

Anna Maria Fulterer

**Competing Phases in High- T_c Superconductors:
Variational Cluster Approach
From Equilibrium to Non-Equilibrium**

DOCTORAL THESIS

For obtaining the academic degree of
Doktorin der technischen Wissenschaften

Doctoral Programme of Technical Sciences
Technical Physics



Graz University of Technology

Supervisor:

Univ. Prof. Dr.rer.nat. Enrico Arrigoni

Institute of Theoretical Physics - Computational Physics

Graz, June 2012

To my family

Ich möchte mich bei meinem Betreuer Prof. Enrico Arrigoni für die gute Zusammenarbeit, seine Unterstützung und den Freiraum bedanken, den er mir bei meiner Arbeit zugestanden hat. Ebenso bei Prof. H. Sormann, durch dessen Hände die Arbeit in der Vorbegutachtungsphase gegangen ist, für die wertvollen Vorschläge zur Verbesserung dieser Arbeit. Danke an Christoph Heil, Michael Knap, Faruk Geles, Martin Nuss, Markus Aichhorn, Peter Pippan und Ralph Gamilschegg und die anderen Kollegen am Institut für theoretische Physik der TU Graz.

Abstract

The pair formation in high temperature superconducting cuprates is believed to happen in the two dimensional CuO_2 layers, that are a common feature of most of these materials. High temperature superconductivity, however, is not a totally two-dimensional phenomenon. In fact, the transition temperature T_c is a dome shaped function of the number of neighbouring CuO_2 layers per unit cell. Interactions between neighbouring layers can happen by tunneling of pairs or single particles. The materials are highly anisotropic so that the conductance within the layers is much larger than perpendicular to the layers.

In this work, we use the one band Hubbard model to describe the CuO_2 layers. To treat the strong onsite correlation on copper d-shells and in order to account for the hopping to neighbouring sites, we solve the Hamiltonian on a cluster of lattice sites and incorporate the inter-cluster hopping perturbatively. The perturbative treatment is then improved by adding a variational condition within the Variational Cluster Approach (VCA). We study the phase diagram of this model, which describes the competition between antiferromagnetism and superconductivity for both electron and hole doping. We obtain spectra for optimally doped and overdoped samples. Our results indicate that the inter-layer coupling is an essential parameter to describe multilayer cuprates.

Another important issue, connected to the inter-layer coupling, is the c-axis current. We adopt a recently developed method to incorporate non-equilibrium Green's functions within the VCA formalism. This allows us to simulate the application of a voltage to a Hubbard monolayer or bilayer, obtained by connecting two electrodes across the Hubbard layer. Here we apply for the first time an expression that is the natural extension of the equilibrium variational condition. Using this non-equilibrium "Euler like" equation, we find that the application of a bias voltage not only leads to a change in particle density and a current flowing through the sample, but also to a decrease of the superconducting order parameter and in the end, for high enough coupling strength to the electrodes, superconductivity vanishes.

non equilibrium, cuprates, high temperature, superconductors, embedding cluster approaches, Green's functions, bilayer

Zusammenfassung

Man nimmt an, dass die Paarbildung in keramischen Hochtemperatursupraleitern vor allem in den zweidimensionalen Kupferdioxyschichten stattfindet, die diesen Materialien gemein sind. Hochtemperatursupraleitung ist aber kein rein zweidimensionales Phänomen. Die Übergangstemperatur, z.B., ist eine Funktion der Anzahl von benachbarten CuO_2 Schichten in der Einheitszelle. Wechselwirkung zwischen benachbarten Schichten geschieht durch Tunneln von einzelnen oder gepaarten Teilchen. Die keramischen Hochtemperatursupraleiter sind aber trotzdem stark anisotrop, sodass die Leitfähigkeit in der Schicht jene senkrecht zu den Schichten, in Richtung der c-Achse, bei weitem übertrifft.

In dieser Arbeit verwenden wir das Einband-Hubbardmodell um die CuO_2 Schichten zu beschreiben. Damit sowohl die starke lokale Coulombwechselwirkung in den d-Orbitalen der Kupferatome als auch das Hüpfen zwischen benachbarten Kupferatomen gut berücksichtigt werden kann, lösen wir den Hubbard Hamilton-Operator auf einem Cluster aus Gitterplätzen, und erfassen the Hüpfen von Teilchen zwischen den Clustern störungstheoretisch. Wir verwenden eine variationelle Variante der soeben beschriebenen Methode, den Variationellen Cluster Ansatz, um das Phasendiagramm dieses Modells zu untersuchen, welches den Wettbewerb zwischen Supraleitung und Antiferromagnetismus beschreibt. Wir analysieren den Einfluss der Hüpfprozesse zwischen den Schichten (inter-layer) auf Spektren und Phasendiagramm von Vielschicht-Hochtemperatursupraleitern.

Ein wichtiges Thema, das mit dem inter-layer Hüpfen im Zusammenhang steht, ist der Strom in Richtung der c-Achse, hervorgerufen durch das Anlegen einer Spannung. Wir verwenden eine kürzlich entwickelte Methode, nämlich den Variationellen Cluster Ansatz mit Greenschen Funktionen im Nichtgleichgewicht. Damit berechnen wir was passiert, wenn an eine dünne Schicht von hochtemperatursupraleitendem Material über metallische Kontakte eine Spannung angelegt wird. Die Ergebnisse zeigen, dass die Biasspannung an der dünnen supraleitenden Schicht nicht nur zu Änderungen in der Dichte, und zu einem Stromfluss durch die Schicht führt, sondern auch zum Schrumpfen des supraleitenden Ordnungsparameters, und bei genügend starker Kopplungsstärke, zum Verschwinden der Supraleitung.

Nicht Gleichgewicht, Cuprate, Hochtemperatur, Supraleiter, Keldysh Formalismus, Bilayer, Schichten

Contents

0.1	Preamble	iv
0.2	Organization	v
1	Introduction	1
1.1	Superconductivity	1
1.2	High- T_c Superconductors	2
1.3	Map onto Hubbard model	5
1.4	Aim of the Work	8
2	Copper Oxide Layer in Equilibrium	9
2.1	Introduction	9
2.2	Model	11
2.2.1	z-Hopping or Inter-Layer Hopping	11
2.3	Method	14
2.3.1	Cluster Perturbation Theory	14
2.3.2	Variational Cluster Approach	15
2.3.3	Self-Energy Functional Theory	17
2.3.4	Parameters and Variational Fields Used in this Work	19
2.4	Results	19
2.4.1	Phase Diagram	19
2.4.2	Correlation-Induced Suppression of Bilayer Splitting	23
2.5	Discussion	29
2.5.1	Physics to Model	29
2.5.2	Solver	30
2.6	Conclusion	31

3	High-T_c (Bi)Layer in Non-Equilibrium	33
3.1	Problem Statement	33
3.2	What has already been done?	33
3.2.1	NSN junction	34
3.2.2	Measurement of C-Axis Transport Behaviour	35
3.2.3	Theoretical Work on the Topic	35
3.2.4	Stacks of Josephson Junctions	36
3.2.5	Phase Transition by Field Effect	36
3.2.6	Relevant Aspects	37
3.3	Map to Model and Organisation	38
3.3.1	Model	38
3.3.2	Procedere for Solution	39
3.3.3	Organisation	40
3.3.4	Expectations	41
3.4	Keldysh Formalism	42
3.5	CPT plus Keldysh	44
3.5.1	Steady State	46
3.5.2	Current	46
3.5.3	Implications of Our Specific Setup	47
3.6	Leads	49
3.6.1	Green's function for $\tau = -\infty$	49
3.6.2	One-Sided Particle-Hole Transformation	50
3.7	Test: TB Central Region	51
3.7.1	Recovering the 3D TB Model	51
3.7.2	Lead DOS and Dispersion Relation	53
3.7.3	Applying Voltage	54
3.7.4	Particle Density	55
3.8	Coupling Strength Γ	56
3.9	Effect of Lead Bandwidth and Interaction U	57
3.9.1	Non-Interacting Central Region	57
3.9.2	Interacting Central Region	57

3.10	Variational Cluster Approach for Non-Equilibrium	61
3.10.1	Variational Cluster Approach + Keldysh	61
3.10.2	Variational Condition	62
3.11	Frequency Integration over Objects in Keldysh Space	65
3.11.1	Equilibrium	65
3.12	NnSN in Non-Equilibrium: Results	68
3.12.1	Monolayer as Central Region	68
3.12.1.1	$\Gamma = 0.01$, Narrow and Wide Lead Bands	69
3.12.1.2	$\Gamma = 0.005$, Wide Lead Bands	75
3.12.2	Bilayer as Central Region	77
3.12.2.1	Adaptions in Model and Method	78
3.12.2.2	Bilayer, $\Gamma = 0.01$, Wide Lead Bands	80
3.12.3	Alternative Monolayer as Central Region	84
3.12.4	Summary of the Results	85
3.13	Discussion and Conclusion	87
3.13.1	Physics to Model	87
3.13.2	Solver	87
3.13.3	Summary	90

A Derivation of the Equilibrium Euler Equation 91

Nomenclature

ε	onsite energy
Γ	coupling strength
λ	variational parameters
μ	chemical potential
Ω	grand canonical potential
Σ	self-energy
T_c	transition temperature
a	lattice spacing
T	temperature
t_L	hopping amplitude in the leads
V	hybridisation
2D	two dimensional
3D	three dimensional
CPT	Cluster Perturbation Theory
DOS	density of states
e	electron charge
HTSC	high- T_c superconducting cuprates
NnSN	normal state - nano superconductor - normal state
NSN	normal conductor - superconductor - normal conductor
SFT	Self-Energy Functional Theory
SIS	superconducting - insulator - superconductor
TB	tight-binding
VCA	Variational Cluster Approach

0.1 Preamble

Since their discovery in 1986 high transition temperature superconductors have attracted much interest and triggered a lot of both experimental and theoretical work aiming at a better understanding of their mechanism and their other properties.

One of the mainstream ideas is, that pairing is mediated by spin fluctuations. The main difficulty in the numerical description of high- T_c materials lies in the strong local correlations experienced by charge carriers. This means, that the particles in these materials do not experience a mean field, but are interacting strongly with each other. In a numerical simulation, this complex system of strongly correlated particles can only be treated approximately. The first simplification we make is to use the Hubbard model. This is already a heavy approximation, since only the copper dioxide layers are taken along and the processes now happen on lattice, and not in continuous space. The Hubbard model, however, still needs to be solved. This leads to major problems, since both the correlations and the hopping between sites are relatively large, and none of them can be treated perturbatively.

We want to make use of the Variational Cluster Approach to solve the Hubbard model. It combines the exact evaluation of a cluster's Green's function and its perturbation by inter-cluster hopping terms with a variational calculation. This leads to a good description of both short-range correlations and long-range symmetry broken phases. In this way, we want to calculate the properties of bilayer and monolayer superconducting cuprates.

The last years have seen a rising of the Keldysh formalism to treat systems out of equilibrium. This method was developed in 1965 [1], and, due to the growing power of modern computers, it can now be used to simulate complex systems in non-equilibrium setups.

We simulate a metal - (single layer) superconductor - metal junction with a constant applied voltage, that has evolved into a steady state. We will use the Variational Cluster Approach in Keldysh space to describe such a junction, and present its properties as a function of initial doping in the superconductor, applied voltage and bandwidth of the metal. We also discuss the simplifications and limitations that we have made, and the inaccuracies they introduce.

0.2 Organization

The work is organized as follows: In Chapter 1 we introduce the reader to superconductivity, justify the use of the Hubbard model, give notice of the methods that we use and finally lay out in detail the problems that we want to tackle.

Chapter 2 treats the first part of the work, the simulation of monolayer and bilayer cuprates in equilibrium. The model to be solved is laid out in Section 2.2. Section 2.3 gives an in-depth description of the methods used. The results are presented in Section 2.4 and discussed in Section 2.5. A great part of the results to this problem has been published in the Journal of Superconductivity and Novel Magnetism [2]. We have incorporated this publication and marked verbatim text by using the following font: "Competing Phases in High- T_c Superconductors".

In Chapter 3 we focus on the non-equilibrium problem. Further introductory information on the non-equilibrium setup is given in Sections 3.1 to 3.3. Sections 3.4 to 3.9 show the CPT + Keldysh formalism employed for the description of the non-equilibrium problem, and some applications to understand the peculiarities of our three dimensional setup. Finally, we come to the Variational Cluster Approach + Keldysh method in Section 3.10. We present the results of our simulation of a normal metal - thin superconductor - normal metal junction in Section 3.12 and thereafter discuss the model and method in Section 3.13.

Chapter 1

Introduction

We first address superconductivity generally in Section 1.1, and high transition temperature superconductivity in Section 1.2. We motivate the use of the Hubbard model in Section 1.3, and finally point out the problems that we want to solve in Section 1.4.

1.1 Superconductivity

Superconductivity was discovered at the beginning of the twentieth century. The phenomenon of electronic current had been known from the beginning of the 17th century. It was the English physicist William Gilbert, who made first investigations about electricity. From the beginning of the 19th century electricity was used for light generation.

Metals consist of atoms of elements that have only few electrons in the outer shells. If the valence band, the highest occupied band at zero temperature, is only half-filled, the electrons can be excited with an infinitesimal amount of energy (gapless) out of the Fermi sea and move freely through the material. If a voltage is applied, the mean motion of the electrons is towards the positive pole. The resistance comes from electrons being scattered at other electrons, impurities and lattice vibrations.

Conventional Superconductors

At the beginning of the 20th century Heike Kamerlingh Onnes succeeded in cooling helium (He) into its liquid phase (4.2K). He then used the liquid He to cool metals down to low tem-

peratures. He expected the resistivity to shrink, since he thought that resistivity is caused by the electrons being scattered from the lattice. We now know, that electrons are scattered from lattice vibrations. In fact, what Kamerlingh Onnes found was that the resistivity (of mercury) decreased when the material was cooled down to low temperatures. But, all of a sudden, below the critical temperature T_c it was even zero. He called this state the superconducting state. Forty years later the explanation for superconductivity in metals, the so-called BCS theory, was found [3]. A simple view of this is the following: An electron in an ion lattice deforms the lattice. This lattice deformation attracts another electron. In this way, two electrons are coupled or attracted by the lattice deformation. The lattice deformation modes are termed phonons. Now, each electron, since it is a fermion, occupies its own state. But if two electrons couple, they form a boson, the so called “Cooper pair”. These bosons can all occupy the same, lowest lying state. This coherent state allows a current flow without resistance.

Summing up, we find that at low temperatures, below the transition temperature T_c , the decreased lattice motion not only does not hinder electron motion any more, it even allows the charge carriers to pair up to bosons, which can form a Bose-Einstein condensate.

There exist two types of conventional superconductors, depending on their reaction to an external magnetic field: Type I superconductors are perfect diamagnets, so that the external magnetic field smaller than the critical magnetic field is totally expelled from the material. In type II superconductors there exists a range of critical field intensity, where the magnetic field penetrates into the material, it is however localized by the formation of magnetic flux tubes. Another important characteristic of conventional superconductors is the isotope effect [4]. Substitution of atoms in the compounds by their isotopes changes the coupling strength between the electrons. This proved that phonons, which are influenced by the atomic masses involved, are the coupling particles.

1.2 High- T_c Superconductors

High temperature superconductors are characterized by a higher transition temperature. They show a reduced isotope effect, which suggests that they do not work by the principle “electron pairing by phonons”. A family of high- T_c superconductors are those containing CuO_2 layers, called “cuprates”. From now, when speaking about high- T_c superconductors or HTSC, we mean

cuprate high- T_c superconductors, even though there exist other classes of materials showing this effect, like the iron pnictides [5], based on FeAs layers.

Structure of the Undoped (Parent) Compounds

Cuprate superconductors have a perovskite structure. They consist of copper dioxide CuO_2 layers which sandwich other atoms. The CuO_2 layers are believed to carry the charge, while the atoms in between act as charge reservoirs. There may be one or more CuO_2 layers in the unit cell. Let us first just regard a single-layer material. Oxygen consists of 8 electrons (and each 8 protons and neutrons). The lowest two electrons fill the 1s shell, next 2 electrons for the 2s shell. The remaining 4 electrons sit in the 2p, which would be filled by another 2 electrons. Copper has got the ordering number 29 and thus 29 electrons. The electron configuration is $1s^2 2s^2 2p^6 3s^2 3p^6 3d^{10} 4s^1$. In the CuO_2 layer two electrons from copper move to oxygen which has now a filled 2p shell. One could also say that the electrons form a hybridisation band which has got its emphasis on the oxygen. Now the configuration of oxygen is $1s^2 2s^2 2p^6$ or $[\text{Ne}]$, and that of Copper is $1s^2 2s^2 2p^6 3s^2 3p^6 3d^9$ or $[\text{Ar}]3d^9$. So the oxygen is inert while on the Copper there is an unpaired electron and an unpaired spin. Because of the specific lattice structure, the 3d orbitals are not degenerate. The hole sits in the highest orbital of $d_{x^2-y^2}$ symmetry. In this orbital the Coulomb repulsion is very strong, which means that double occupancy costs a large amount of correlation energy U . The large correlation makes the material an insulator, even if it should be a metal considering the half filled valence band and according to simple LDA calculations [6]. Depending on the value of U and the temperature the material can then be a charge transfer insulator (see Section 1.3) or an antiferromagnetic insulator.

Phase Diagram

The phase diagram of HTSC as a function of doping and temperature is schematically reproduced in Fig. 1.1. At half filling the materials are insulators, for electron and hole doping the long range antiferromagnetism vanishes and instead the superconducting state forms, and vanishes again at higher dopings. The details vary from one specific material to the other, but the general picture is the same.

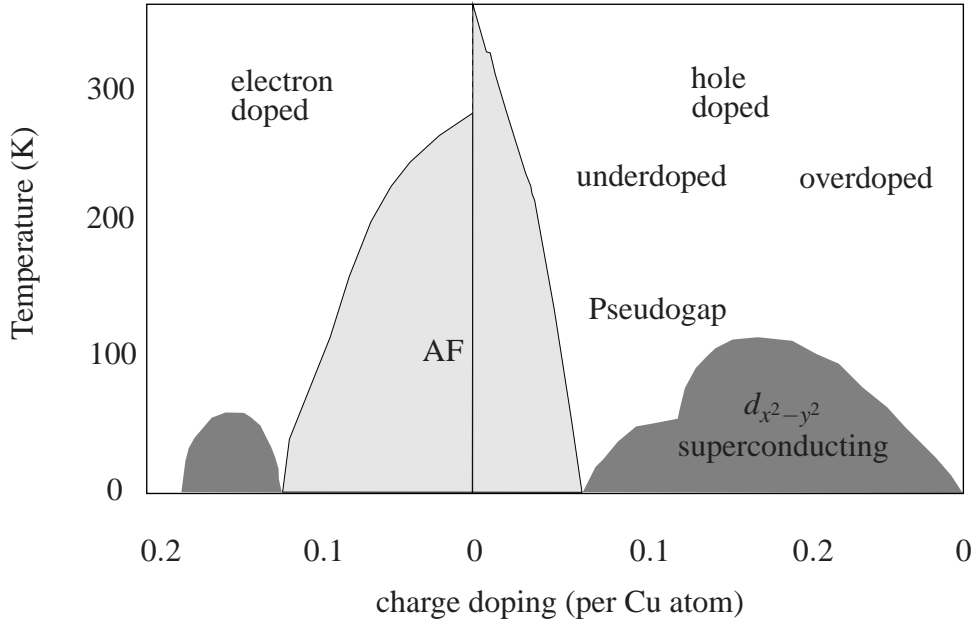


Figure 1.1: Schematic phase diagram in temperature and doping of copper oxide materials [7]. Such a phase diagram is obtained experimentally for high- T_c materials.

Anisotropy and Other Characteristics

An important feature of high- T_c superconductors is their anisotropy. Electron dynamics seem to happen mainly in the CuO_2 layers, but there is interaction between the layers in one unit cell and between different unit cells. This interaction leads to transport phenomena in c -axis direction, which is perpendicular to the CuO_2 layers. The mechanisms that contribute to c -axis current are still under discussion, just like the enigmatic pseudogap (e.g. [8]) or an inter-layer contribution to the superconducting order parameter.

Possible Pairing Mechanism

While it is known that charge carriers in normal superconductors pair by bosonic interaction (phonons), the mechanism in high- T_c superconductors is still under discussion. Many theories have been proposed, most of which succeed to explain or predict only some aspects. One idea is that superconducting pairs are formed because of phonon interaction, just like in normal superconductors [9]. On the other hand, there is overwhelming evidence for the coupling mediated by spin fluctuations [10, 11] (also called magnons or, more generally, spin-polarons[12]). Other theories proposed include a bosonless coupling and the bisoliton theory [13, 14].

A schematical explanation of the spin fluctuation mediated coupling in real space could be

the following: The spins on the copper are subject to a large correlation energy and order antiferromagnetically by superexchange. An additional hole disturbs this order and creates a spin-polaron (spin-polarisation of its surrounding). This spin-polaron can enable the coupling to other holes.

1.3 Map onto Hubbard model

In Section 1.2 we mentioned, that particles on the copper 3d orbital are subject to strong on-site Coulomb interaction. The Cu $3d_{x^2-y^2}$ -orbital is thus only half-filled, which leads to an unpaired spin on each copper site. Between two copper atoms there sits an oxygen atom, the p-orbitals filled by two electrons with antiparallel spins. This results in a superexchange interaction between the two copper atoms, with the unpaired spins ordering antiferromagnetically [15]. When considering the copper and the oxygen bands around the Fermi energy, one finds that the undoped parent compound is a charge-transfer insulator [16, 17].

Away from half-filling there is an asymmetry between electron and hole doping, which is also observed in experiments. Doped holes localize on the oxygen atoms, and destroy the antiferromagnetic coupling between Cu spins. On the other hand, doped electrons live on the Cu sites, where they dilute the antiferromagnetically ordered spins [18]. This explains, why the antiferromagnetic phase is much more stable for electron than for hole doping, as illustrated in Fig. 1.1.

Already in 1987 it was suggested, that CuO_2 layers in HTSC can be described by the Hubbard model [19]. A generalized single-band Hubbard Hamiltonian reads:

$$H_{\text{H}} = - \sum_{\sigma, ij} t_{ij} (c_{i\sigma}^\dagger c_{j\sigma} + c_{j\sigma}^\dagger c_{i\sigma}) + \sum_i U_i n_{i\uparrow} n_{i\downarrow}, \quad (1.1)$$

where $c_i(c_i^\dagger)$ is the annihilation(creation) operator on site i , t_{ij} is the hopping amplitude between sites i and j and $n_{i\sigma}$ denotes the particle number operator which counts the particles of spin $\sigma \in \uparrow, \downarrow$ on site i . The main ingredients for the Hubbard Hamiltonian are the strong correlations U_i and the hoppings between sites, weighted by parameter t . For the description of CuO_2 layers, the Hamiltonian is defined on a square lattice.

The above arguments could make us assume, that the physics of CuO_2 planes should be described by a 3-band Hubbard model, with one Cu band and two oxygen bands. The number of

orbitals per site that should be used is however still issue of discussion. Usually, a single-band Hubbard Hamiltonian is used instead of the three-band one. The single-band Hubbard model, however, describes a Mott-insulator at half-filling. Why should it still be useful for describing CuO₂ planes? The answer to this question is the Zhang-Rice singlet: A doped hole occupies a quasi-localized state on the four neighbouring oxygen atoms of a Cu-site. Such a hole then forms a local spin-singlet with the hole on the central Cu-site, referred to as Zhang-Rice singlet [20]. The Zhang-Rice singlets are the charge carriers, and are the candidates to condense into the superconducting state. When using the single-band Hubbard model, the doped holes should describe these Zhang-Rice singlets.

It fact, numerical simulations of the single-band Hubbard model yield physical observables like the Fermi surfaces, spectral functions and others in qualitative agreement with experimental results [21, 22, 23]. It is however essential to include next-nearest neighbour hopping terms, which generate the difference between particle and hole doping that has been described above.

We decided to use the single-band Hubbard model, since it is much more simple and easier in the numerical treatment, and still describes the essential features of high-T_c cuprates. The total single-band Hubbard Hamiltonian for a CuO₂ monolayer reads

$$H_H = -t \sum_{\langle ij \rangle} \sum_{\sigma} (c_{i\sigma}^{\dagger} c_{j\sigma} + c_{j\sigma}^{\dagger} c_{i\sigma}) + t' \sum_{\langle\langle ij \rangle\rangle} \sum_{\sigma} (c_{i\sigma}^{\dagger} c_{j\sigma} + c_{j\sigma}^{\dagger} c_{i\sigma}) + U \sum_i n_{i\uparrow} n_{i\downarrow} - \mu \sum_{i\sigma} n_{i\sigma}, \quad (1.2)$$

with hopping t between nearest neighbour Cu sites, and next-nearest neighbour hopping t' . The chemical potential μ fixes the doping of holes (or Zhang-Rice singlets), for $\mu = U/2$ the system is half filled. Most importantly, the strong onsite-interaction of particles on the Cu sites is accounted for by the correlation energy U . When treating the bilayer, we additionally need to know the inter-layer hopping terms.

Even the single-band Hubbard model on a square lattice has not been solved exactly. The main difficulty in the numerical treatment of the Hubbard model in our case is that t and U are of the same order of magnitude and thus it does not justify to treat one of them perturbatively. A means to solve the Hubbard model numerically is the so-called Cluster Perturbation Theory (CPT) [24, 25], see Section 2.3.1. We use an extension of the CPT, called Variational Cluster Approach (VCA), to describe the competition between antiferromagnetism and superconductivity. An introduction to VCA is given in Section 2.3.2.

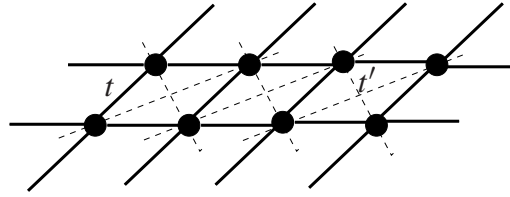


Figure 1.2: Intra-layer hopping processes. The filled circles denote the Cu sites, where strong Coulomb interaction U takes place. Particles hop along the solid lines (nearest neighbour hopping) and dashed lines (next-nearest neighbour hopping).

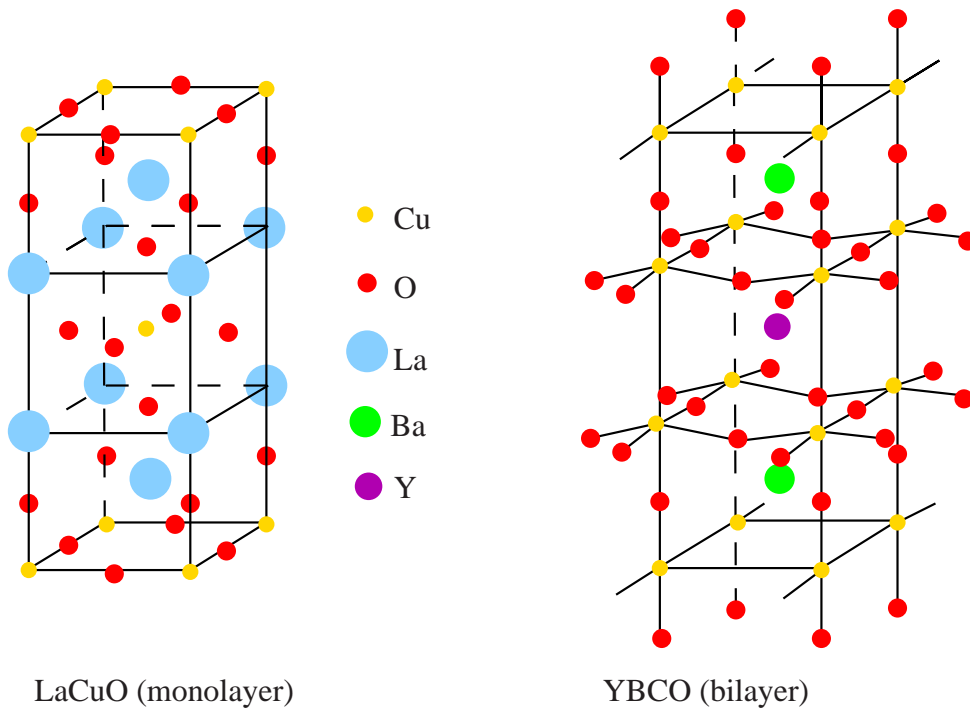


Figure 1.3: Crystal structure of the LaCuO (left) and YBCO (right) parent compounds. They represent two types of the high- T_c superconductors, namely monolayer and bilayer materials.

1.4 Aim of the Work

We want to study the properties of cuprate high- T_c superconductors. The model that we use to describe these materials, is the single-band Hubbard model. As solver we have chosen the Variational Cluster Approximation. Our focus will be on the difference between monolayer and bilayer materials, see Fig. 1.3. These are materials containing one or two CuO_2 layers per unit cell, respectively.

In the first part of the work, we study the equilibrium situation. It is described by the Hubbard model defined on a two dimensional (2D) lattice. For the bilayer system, we add an inter-layer hopping to describe two coupled 2D layers. We calculate the phase diagram and compare spectra of the monolayer and bilayer system to experimental results. The focus is on the splitting caused by the inter-layer hopping, which is expected to be renormalized by strong correlations.

In the second part of the work, we present a new version of VCA to treat systems out of equilibrium. It can be used to investigate a strongly correlated central region in a symmetry broken phase like superconductivity at time $\tau = -\infty$, which is at time τ_0 contacted by two leads at different chemical potentials. In this way, a bias voltage is applied to the central region. After some time, a steady state evolves, and with the new version of VCA, one can analyse this state, e.g. find out if it is still symmetry-broken and measure the c-axis current. The setup that we use for testing the new method, is a metal - (nano) superconductor - metal (NnSN) junction with applied voltage, see Fig. 3.1. This is an interesting application of the non-equilibrium VCA, and there exists a considerable amount of both experimental and theoretical work about similar setups, but with wider superconducting central region. Especially experiments done to analyse the anisotropy in high- T_c superconductors, like measuring the c-axis versus ab-axis charge dynamics could be comparable to our setup.

Chapter 2

Copper Oxide Layer in Equilibrium

A large part of the results presented in this chapter has been published in Ref. [2]. The author's contribution to the work was to use and modify where necessary an existing VCA code, mainly written by the coauthor, in order to explore the bilayer Hubbard model. Moreover, the author interpreted the results scientifically, made a literature recherche to investigate the status quo of scientific research in this field and compared to experimental and theoretical results. Since the article is part of this PhD work, it is included in the present thesis with the agreement of all authors. However, since it is published work, parts taken verbatim from this article are marked explicitly by using a special font "Copper Oxide Layer in Equilibrium".

We carry out a theoretical study of the bilayer single-band Hubbard model in the undoped and in the superconducting phases by means of the Variational Cluster Approach. In particular, we focus on the effects of bilayer splitting induced by the inter-layer hopping, as well as its interplay with strong correlation effects. We find that the bilayer splitting between the antibonding and bonding is considerably suppressed in both the normal and superconducting phases, in qualitative agreement with experiments on $\text{Bi}_2\text{Sr}_2\text{CaCu}_2\text{O}_{8+\delta}$. In addition, in the superconducting phase, the shape of the splitting in k space is modified by correlations.

2.1 Introduction

It is widely accepted that the fundamental physics of High-Tc superconductors (HTSC) takes place in the two-dimensional CuO_2 -layers. On the other hand, several classes of HTSC exist with a different number of CuO_2 -layers per unit cell, their transition temperature being strongly

related to this number [26]. There have been several explanations for this phenomenon, among them one could mention inter-layer interactions, charge imbalance or quantum tunneling of Cooper pairs [27, 28, 29].

Experimental measurements, supported by theoretical investigations [30], show that the inter-layer coupling and the third dimension more generally have a strong impact on angle-resolved photoemission spectroscopy (ARPES) results [31, 32, 33]. Depending on photon energy and polarisation, different features are accentuated in the measured spectra [34, 35], while the “real” underlying quasiparticle spectrum remains hidden.

In the last decade, the BiSrCuO compounds BSCO-2212 and BSCO-2201 have been studied thoroughly, and several conclusions have been drawn from the results: High resolution ARPES on BSCO-2212 with suppressed superstructure reveals the presence of two Fermi surface pieces, one hole-like, the other changing from electron to hole-like [35]. Heavily overdoped BSCO-2212 shows a difference in bilayer band splitting for the normal and superconducting case [36]. In the normal state this is about 88meV and gets renormalized to about 20meV in the superconducting state. In the superconducting state each one of the two split bands develops its own peak-dip-hump structure (PDH). This is most probably due to the strong renormalisation at about 60 meV produced by the interactions with spin fluctuations [36].

Bilayer splitting in the normal state only weakly depends on doping [37]. In optimally doped BSCO-2212 (bilayer) the quasiparticle in the $(\pi,0)$ region should look similar to that of BSCO-2201 (monolayer) [34], the enhanced linewidth in the bilayer material is attributed to correlation effects, more specifically (π,π) scattering due to antiferromagnetic fluctuations. In order to unravel the underlying mechanisms producing these effects, different theoretical methods have been applied. LDA calculation done for YBCO [38] show that the inter-layer hopping comes from copper s electrons. Different models were used to describe the system of coupled 2D CuO planes, e.g. the bilayer Hubbard Model [39, 40], coupled two-leg spin ladders [41], tight-binding extended Hubbard Model [42, 43], bilayer t-J model [44]. From these calculations the following conclusions can be drawn. The PDH structure can be explained by a coupling of the electronic excitations to magnetic resonances or spin fluctuations [45, 46]. At low doping, the coupling between the layers should be antiferromagnetic [40], and there might be contributions to superconductivity by inter-layer Cooper pairs, being formed by holes belonging to different layers. The reduction of the bilayer splitting with respect to the noninteracting

tight-binding model is attributed to the formation of spin bags in the layers [44], which increases the quasiparticle weight or/and antiferromagnetic inter-layer order.

We want to address these issues by an alternative approach, in which correlations are evaluated exactly at a short-range level of a cluster, and thus is expected to capture the interplay between short-range antiferromagnetic coupling and quasiparticle excitations. Specifically, we use the Variational Cluster Approach (VCA) [47, 48] treated in Section 2.3.2 to solve the bilayer Hubbard model. VCA is an extension of Cluster Perturbation Theory (CPT) [24, 25], Section 2.3.1). Due to its variational nature it allows for a treatment of symmetry breaking phases, in our case antiferromagnetism and/or superconductivity. The method has already been successfully applied to a wide range of problems [48, 22, 49, 50, 51] and is based on the Self-Energy Functional Theory (SFT) [52, 53], described in Section 2.3.3. We will illustrate the effects of bilayer splitting by displaying the spectral functions for the two bands. Finally, we will discuss the reduction of bilayer splitting due to correlation in both the normal as well as in the superconducting state.

2.2 Model

A single CuO_2 layer is described by the standard two-dimensional Hubbard Hamiltonian (see Section 1.3)

$$H_H = -t \sum_{\langle ij \rangle} \sum_{\sigma} (c_{i\sigma}^{\dagger} c_{j\sigma} + c_{j\sigma}^{\dagger} c_{i\sigma}) + t' \sum_{\langle\langle ij \rangle\rangle} \sum_{\sigma} (c_{i\sigma}^{\dagger} c_{j\sigma} + c_{j\sigma}^{\dagger} c_{i\sigma}) + U \sum_i n_{i\uparrow} n_{i\downarrow} - \mu \sum_{i\sigma} n_{i\sigma} \quad (2.1)$$

in standard notation. As usual, we include a next-nearest hopping in order to reproduce the band structure observed in ARPES experiments.

2.2.1 z-Hopping or Inter-Layer Hopping

For the description of bilayer materials the inter-layer part of the Hamiltonian is essential. As well known, for example from LDA calculations, the inter-layer hopping has a characteristic k_{\parallel} structure, where k_{\parallel} is the wave vector in the CuO_2 plane, the (x, y) -plane.

We use the k_{\parallel} -dependent inter-layer hopping derived in Ref. [38] for $\text{YBa}_2\text{Cu}_3\text{O}_7$ (YBCO), which is a bilayer HTSC compound. They obtained the inter-layer hopping in the following

way: The band structure of the material was described in the local density approximation. Then, the high-energy and chain related degrees of freedom were integrated out, to arrive to two 8-band Hamiltonians, for the even and odd bands of the bilayer respectively. Downfolding these 8-band Hamiltonians leads to a single-layer Hubbard Hamiltonian, with an k_{\parallel} -dependent inter-layer hopping (which comes mainly from copper s and oxygen d-orbitals) of the form

$$t_{\perp}(k_{\parallel}) = \tilde{t} \frac{v^2}{(1 - 2u' \frac{t'}{t})^2} \quad (2.2)$$

with

$$u = \frac{\cos(k_y B) + \cos(k_x A)}{2} \quad (2.3)$$

$$v = \frac{\cos(k_y B) - \cos(k_x A)}{2} \quad (2.4)$$

and A, B the lattice constants. Since $ut'/t \ll 1$, we can Taylor expand the denominator in eq. (2.2) in terms of $s = 2ut'/t$ to obtain

$$\frac{1}{(1-s)^2} \approx 1 + 2s, \quad (2.5)$$

We approximate the denominator by 1 and are left with

$$\Rightarrow t_{\perp}(k_{\parallel}) \approx \tilde{t} v^2 = \frac{\tilde{t}}{4} (\cos k_y B - \cos k_x A)^2 \quad (2.6)$$

In VCA we need the hopping term in real space, and thus have to Fourier transform the hopping term into space coordinates.

The whole inter-layer hopping term in the Hamiltonian is

$$H_{t_{\perp}} = \sum_{k_x, k_y} t_{\perp}(k_{\parallel}) (c_{ak_{\parallel}}^{\dagger} c_{bk_{\parallel}} + c_{bk_{\parallel}}^{\dagger} c_{ak_{\parallel}}), \quad (2.7)$$

with $c_{ak}^{\dagger} (c_{bk})$ the creation(annihilation) operator of a particle with wave vector k_{\parallel} in the layer $a(b)$. Fourier transform of the creators and annihilators from \vec{k}_{\parallel} into real space sites R, R' in the layer leads us to

$$\begin{aligned} H_{t_{\perp}} &= \sum_{k_x, k_y} t_{\perp}(k_{\parallel}) \left(\underbrace{\frac{1}{\sqrt{N_{2D}}} \sum_R e^{ik_{\parallel} R} c_{aR}^{\dagger}}_{c_{ak_{\parallel}}^{\dagger}} \underbrace{\frac{1}{\sqrt{N_{2D}}} \sum_{R'} e^{-ik_{\parallel} R'} c_{bR'}}_{c_{k_{\parallel} b}} + h.c. \right) = \\ &= \sum_{k_x, k_y} t_{\perp}(k_{\parallel}) \frac{1}{(\sqrt{N_{2D}})^2} \sum_{R, R'} e^{ik_{\parallel} (R-R')} (c_{Ra}^{\dagger} c_{R'b} + h.c.) = \\ &= \sum_{R, R'} \underbrace{\frac{1}{(\sqrt{N_{2D}})^2} \sum_{k_x, k_y} t_{\perp}(k_{\parallel}) e^{ik_{\parallel} (R-R')} (c_{Ra}^{\dagger} c_{R'b} + h.c.)}_{=T(R-R')} \end{aligned} \quad (2.8)$$

The hopping amplitude in spatial coordinates becomes:

$$\begin{aligned}
T(R - R') &= \frac{1}{(\sqrt{N_{2D}})^2} \sum_{k_x, k_y} t_{\perp}(k_{\parallel}) e^{ik_{\parallel}(R - R')} = \\
&= \frac{1}{\sqrt{N_{2D}}} \sum_{k_x} \frac{1}{\sqrt{N_{2D}}} \sum_{k_y} t_{\perp}(k_{\parallel}) e^{ik_{\parallel}(R - R')} \\
&\rightarrow \frac{1}{2\pi} \int dk_x \frac{1}{2\pi} \int dk_y t_{\perp}(k_{\parallel}) e^{ik_{\parallel}(R - R')},
\end{aligned} \tag{2.9}$$

where we took the lattice constant to be 1.

Introducing the distance between lattice positions in the (x, y) -plane $(\Delta x, \Delta y)$ for $R - R'$ we get:

$$T(\Delta x, \Delta y) = \frac{1}{(2\pi)^2} \int dk_x \int dk_y t_{\perp}(k_{\parallel}) e^{ik_x \Delta x} e^{ik_y \Delta y}. \tag{2.10}$$

And if we replace $t_{\perp}(k_{\parallel})$ by the r.h.s. in eq. (2.6) we obtain

$$T(\Delta x, \Delta y) = \frac{1}{(2\pi)^2} \int dk_x \int dk_y \frac{\tilde{t}}{4} (\cos k_y B - \cos k_x A)^2 e^{ik_x \Delta x} e^{ik_y \Delta y}. \tag{2.11}$$

Integrating this out (using $A = B = 1$) gives:

$$\frac{\tilde{t}}{(2\pi)^2} \frac{2 \sin(\pi \Delta x)}{\Delta x} \frac{2 \sin(\pi \Delta y)}{\Delta y} \left[\frac{(\Delta y)^2 - 2}{(\Delta y)^2 - 4} + \frac{(\Delta x)^2 - 2}{(\Delta x)^2 - 4} - \frac{2(\Delta x)^2 (\Delta y)^2}{((\Delta x)^2 - 1)(\Delta y)^2 - 1} \right] \tag{2.12}$$

or, using the Kronecker δ ,

$$T(\Delta x, \Delta y) = \frac{\tilde{t}}{(2\pi)^2} \left[-\pi^2 \delta_{\Delta x, 0} \delta_{\Delta y, 0} + \frac{\pi^2}{2} \delta_{\Delta x, \pm 1} \delta_{\Delta y, \pm 1} - \frac{\pi^2}{4} (\delta_{\Delta x, \pm 2} \delta_{\Delta y, 0} + \delta_{\Delta x, 0} \delta_{\Delta y, \pm 2}) \right]. \tag{2.13}$$

This means, that in real space there are three types of inter-layer hopping terms, a vertical hopping ($\delta_{\Delta x, 0} \delta_{\Delta y, 0}$), a diagonal hopping ($\delta_{\Delta x, \pm 1} \delta_{\Delta y, \pm 1}$), and one along the x or y axis ($\delta_{\Delta x, 0} \delta_{\Delta y, \pm 2}$ and $\delta_{\Delta y, 0} \delta_{\Delta x, \pm 2}$). This is illustrated in Fig. 2.1.

Expressing the amplitude of the direct inter-layer hopping $t_{\perp}(0, 0)$ in terms of the amplitude in k -space \tilde{t} , which we have first used in equation (2.2) gives:

$$t_{\perp}(0, 0) = \frac{\tilde{t}}{(2\pi)^2} (-\pi^2) = -\frac{\tilde{t}}{4} \tag{2.14}$$

Values for the ratio of \tilde{t} and nearest neighbour hopping t appearing in the literature include $\tilde{t}/t = 0.25/0.4 = 0.625$ for YBCO (according to [38]) and $\tilde{t}/t \approx 0.3$ for BSCO bilayers [43].

We will use $\tilde{t} = 0.2$.

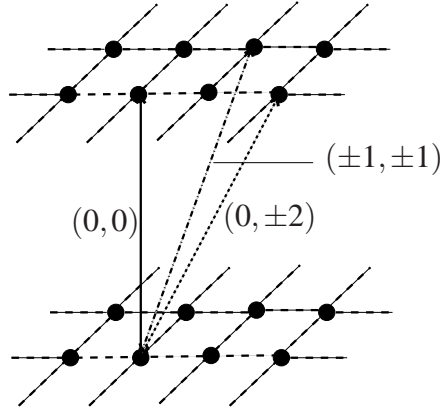


Figure 2.1: Inter-layer hopping processes. We sketch the three types of inter-layer hoppings. The solid line labeled $(0,0)$ corresponds to the direct term, $\delta_{\Delta x,0}\delta_{\Delta y,0}$. The dash-dot line labeled $(\pm 1, \pm 1)$ corresponds to the diagonal terms, $\delta_{\Delta x,\pm 1}\delta_{\Delta y,\pm 1}$. The dotted line labeled $(0, \pm 2)$ corresponds to the terms along the x or y axis, $\delta_{\Delta x,0}\delta_{\Delta y,\pm 2}$. For reasons of clarity, we only plot the direct intra-layer hopping (dashed lines).

2.3 Method

The method used for approximating the ground-state properties of the system is VCA, which is a variational extension of CPT. The variational principle based on the self-energy functional approach has been formulated by M. Potthoff [54]. By introducing additional variational fields and “optimizing” the grand potential with respect to these fields, one can study broken-symmetry phases, such as magnetism or superconductivity [48, 22, 49]. In the next three Section, CPT, VCA and SFT are introduced.

2.3.1 Cluster Perturbation Theory

With the help of CPT [24, 25], the single-particle Green’s function of strongly correlated electron systems can be calculated.

(a) The first step is to tile the lattice with identical clusters, where the cluster Hamiltonian H_{CL} can be solved exactly, see Fig. 2.2.

$$H = H_{\text{CL}} + H_{\text{inter-CL}} \quad (2.15)$$

The single-particle Green’s function of a cluster, G^{CL} , is calculated numerically, we do it by Lanczos exact diagonalisation [55].

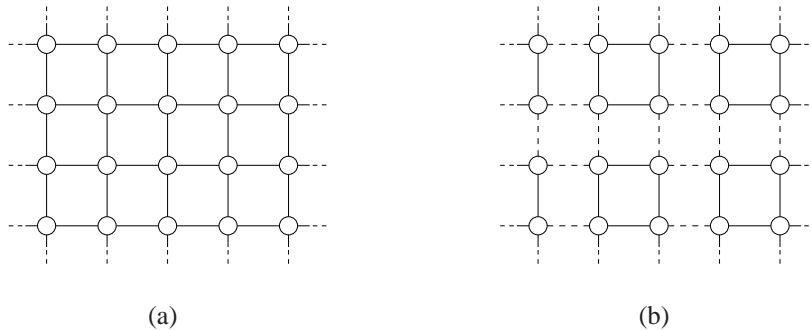


Figure 2.2: CPT: Whole lattice (a) and tiled lattice (b). The circles denote sites with strong correlation, the solid lines denote hoppings between the sites to be treated exactly, along the dashed lines the hopping is treated perturbatively. In this figure, the lattice is tiled with 2×2 clusters.

(b) By coupling the clusters within strong-coupling perturbation theory at leading order, an approximation to the Green's function on the whole lattice G^{CPT} is recovered,

$$G^{\text{CPT}}(z) = \frac{1}{G^{\text{CL}}(z)^{-1} - \hat{T}}, \quad (2.16)$$

where \hat{T} is a matrix describing intercluster hoppings (see e.g. Ref. [51] for details).

The CPT approximation consists in replacing the self-energy of the lattice system by the one describing the cluster only. CPT gives very good results for spectral functions, but it does not allow for spontaneous symmetry breaking.

In order to study symmetry breaking phases like magnetism or superconductivity, a variational principle has been introduced in CPT [48, 47, 51], which leads us to the Variational Cluster Approach.

2.3.2 Variational Cluster Approach

Doing a variational computation means to introduce parameters which are varied to obtain a better solution. In variational CPT, these variational parameters multiply additional single-particle operators A_i that are added to the cluster Hamiltonian, but are subtracted in the perturbation calculation. In order to find the optimum value of these parameters, which we call $\vec{\lambda}$, one looks for a saddle point of the grand canonical potential Ω ,

$$\Omega - \Omega_{\text{CL}}(\vec{\lambda}) = \text{Tr} \sum_{n=1}^{\infty} (G^{\text{CL}}(\vec{\lambda})T)^n \frac{1}{n} = \text{Tr} \ln G^{\text{CPT}} - \text{Tr} \ln G^{\text{CL}}(\vec{\lambda}), \quad (2.17)$$

with T the temperature, $G^{\text{CL}}(\vec{\lambda})$ the cluster Green's function obtained for $H_{\text{CL}}(\vec{\lambda})$, and G^{CPT} the approximatively recovered Green's function of the thermodynamic limit (eq. (2.16)). The cluster grand potential $\Omega_{\text{CL}}(\vec{\lambda})$ at zero temperature is given by $\Omega_{\text{CL}}(\vec{\lambda}) = E_{\text{G}}(\vec{\lambda}) - \mu N$, with the $E_{\text{G}}(\vec{\lambda})$ the ground state energy and N the total number of particles.

The self-energy functional theory (SFT, see Section 2.3.3) introduces a self-energy functional $\hat{\Omega}(\Sigma)$, which is stationary at the exact self-energy Σ of the system. When restricting to the space of self-energies resulting from the reference-cluster, this self-energy functional can be evaluated by eq. (2.17).

In summary, we have the following procedure:

- exact diagonalisation of the cluster Hamiltonian $H'_{\text{CL}}(\vec{\lambda}) = H_{\text{CL}} + H_{\vec{\lambda}}$ with added Weiss fields $H_{\vec{\lambda}} = \sum_i \lambda_i A_i$, where A_i are additional single-particle operators.
- introduction of intercluster terms by first order perturbation calculation, and subtraction of Weiss fields: $G^{-1}(\vec{\lambda}) = G_{\text{CL}}(\vec{\lambda})^{-1} - \hat{T}'(\vec{\lambda})$. Here $\hat{T}'(\vec{\lambda})$ contains the intercluster hopping of the initial Hubbard Hamiltonian and the Weiss fields, the latter with reversed spin.
- variational calculation: The condition is to find the stationary point of $\Omega(\vec{\lambda})$:

$$\frac{\partial \Omega}{\partial \lambda_i} = 0 \quad (2.18)$$

Improvements with respect to CPT:

- It allows for symmetry broken states.
- Variational hopping parameters can correct for the isolation of the cluster from the rest of the lattice in the exact diagonalisation.
- The use of a variational chemical potential μ_{var} helps to simulate a smoothly evolving particle density when doping the system by changing the chemical potential μ .

However, we have to keep in mind that the continuous particle density with doping is just simulated, since the exact diagonalisation of the cluster is still done for a discrete number of particles in the cluster. This leads to an overestimation of the optimal doping and of the superconducting gap, which can be overcome by the introduction of bathsites [56, 57].

2.3.3 Self-Energy Functional Theory

The formalism of SFT is described in Ref. [54, 53, 52]. Here, the VCA self-consistency condition is derived in the SFT framework, mostly referring to Ref. [54]. One starts with a system defined by a Hamiltonian, which contains interaction U and one-particle parameters t ,

$$H = H_0(t) + H_1(U), \quad (2.19)$$

and wants to find its grand potential $\Omega_{t,U}$ and single-particle Green's function $G_{t,U}$.

To do this, using VCA one has to solve the variational condition, eq. (2.18). If the grand potential is expressed as functional of the self-energy, a more general form of this condition can be written as

$$\frac{\delta \hat{\Omega}_{t,U}[\Sigma]}{\delta \Sigma} = 0. \quad (2.20)$$

This defines the stationary point of the grand potential as functional of the self-energy.

But how does the condition eq. (2.20) justify?

First, one introduces the Luttinger-Ward functional $\hat{\Phi}_U[G]$ defined in Ref. [58], which maps the dynamic Green's functions to a static quantity. Evaluated at the exact (physical) Green's function $G_{t,U}$ described by the above Hamiltonian, it gives a quantity $\hat{\Phi}_U[G_{t,U}] = \Phi_{t,U}$ which contributes to the grand potential of the system via

$$\Omega_{t,U} = \Phi_{t,U} + \text{Tr} \ln G_{t,U} - \text{Tr}(\Sigma_{t,U} G_{t,U}). \quad (2.21)$$

The important thing considering the Luttinger-Ward functional $\hat{\Phi}_U[G_{t,U}]$ is, that it contains all information on the interaction U and is completely determined by it, and does not depend explicitly on t (it can still depend on temperature T and chemical potential μ).

A functional derivative of it with respect to G gives

$$\frac{1}{T} \frac{\delta \hat{\Phi}_U[G]}{\delta G} = \hat{\Sigma}_U[G], \quad (2.22)$$

which is again a functional of the Green's function. Evaluated at the physical Green's function, it gives the physical self-energy $\Sigma_{t,U}$ of the system. The Luttinger-Ward functional is illustrated diagrammatically in Fig. 2.3.

Eq. (2.21) can be verified by integrating over μ , shown in Ref. [54], or by a coupling constant integration [58].

$$\hat{\Phi}_U[G] = \begin{array}{c} \circ \\ | \\ \circ \end{array} + \begin{array}{c} \circ \\ \text{---} \\ \circ \end{array} + \begin{array}{c} \circ \\ \text{---} \\ \circ \\ \text{---} \\ \circ \end{array} + \dots$$

Figure 2.3: Luttinger-Ward functional $\hat{\Phi}_U[G]$. It was originally constructed diagrammatically, see Ref. [58]. Then the functional is the limit of the infinite series of closed renormalized skeleton diagrams. Dashed lines denote the interaction U and double lines the fully interacting propagators G

To proceed with the proof of the condition eq. (2.20), one inverts the r.h.s. in eq. (2.22) locally. This is possible unless the system is at a critical point for a phase transition. One uses the resulting functional $\hat{G}_U[\Sigma]$ to perform a Legendre transformation of the Luttinger-Ward functional

$$\hat{F}_U[\Sigma] = \hat{\Phi}_U[\hat{G}_U[\Sigma]] - \text{Tr}(\Sigma \hat{G}_U[\Sigma]) \quad (2.23)$$

For the functional derivative with respect to Σ one finds

$$\frac{1}{T} \frac{\delta \hat{F}_U[\Sigma]}{\delta \Sigma} = -\hat{G}_U[\Sigma] \quad (2.24)$$

Now one defines the self-energy functional $\hat{\Omega}_{t,U}[\Sigma]$:

$$\hat{\Omega}_{t,U}[\Sigma] = \text{Tr} \ln \frac{1}{G_{t,0}^{-1} - \Sigma} + \hat{F}_U[\Sigma] \quad (2.25)$$

Its functional derivative is (using eq. (2.24))

$$\frac{1}{T} \frac{\delta \hat{\Omega}_{t,U}[\Sigma]}{\delta \Sigma} = \frac{1}{G_{t,0}^{-1} - \Sigma} - \hat{G}_U[\Sigma]. \quad (2.26)$$

The root of the right hand side of this equation is a condition for the physical self-energy of the system:

$$\frac{1}{G_{t,0}^{-1} - \Sigma} = \hat{G}_U[\Sigma] \quad (2.27)$$

Thus, at the physical self-energy, also the r.h.s of eq. (2.26) should become zero,

$$\frac{1}{T} \frac{\delta \hat{\Omega}_{t,U}[\Sigma]}{\delta \Sigma} = 0, \quad (2.28)$$

q.e.d.

The above equation can only be solved using an approximation. In VCA, the approximation consists in restricting the domain of the self-energies in the functional using a so called reference

system, i.e. a cluster with some changes in the one-particle operators. The domain of self-energies is thus restricted to the self-energies of the reference system.

2.3.4 Parameters and Variational Fields Used in this Work

In this work, for the description of the reference system, we add the following variational fields to the cluster Hamiltonian, which within VCA are just used for the determination of the self-energy and then subtracted perturbatively [51]:

- staggered magnetic field

$$H_M = h_M \sum_{i\sigma} (-1)^\sigma e^{i\vec{Q}\vec{r}} c_{i\sigma}^\dagger c_{i\sigma}, \quad (2.29)$$

with $Q = (\pi, \pi)$.

- superconducting field

$$H_{SC} = h_{SC} \sum_{i,j} \frac{\eta_{i,j}}{2} (c_{i\uparrow} c_{j\downarrow} + c_{j\uparrow} c_{i\downarrow}), \quad (2.30)$$

where η is the form factor which determines the symmetry of the superconducting order parameter, in our case d-wave.

- on-site energy

$$H_n = \varepsilon_{\text{var}} \sum_{i\sigma} n_{i\sigma} \quad (2.31)$$

which is needed for thermodynamic consistency [51].

The nearest neighbour hopping $t = 1$ sets the energy scale, and we take typical values $U = 8$ and $t' = 0.3t$ (see e.g. [59]). The inter-layer hopping is chosen to be $\tilde{t} \approx 0.2$ close to the value estimated for BSCO-2212 in [43].

2.4 Results

2.4.1 Phase Diagram

The phase diagram of the bilayer model with $\tilde{t} = 0.2$ is very similar to the one of a monolayer system only. It consists of a very broad stable antiferromagnetic zone around half filling $\mu = \frac{U}{2}$ [49, 22, 60]. Here, the superconducting order parameter is zero, and the particle density

per site is 1. When going away from half filling, by changing the chemical potential, in both directions (particle and hole doping) a d-wave superconducting phase forms (Fig. 2.6). The critical chemical potential where superconductivity appears is different for particle and hole doping. Moreover, doping in both directions at some point destroys the antiferromagnetic phase, see Fig. 2.5. Antiferromagnetism is more extended for particle than for hole doping. To simulate this difference between particles and holes observed in experiments, we have introduced the next nearest neighbour hopping t' . The spectral function at half filling

$$A(k, \omega) = -\frac{1}{\pi} \text{Im} G(k, \omega) \quad (2.32)$$

on the path $[(0, 0), (0, \pi), (\pi, \pi), (0, 0)]$ in the Brillouin zone is shown in Fig. 2.4.

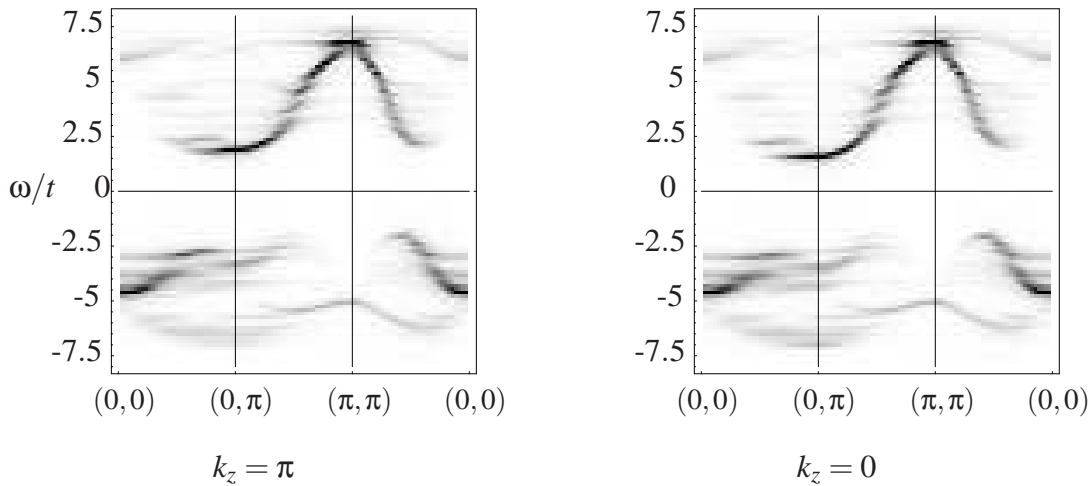


Figure 2.4: Spectral function $A(k, \omega)$ as a gray plot for the half filled bilayer Hubbard model. Results are shown for the bonding ($k_z = 0$) and antibonding ($k_z = \pi$) band.

It already hints an asymmetric behaviour of particle and hole filling in the phase diagram, since particles are expected to enter the Brillouin zone around $(\pi/2, \pi/2)$, while holes appear at $(\pi, 0)$.

At electron doping, the slope of the superconducting order parameter with doping is different from the monolayer case, in fact one can see that first one band in k-space becomes superconducting, and then the next one (Fig. 2.6(a) and 2.8). At hole doping, the inter-layer hopping seems to delay the superconducting phase transition, always as a function of chemical potential. Moreover, it shifts the range of densities, which are not realized, see Fig. 2.6(b). Note that the density is not a linear function of chemical potential μ and not even a continuous one as shown in Fig. 2.7. Our results indicate that phase separation can occur. In this case distinct phases with

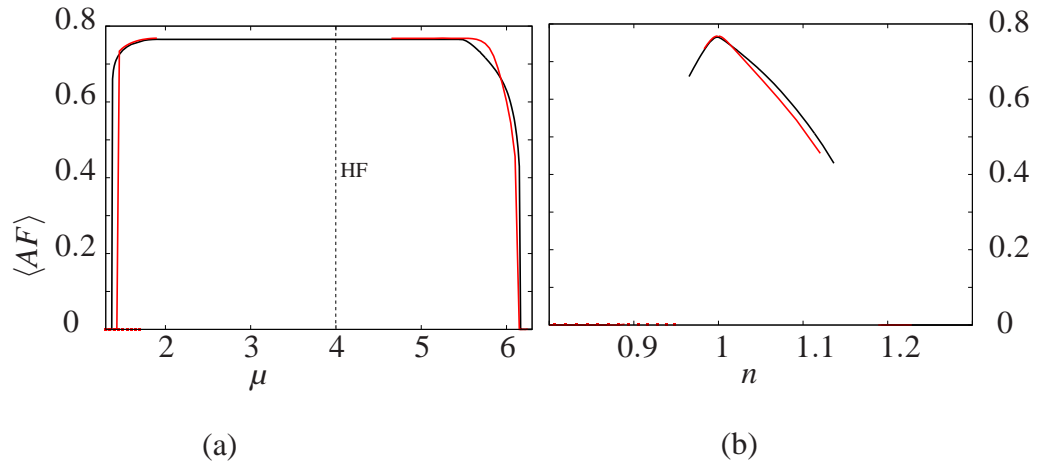


Figure 2.5: Antiferromagnetic order parameter $\langle AF \rangle$ as a function of (a) the chemical potential μ , and (b) the density n , for bilayer (black) and monolayer (red). The system is half-filled in the region around $\mu = U/2$, between $2 < \mu < 5.4$.

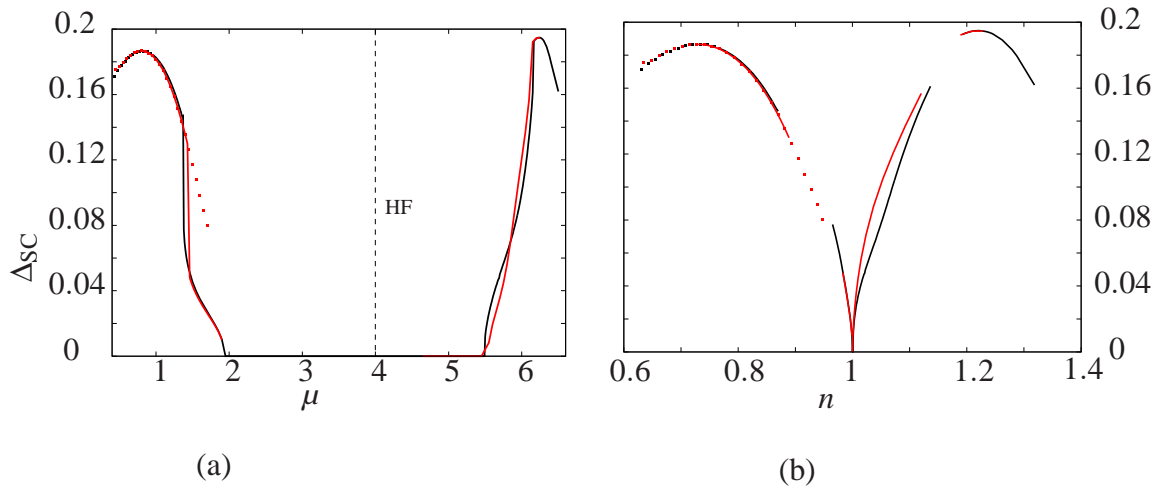


Figure 2.6: Superconducting order parameter Δ_{SC} as a function of (a) chemical potential μ and (b) doping n for bilayer (black line) and monolayer (red line). For certain doping ranges, only two parameters were varied (h_M forced to zero) (dotted lines)

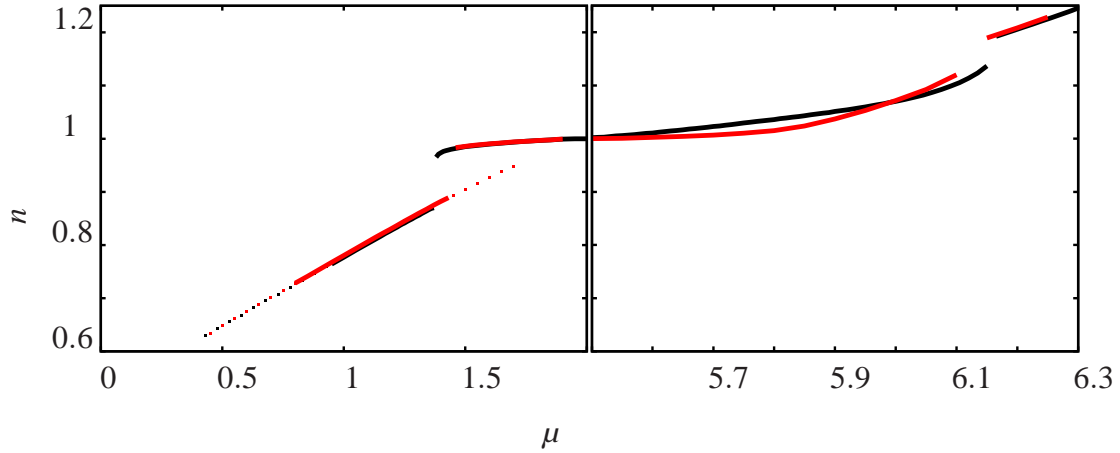


Figure 2.7: Particle density n as a function of the chemical potential μ , bilayer (black line) and monolayer (red line). The dotted line is obtained using only two variational parameters, h_{SC} and ε_{var} . The discontinuities in n are due to phase separation

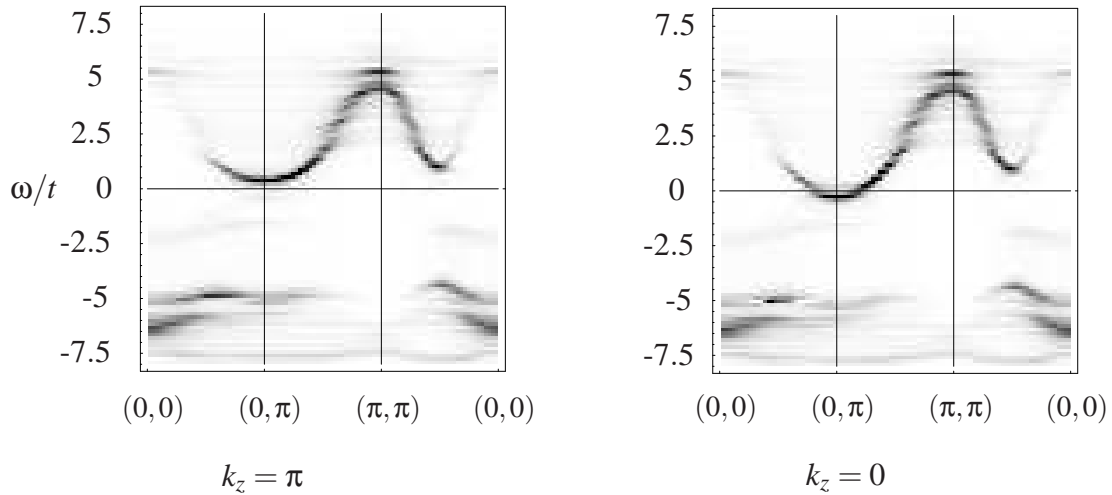


Figure 2.8: Spectral function $A(k, \omega)$ as a gray plot for electron doping, at $\mu = 5.81$. The bonding ($k_z = 0$) Fermi sheet has already crossed the Fermi surface. Thus, for $k_z = \pi$ particles are already doped into the π, π region. The antibonding band is still above the Fermi level.

different particle densities form next to each other, if a homogeneous phase is not favourable at a certain density. Then, the density averaged over a short region would be restricted to specific ranges of values. The steps in density, which we obtain as a function of the chemical potential, hint towards such a phase separation behaviour.

2.4.2 Correlation-Induced Suppression of Bilayer Splitting

Half filling The spectral function $A(k, \omega)$ at half filling is plotted in Fig. 2.4. along the path $[(0,0), (0,\pi), (\pi,\pi), (0,0)]$ in the Brillouin zone. The spectrum shows the asymmetric behavior of electron and hole filling produced by t' : electrons are expected to first enter the Brillouin zone around $(\pi,0)$, while holes first enter at $(\pi/2, \pi/2)$. The inter-layer hopping introduces a splitting of the bands into antibonding and bonding band [38]. Without correlations we would expect the splitting of the bands to be $2 * t_{\perp}(k) \frac{(\cos(k_x a) - \cos(k_y a))^2}{2}$. Looking at the Brillouin zone this means that along the diagonal $k_x = k_y$ the two Fermi points for the bonding and antibonding bands are exactly one over the other. When going away from this diagonal the splitting grows until reaching a maximum near the $(0,\pi)$ and $(\pi,0)$ points. In Fig. 2.9 we plot the density of states of the bonding and antibonding bands at $(0,\pi)$, which clearly shows the inter-layer splitting. The splitting is approximately $\Delta_U = 0.32t$, which is reduced with respect to the value $\Delta_0 = 0.4t$ in the noninteracting case.

Optimal doping At optimal doping no bilayer splitting could be resolved in ARPES measurements of BSCO-2212 [34]. In order to analyze this effect, the spectral functions for the bonding and antibonding bands at $(\pi,0)$ in the superconducting case are displayed in Fig. 2.11 for optimal doping. The total spectral function of the optimally doped system is shown in Fig. 2.10. Our calculations indeed suggest that the antibonding and bonding spectrum lie almost exactly over each other.

Moreover it was found that the shape of the quasiparticle peak in the $(\pi,0)$ region of the optimally doped monolayer (BSCO-2201) and bilayer material (BSCO-2212) are similar [34]. This is also very well reproduced in our data, as can be seen in Fig.2.11(b).

Overdoping Bilayer splitting has been measured by ARPES in several works (see. e.g. [36, 34, 35, 37]). In heavily overdoped samples the splitting is suppressed much more in the

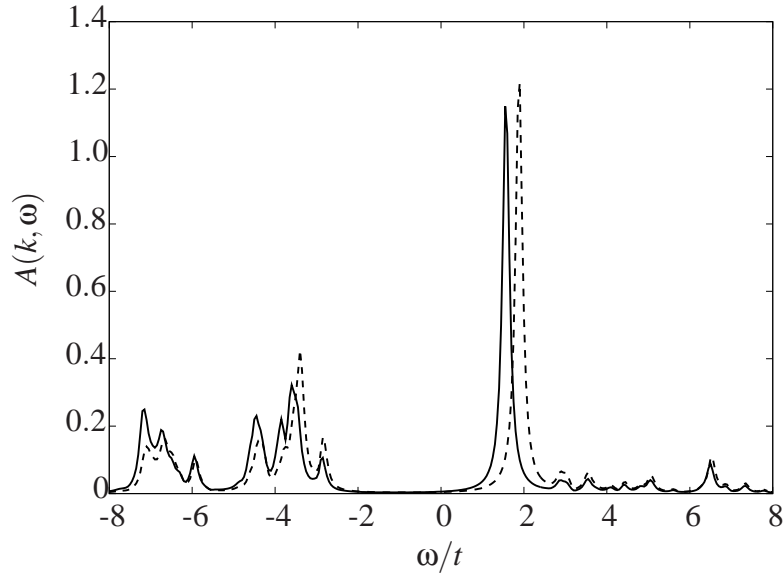


Figure 2.9: Spectral functions for the $k_z = 0$ (solid line) and $k_z = \pi$ (dashed) bands at $(0, \pi)$ (maximum bilayer splitting) at half filling.

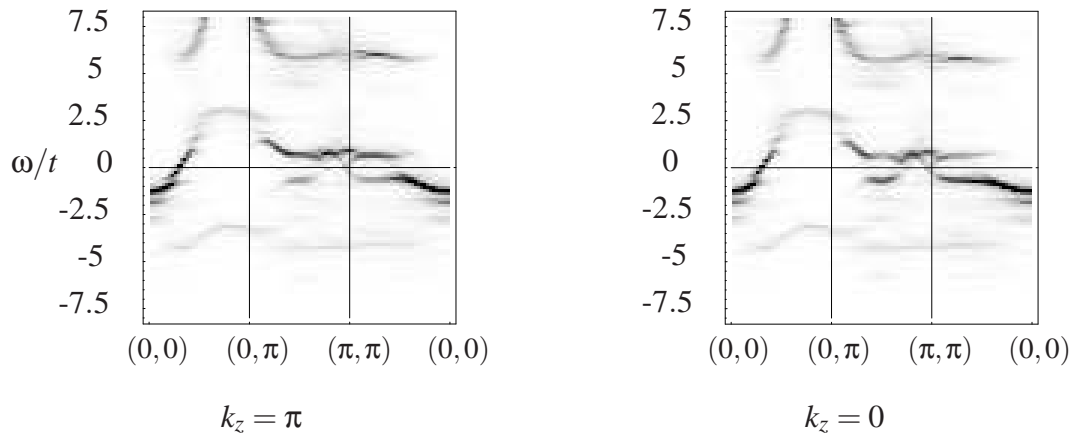


Figure 2.10: Spectral function $A(k, \omega)$ as a gray plot at optimal doping in the superconducting state. The used chemical potential is $\mu = 0.83$, where we obtained the largest superconducting order parameter.

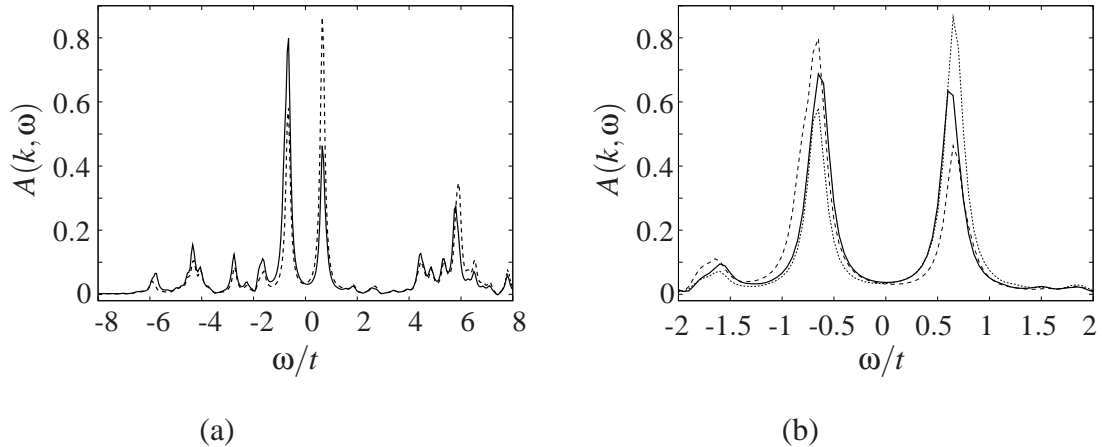


Figure 2.11: Density of states at the $(0, \pi)$ point for the optimally doped system. (a) bonding (solid line) and antibonding bands (dashed) of the bilayer. (b) comparison of bilayer bands (dashed) to the monolayer (fat solid line).

superconducting case than in the normal state, contrary to the naive expectation that a global phase coherence below T_c will enhance the c -axis coupling and thus cause larger splitting [36]. We checked these results by plotting the spectral function in the overdoped region [61] of the bilayer Hubbard model both in the normal and superconducting state. These are displayed in Figs. 2.12 and 2.13.

In Fig. 2.15, we focus on details of the energy splitting and plot its k_{\parallel} -dependence in the overdoped region. Our results suggest a reduction of the splitting at $(0, \pi)$ by about 30% in the normal and by about 70% in the superconducting phase with respect to the tight-binding model. Moreover, in the superconducting phase also the k_{\parallel} dependence is modified. This larger suppression in the superconducting phase is in qualitative agreement with experiments [36]. In order to disentangle the effects of correlation from the ones due to the superconducting gap, we also display results obtained for $U = 0$ by introducing “by hand” a superconducting symmetry breaking field equal to the one obtained variationally at $U = 8$, for the whole spectral function see Fig. 2.14.

As one can see from the figure, the superconducting gap only produces a small (about 10%) reduction, which is uniform in k_{\parallel} . The anomalous behavior of Fig. 2.15 is thus essentially due to correlations.

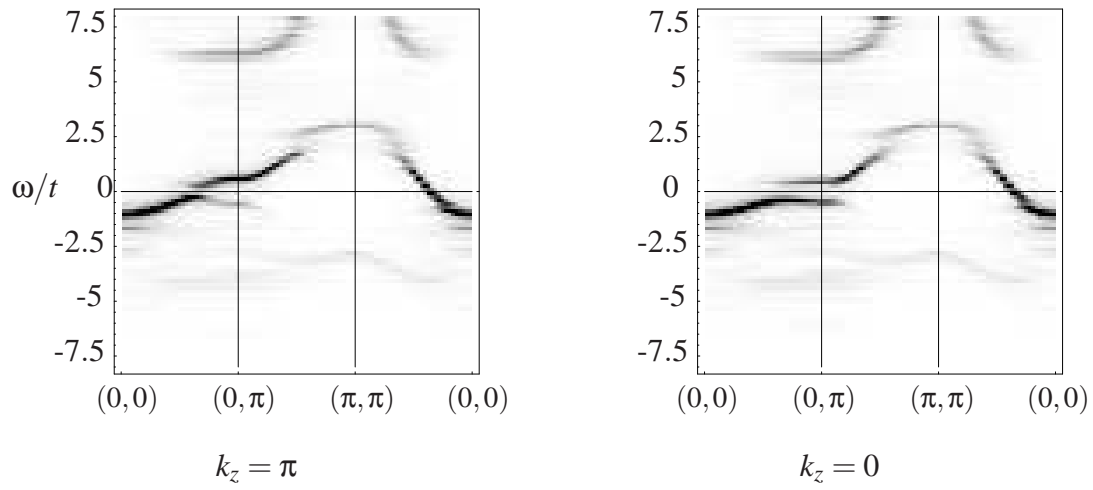


Figure 2.12: Spectral function $A(k, \omega)$ as a gray plot in the overdoped ($\mu = 0.43$) region in the superconducting phase.

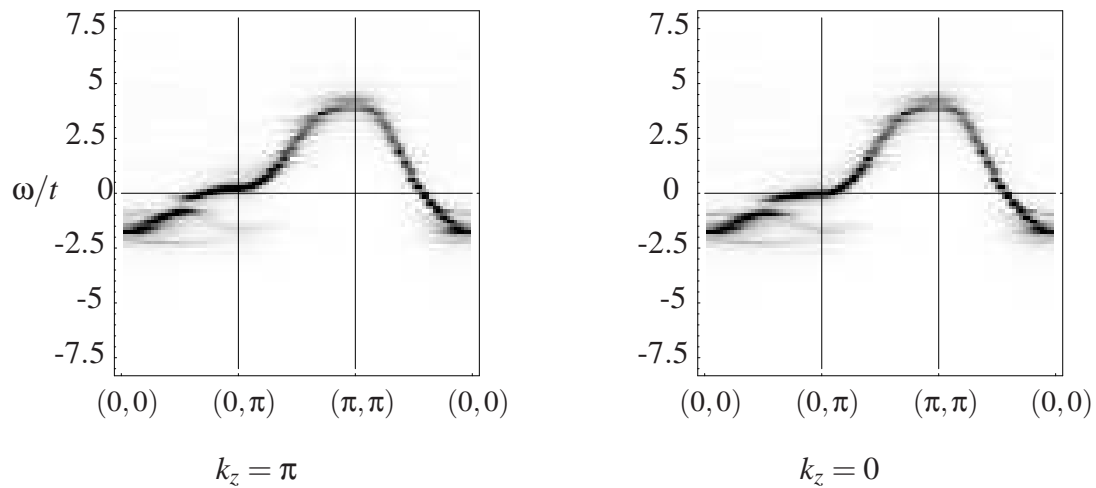


Figure 2.13: Spectral function $A(k, \omega)$ as a gray plot in the overdoped region in the normal phase.

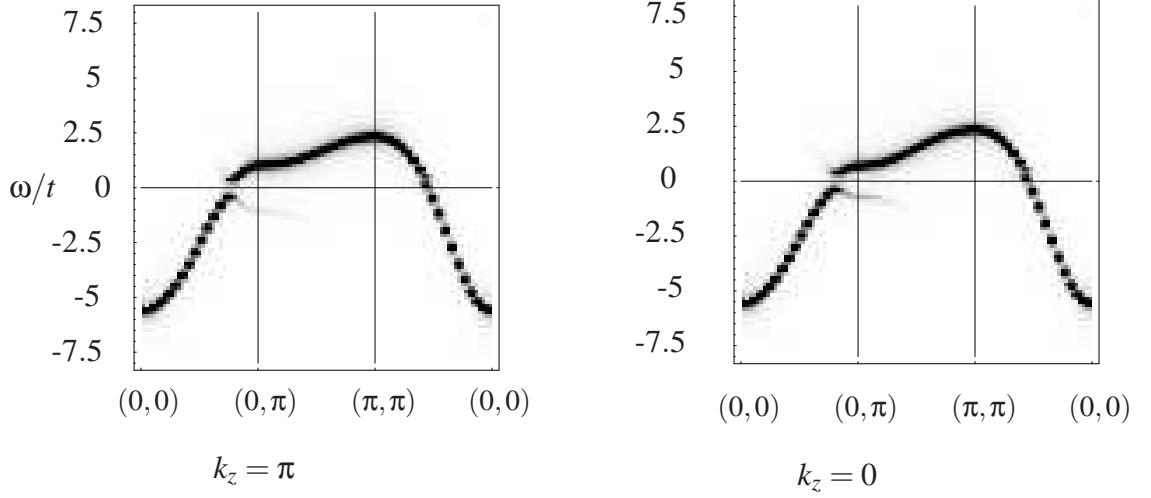


Figure 2.14: Spectral function $A(k, \omega)$ as a gray plot for $U = 0$, $\mu = 0$, imposed superconductivity (like in heavily overdoped solution). The splitting at $(\pi, 0)$ is here $\approx 0.35t$, which is already reduced from the pure TB case.

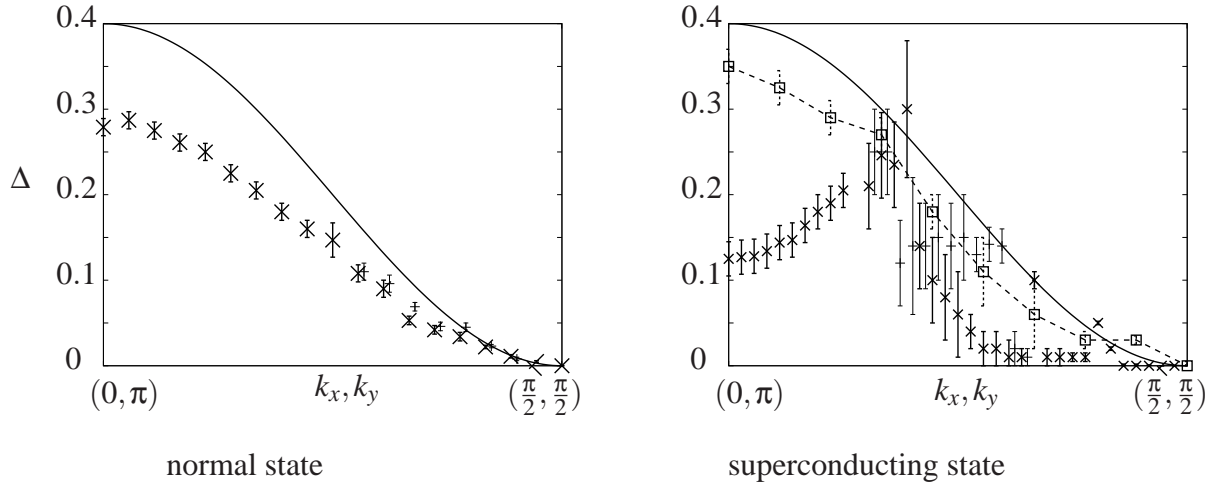


Figure 2.15: Energy bilayer splitting Δ along the line connecting $(0, \pi)$ and $(\pi/2, \pi/2)$ in the normal and superconducting state in the overdoped region (crosses and lines with errorbars). Results are compared to the splitting for $U = 0$ (solid line). In the superconducting phase we also display results obtained for $U = 0$ by introducing “by hand” a superconducting symmetry breaking field (dashed line, empty squares). At some positions in k -space the band is splitted in two features which present different bilayer splittings. For these k points we also show the second value of the splitting, shifted to the right for clarity with thin errorbars. The errorbars represent the estimated error due to the uncertainty of the peak positions.

The values of the splitting for $U = 8$ plotted in Fig. 2.15 are obtained in the following way: In the normal state there is just one prominent dispersing peak for each k_z defining a bonding and antibonding band. The k_{\parallel} dependent splitting is defined as the distance between the maxima of these peaks for $k_z = 0, \pi$, see Fig. 2.16.

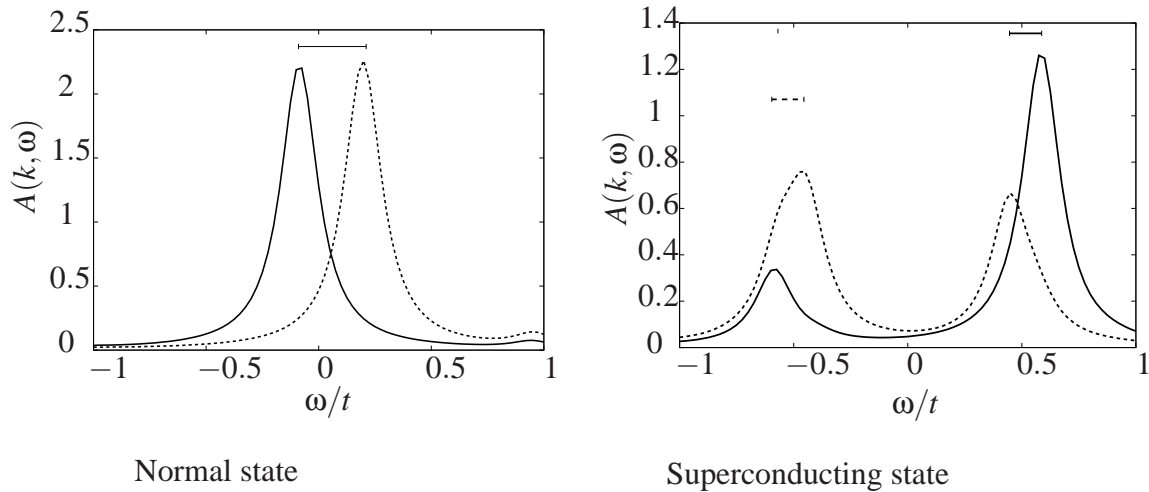


Figure 2.16: DOS for overdoped system at the antinodal $(0, \pi)$ point in k -space. Bonding (solid line) and antibonding (dashed line) bands. We have added horizontal lines to illustrate the distance between the maxima, which is the bilayer splitting.

When going away from the antinodal point, each quasiparticle peak first broadens, which introduces an error in the determination of Δ , and then evolves into a two peak structure, which resembles the peak-dip-hump structure that is observed in ARPES [36]. Measuring the distance between the second pair of peaks gives a second set of data points, which is also displayed in the Figures. For the superconducting state we plot the splitting for the quasiparticle states below the Fermi level. We have checked that it very close to the splitting of the mirror states above it.

2.5 Discussion

The simulation of a complex solid state using a simple model and solver in our case leads to spectral functions and a phase diagram that are in qualitative agreement with experimental results. In this section we want to point out, where we have made approximations and with what effect. We distinguish between approximations made by the choice of the model and those introduced when solving it using VCA.

2.5.1 Physics to Model

(1) Map to Hubbard Model As pointed out in Section 1.3, we use a single-band Hubbard model to describe the complex happenings in the CuO_2 layers of HTSC. This surely is a strong simplification, which has however already been used by many groups, and leads to qualitative agreement with experimental results [21, 22, 23]. Moreover, only the CuO_2 layers are included in the simulation, neglecting the additional rare-earth or transition-metal atoms. These are generally assumed to merely act as charge reservoirs.

(2) Neglecting the Inter-Cell Hopping In z -direction we only consider the hopping between layers in one unit-cell, but not the hopping between different unit cells. We thus in fact describe a pure monolayer or bilayer, and not the 3D compound. The inter-cell hopping that we neglect is known to be much smaller than the inter-layer hopping, due to the larger inter-cell Cu-Cu distance, resulting in weak but non-vanishing k_z dispersion [30]. If the extension of superconducting solid in z -direction is large, the inter-cell hopping leads to a broadening of both the bonding and the antibonding band, thus reducing the bilayer gap size.

(3) Form of the Inter-Layer Hopping We have simplified the inter-layer hopping, as described in Section 2.2.1. In fact, the inter-layer hopping has not the same form for all bilayer HTSC compounds, we opted for a simplified version of the dependence obtained by ab-initio calculations for YBCO [38]. A more recent description of the bilayer splitting in Bi-2212, based on experimental results, can be found in Ref. [30].

(4) Neglecting Disorder We model the superconducting compound at temperature $T = 0$, thus neglecting temperature effects, like the thermal fluctuations of spins or lattice sites. Here we are

interested only in effects at very low temperatures. Moreover, we neglect phonons, which are believed to play an important role in high- T_c superconductors.

2.5.2 Solver

We now come to the systematic deviances introduced when solving the Model.

(1) Restricted Cluster Size The lattice is tiled with clusters, and the inter-cluster hopping processes are treated only perturbatively. This leads to finite size effects. One important effect is the discrete steps in cluster filling. In a 8-sites cluster, only fillings of $\frac{1}{8}, \frac{2}{8}, \frac{3}{8}, \dots, \frac{16}{8}$ are treated well, since the exact diagonalization of the cluster is made with an integral number of particles in it. This leads to steps in the density vs. chemical potential curve. We have used a variational chemical potential ϵ_{var} to correct for this finite size effect. This however leads to an overestimation of the optimal doping and superconducting order parameter, as described in Ref.[56]. Another possibility to avoid the discrete density lies in the introduction of bath sites[56, 57]. These additional sites, which can be regarded as additional parameters in the reference system, allow for continuous filling at the cluster level. Their implementation and use in VCA does however lead to a substantial additional complexity, as the author has comprehended from her attempts to take advantage of them. The main problem is the growing number in variational parameters that arise.

(2) Perturbative Treatment of Inter-Layer Hopping We have tiled the lattice with clusters, which contain sites of one layer only. Therefore, the inter-layer hopping is included only perturbatively. For $U = 0$, this would still lead to exact results, but we work at high correlation energies, $U = 8$. Treating the inter-layer hopping only perturbatively does only justify if it is small. This is certainly the case, regarding the severe problem to resolve the bilayer splitting experimentally, see e.g. [62, 63, 36, 64].

(3) Finite Number of Clusters For an optimal resolution of the spectra in k -space, one needs to take into account infinite lattice sites. We do however use only a finite number of clusters, and apply periodic boundary conditions at the end. In the variational calculation we used 18×18 clusters in the x, y plane. The optimal values of the variational parameters are expected to converge fast with number of clusters. For the calculation of the spectra, we have increased the

number of cluster to improve the resolution of the Green's functions and spectral functions in the Brioullin zone.

(4) Subset of Self-Energies In VCA, the self-energy of the physical system $\Sigma_{t,U}$ is approximated by the self-energy of the reference system $\Sigma_{t,U}$ with changed one-particle operators. One searches for a saddle point of the grand potential Ω in the subspace of the possible self-energy of the reference system. Only a variation in all one-particle parameters (even dynamic ones) makes the trial self energies fill the total space of self energies. We use a reduced space of self energies, since we have restricted to three (sometimes two) variational parameters. A consequence is that we can find only symmetry-broken phases, which we have included in our simulation. In fact, there could be other phases, like the stripe phase [65].

(5) Choosing the Right Saddle Point The solution is a saddle point in Ω . There can however exist more than one solution in the subspace of self-energies determined by the variational parameters used. A systematic analysis of the quality and validity of solutions (stationary points in Ω) obtained with VCA is found in Ref. [66]. In this work, we can find a superconducting solution, and a trivial normal-state solution ($h_{SC} = 0$). We consider here the superconducting solution, since its ground state energy is lower.

2.6 Conclusion

We have studied the bilayer Hubbard model by means of the Variational Cluster approach, a method appropriate to capture short range correlation in strongly interacting lattice systems. As expected, the interlayer hopping splits the spectrum into a bonding and an antibonding band. However, the corresponding bilayer splitting is strongly renormalized due to correlations. This is evident in the overdoped case in both the normal and superconducting phase. In qualitative agreement with ARPES measurements the suppression effect is stronger in the superconducting phase. We also found a changed k -dependence of the bilayer splitting in the overdoped superconducting sample, where the splitting is still large between around $(\frac{\pi}{6}, \frac{5\pi}{6})$, but strongly renormalized around the anti-nodal and nodal points. Surprisingly, for optimal doping, the bilayer splitting vanishes completely, as found in ARPES [34]. The phase diagram is only slightly changed from the monolayer system.

Chapter 3

High- T_c (Bi)Layer in Non-Equilibrium

3.1 Problem Statement

An area of research that recently drew renewed attention is the field of correlated quantum systems out of equilibrium. As an application, we want to treat a thin layer (mono/bi-layer) of high- T_c superconducting material where metal contacts are attached and a voltage applied, as shown in Fig. 3.1. When a constant voltage is applied, after some time a steady state evolves. This steady state should not depend on the start parameters any more.

Many questions arise when treating such a setup: Will there be a voltage treshold, below which no current flows? Does the superconducting state in the monolayer survive the attachment of electrodes, and application of voltage? How large is the critical value for the current (electric field), that is, the current (field) where the superconducting order breaks down?

We want to study this problem using an extension of the Variational Cluster Approach (VCA) described in Section 2.3.2. By expressing the non-equilibrium Green's functions within Keldysh formalism, the VCA can be generalized into a non-equilibrium capable variational approach.

The model Hamiltonian we map our problem onto is motivated in Section 3.3. However, to start with, we want to review the status quo of non-equilibrium phenomena with superconductivity in theory and experiment.

3.2 What has already been done?

In strong connection with our problem stands the c -axis transport in high- T_c materials, which is a long standing issue. C -axis charge conductance has been treated experimentally [67, 68, 69,

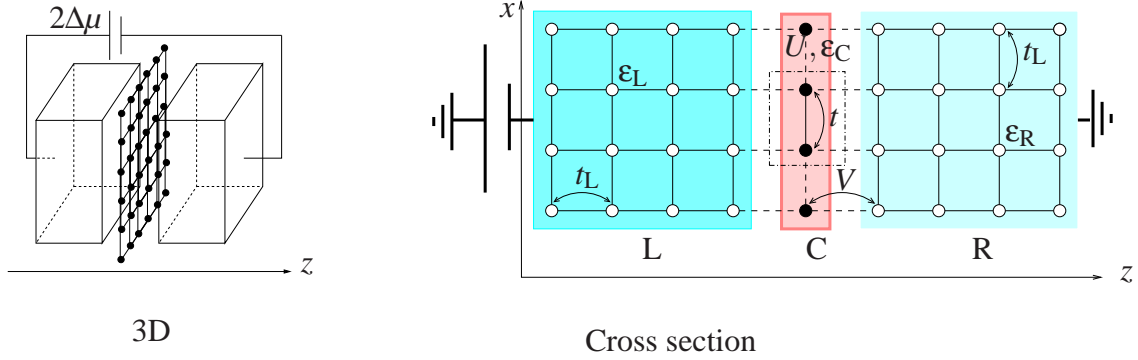


Figure 3.1: Scheme of the non-equilibrium setup discussed in this thesis. The left figure shows the 3D view. A voltage $2\Delta\mu$ is applied to a thin interacting region over two leads. On the right hand side, the cross-section along the (x, z) -plane is illustrated. The central region (pink region, C) is enclosed by two metal leads (dark and light cyan - R and L). Empty (full) circles denote uncorrelated (correlated) sites. The leads are characterized by a tight-binding Hamiltonian with nearest neighbour hopping t_L and an onsite energy $\epsilon_{L/R}$ for the left (L) and right (R) lead, respectively. The interaction between central region and leads consists of a nearest neighbour hopping, called hybridisation V , which conserves the k vector in the (x, y) -plane, denoted k_{\parallel} . In the central region, the Hamiltonian contains nearest and next-nearest neighbour hopping t, t' and additionally a strong onsite interaction, described by a Hubbard U . The central region onsite energy ϵ_C is used to fix the density at $V = 0$. The 2×2 cluster that we treat exactly, is encircled by a dash-dot line, and extends 2 sites in y direction. We distinguish hoppings treated exactly (solid lines) and perturbatively (dashed line).

70] and theoretically [71, 72, 73, 74, 75, 76], see 3.2.2 and 3.2.3 respectively. In Section 3.2.4 we review the picture of high- T_c materials as stacks of Josephson junctions [77, 78, 79, 80]. Most recently, the field effect has been used to influence the charge density in different materials and induce an insulator-superconductor phase transition [81, 82, 83, 84]. We will refer to this work in Section 3.2.5.

3.2.1 NSN junction

Our setup (see Fig. 3.1) is similar to that of a 2D normal conductor - superconductor - normal conductor, short: NSN, junction, but with a very thin layer of superconductor (a monolayer or bilayer) in the center, we will refer to it as NnSN, the small n denoting nano. Transport proper-

ties of NSN junctions have been measured by the authors of Ref. [67]. They report an increased current at almost zero bias, which they attribute to interference of conjugate electron-hole pairs and call the zero bias anomaly. Moreover, they find resistance peaks above the normal state resistance at bias voltages above $2\Delta/e$, where Δ denotes the superconducting gap, and e the electron charge.

3.2.2 Measurement of C-Axis Transport Behaviour

Resistivity of a superconducting compound is usually measured by applying voltage to electrodes attached to the material to be studied. In the normal state, the c-axis resistivity is much larger than the ab-axis one, and its temperature dependence is mostly semiconductor-like, in contrast to the metal-like ab-axis resistivity. Below the transition temperature, the resistivity is zero along both axes.

Moreover, the number of interacting CuO_2 layers per unit cell seems to influence the c-axis resistivity: Measurements of the temperature-dependent resistivities of Tl-based cuprates yielded a semiconductor-like temperature dependence for bilayer and a more metal-like behavior for monolayer (Tl-2201) materials [68]. A complementary method to find out more on the c-axis properties is to measure photon conductance, as described in Ref. [69]. For more details the interested reader is referred to the review article [70] entitled ‘‘Sum Rules and Interlayer Conductivity of High-Tc Cuprates’’.

3.2.3 Theoretical Work on the Topic

The main facts on c-axis conductivity $\sigma_c(\omega, T)$ in superconducting compounds in the normal state can be summarized in the following way [71]):

It strongly depends on the compound.

It is very low (below the minimum metallic conductivity expected).

It has a positive derivative in temperature, $d\sigma_c/dT > 0$.

There seems to be no Drude-like term in the electronic contribution to $\sigma_c(\omega)$

Among the possible explanations it has been proposed:

(1) Charge carriers in the normal state of cuprate superconductors moving along the c-axis are

damped because of the interaction with c-axis phonons [72].

(2) Some authors argue that the electrons in the CuO_2 layers can be described as Luttinger liquids. The Luttinger liquid behavior of the CuO_2 layers generates the incoherence in the tunneling process. The momentum in direction normal to the interface is not conserved [71].

Ref. [85] describes the coherent “ab” and “c” transport theory of high- T_c cuprates within a bipolaron theory. The c-axis behaviour has also been described in terms of two Fermi liquids (for the CuO_2 layers), coupled by an inter-layer term [74]. Contributions to the inter-layer Hamiltonian come from quasiparticle hopping (t_\perp), impurity scattering and bosonic scattering. This inter-layer hamiltonian was expanded to second order, to simulate the incoherence that was expected. The results agree with experimental findings, and the upturn of resistivity with decreasing temperature T is argued to be due to the freezing-out of the inelastic inter-layer scattering.

3.2.4 Stacks of Josephson Junctions

The Josephson effect evidences the coherence of the superconducting phase in a material, and has been used to check for the overlap of the superconducting order parameters between different materials, e.g. see [77]. It will allow a current of superconducting pairs to flow through a superconducting - insulator - superconductor (SIS) junction, if the order parameters overlap. Experiments described in [78, 79] show that high T_c superconductors behave like stacks of SIS Josephson junctions, where the adjacent CuO_2 planes represent the superconductors, and the region in between acts as insulator. The current-voltage characteristic of high T_c superconductors can be described by a series connection of highly capacitive junctions. We deduce that, in the superconducting state, the tunneling of pairs contributes strongly to the current.

Other experiments featuring the Josephson effect in high T_c cuprates include the work by O’Donovan et al. in Ref. [80].

3.2.5 Phase Transition by Field Effect

Most recently, the field effect has been used to influence the charge density in different materials, usually parent compounds of the high T_c superconductors, to induce an insulator-superconductor transition [81, 82, 83, 84]. Different groups applied a gate voltage to shift a superconductor from the underdoped to the optimally doped regime. In their experimental setup, there is no cur-

rent flowing through the superconductor in c -direction in the steady state, which distinguishes this setup from our simulation. Another interesting experimental setup has found light-induced superconductivity in stripe-ordered cuprate material [86].

The work that comes closest to our simulations, describes the application of fluctuation exchange [87] or FLEX + Keldysh to a thin superconducting layer between two metal contacts. The authors of Ref. [88] work in the wide band limit, and use a Hubbard model with $U/t = 4.5$ and no next-nearest neighbour hopping as central region.

3.2.6 Relevant Aspects

There are different contributions to the scattering-matrix representing an NSN junction: transmission of an electron, Andreev reflection, normal reflection of an electron, consult [89] for more details. The different mechanisms have different temperature dependences, leading to a total temperature dependence of the total current. Our simulation is done at temperature $T = 0$. This excludes thermal fluctuations and we can focus on the effect of the electric field and c -axis current. Because of the tiny size of the superconducting region in our simulation, Andreev scattering [90] should not occur, and we thus also do not expect the zero bias anomaly to appear in our simulation.

A normal material in contact with a superconductor is expected to show a small superconducting order parameter, because of the diffusion of Cooper pairs through the interface. This proximity effect has first been described by Meissner in 1960 [91]. Thus, in the setup we describe, Cooper pairs can tunnel between leads and central region, resulting in a Josephson current.

The break-down of the superconducting order parameter because of the c -axis current can originate from two effects. On the one hand, one can expect the superconducting order to vanish at a critical c -axis current I_c , since a normal current flowing through the superconducting layer generates a magnetic field, which breaks the Cooper pairs (especially for high T_c materials, because in this case the coupling presumably happens by spin fluctuations i.e. magnetic excitations). Another effect is the disruption of superconducting order by motion of the charge carriers moving perpendicular to the superconducting layer. These two effects eventually break down superconductivity. In our simulation, we neglect the magnetic field generated by the current between the leads and instead focus on the many body effects of the charge carriers themselves.

3.3 Map to Model and Organisation

The problem to be solved involves a very thin layer of high T_c material between two metal contacts, where voltage is applied, as shown in Fig. 3.1. We describe the thin layer of high- T_c material theoretically by the Hubbard model on a square lattice on the ($z = 0$)-plane, as we have already done in equilibrium in Section 1.3. For the leads, tight-binding Hamiltonians with different chemical potentials at time $\tau = -\infty$ are used. To simulate the hybridisation between superconducting layer and leads, we introduce at time $\tau = \tau_0$ a single-particle hopping in z -direction between the superconducting layer and the edge of the leads. The full Hamiltonian is thus

$$H_{\text{non-eq}} = H_R + H_L + H_C + \Theta(\tau - \tau_0)(H_{LC} + H_{CR}), \quad (3.1)$$

where H_C denotes the Hamiltonian of the superconducting layer, $H_{L/R}$ the left/right lead Hamiltonian and $(H_{RC} + H_{CL})$ the hybridisation turned on at τ_0 .

3.3.1 Model

The full Hamiltonian is illustrated in Fig. 3.1, details are given in the corresponding caption.

Leads

For the description of each lead, we use a nearest neighbour tight-binding (TB) Hamiltonian, defined on a semi-infinite cubic lattice with open boundary conditions, infinite in (x, y) , with the edge at $z = \pm 1$:

$$H_{L/R} = -t_L \sum_{\langle ij \rangle} (d_i^\dagger d_j + d_j^\dagger d_i) + (\varepsilon_{L/R} - \mu_{L/R}) \sum_i m_i, \quad (3.2)$$

with $d_i(d_i^\dagger)$ the annihilation (creation) operator on lead sites i and j , $m_i = d_i^\dagger d_i$ the particle number operator, $\mu_{L/R}$ the chemical potential, $\varepsilon_{L/R}$ the onsite energy and t_L the hopping amplitude which is the same in both leads. Additionally a sum over spin is understood. To describe non-equilibrium, we use different values of chemical potential $\mu_{L/R}$ in the left L and right R lead. In this work we apply voltage by shifting both the onsite energy and chemical potential by the same amount in one lead, and asymmetrically between the two leads. Therefore, for $\mu_L = \varepsilon_L = -\mu_R = -\varepsilon_R$, a total voltage for $2\Delta\mu$ is applied.

The leads are very large with respect to the central interacting region, and thus their state far

away from the central region remains identical to the state at $\tau = -\infty$. The Green's functions for the semi-infinite cubic nearest neighbour TB model can be obtained analytically [92], as we will point out in 3.6.

Central Interacting Region

The central region consists of a thin layer of superconducting material, described by the Hubbard Hamiltonian on a square lattice in the (x,y) -plane, which has been introduced in Section 1.3:

$$H_H = -t \sum_{\langle ij \rangle} \sum_{\sigma} (c_{i\sigma}^{\dagger} c_{j\sigma} + c_{j\sigma}^{\dagger} c_{i\sigma}) + t' \sum_{\langle\langle ij \rangle\rangle} \sum_{\sigma} (c_{i\sigma}^{\dagger} c_{j\sigma} + c_{j\sigma}^{\dagger} c_{i\sigma}) + U \sum_i n_{i\uparrow} n_{i\downarrow} + (\epsilon_C - \mu_C) \sum_{i\sigma} n_{i\sigma}, \quad (3.3)$$

in standard notation. Here we also add variational parameters according to the VCA procedure. We set $\mu_C = 0$ in all calculations and use ϵ_C to fix the density of the uncoupled central region.

Interaction of Leads and Central Layer

The Hamiltonian connecting leads to central region is

$$H_{LC/CR} = -V \sum_{\langle ij \rangle} (c_i^{\dagger} d_j + d_i^{\dagger} c_j + d_j^{\dagger} c_i + c_j^{\dagger} d_i), \quad (3.4)$$

with the hopping amplitude between leads and central region V , denoted hybridisation, and $\langle ij \rangle$ nearest neighbours terms across the interface. Additionally, a sum over spins σ is understood. We note that there are only ‘‘direct’’ terms in this hybridisation, i.e. the hopping is only in z -direction. Moreover, the hybridisation is translation invariant the (x,y) -plane, and thus preserves the k -vector in the (x,y) -plane, denoted k_{\parallel} .

3.3.2 Procedure for Solution

To solve the problem defined by this Hamiltonian, we use VCA in the space of non-equilibrium (Keldysh) Green's functions. Specifically, we proceed in the following way:

- We solve the lead Hamiltonian $H_{L/R}$ exactly at $\tau = -\infty$, where each part of the system (L,C,R) can be considered separately in equilibrium, to obtain the corresponding Green's functions $g_{L/R}$.

- We introduce variational fields in the central region Hamiltonian to have an initial state that is ‘close enough’ to the steady state that will evolve, due to hybridisation with the leads, and calculate the Green’s function g_C .
- We couple the Green’s functions of the leads to the central region Green’s function by CPT, using a Dyson equation. This has to be done in the Keldysh space, since the chemical potentials were distinct at $\tau = -\infty$.
- We repeat the procedure with different initial states, by changing the variational parameters, until the variational condition described in Section 3.10.2 is fulfilled.

3.3.3 Organisation

In Chapter 2 we have first presented the problem, and then introduced the methods before presenting the results. Here we want to proceed in a similar way, but, since there are many new instruments that we need, we have decided to tackle the problem in small steps. This means, that we will introduce the ingredients to our simulation in smaller portions and blend in simple applications where appropriate. In this way, we will evolve our method slowly and equip it with further details where necessary.

The setup we describe is infinite in (x,y) from the beginning. We first restrict to the case of a non-interacting 2D TB central region, and then introduce the hybridisation to the leads to recover the three dimensional (3D) TB model in equilibrium (Section 3.7.1). Applying voltage, we study the current vs. voltage characteristics and how they depend on the lead bandwidth. Moreover, we investigate how the particle density in the central region behaves with respect to voltage. For the noninteracting case, results are exact. However, obviously no superconductivity sets in. Therefore, in a next step, the interaction U is introduced in the central region, and we show in Section 3.9 how the current vs. voltage characteristic changes because of U .

We use VCA to improve the description of the central region with applied voltage, with respect to the results obtained by CPT coupling of leads and central region. Thus, in Section 3.10, we generalize the equilibrium Euler equation (2.27) to obtain a variational condition for the non-equilibrium setup. Then we are finally able to tackle the formulated problem: We describe a superconducting layer between metal contacts with applied voltage in the steady state. The results are presented in Section 3.12. In addition, we also apply the method to a bilayer central

region. In the end, we summarize and discuss our results on the NnSN junction.

Before even starting with the description of non-equilibrium setups we need to introduce non-equilibrium Green's functions, which we do in Section 3.4. In Section 3.5, we show how to describe a probe between contacts using CPT and Keldysh formalism. Especially the c -axis current is an important observable in such a setup. We will mention how it can be obtained. In order to calculate current and density, one needs to perform a frequency integration over Green's functions. How this can be done numerically in Keldysh space is laid out in Section 3.11.

3.3.4 Expectations

We want to investigate how c -axis current, superconducting order parameter and density in the central interacting ($z = 0$)-plane depend on the applied voltage and on the properties of the leads. We expect the c -axis current for the interacting ($U \neq 0$) and superconducting central region to be smaller than for $U = 0$, because of the gaps opening due to correlation and superconductivity. Moreover, the attached leads have a certain spectral function, which we expect to influence the central region.

Much work has already been done regarding a small, mostly zero- or one-dimensional, interacting region in non-equilibrium [93, 94, 95, 96, 97, 98, 99, 100, 101, 102]. In this work we focus on two aspects of the problem,

- (a) the fact that the interacting region is lies on a square lattice, thus the system is translation invariant in the (x, y) plane,
- (b) the variational procedure that is necessary to describe symmetry-broken phases in such a 2D interacting region.

3.4 Keldysh Formalism

We want to describe a system, consisting of two semi-infinite leads coupled to a relatively small interacting central region. At time $\tau = -\infty$, both the left L and right R lead have their own chemical potential $\mu_{L/R}$ and the hybridization V to the central region is turned off. At time τ_0 , V is switched on. We want to calculate expectation values of operators in the steady state that evolves after some time.

In contrast to a non-equilibrium system, an equilibrium system is characterized by a well-defined chemical potential, and perturbations are turned on and off adiabatically.

We present a superficial introduction to Green's functions in general and the Keldysh formalism, and refer the interested reader to standard textbooks on the topics, like [103] for equilibrium Green's functions, and [102] for non-equilibrium.

Green's functions above all consist of expectation values of two operators $A(\tau)$ and $B(\tau')$ at different real times τ, τ' , spins and places. We are presently only concerned with temporal variables, and thus suppress all other variables (spatial, spin, ...).

In equilibrium, such an expectation value of the product $\langle \mathcal{T}B(\tau')A(\tau) \rangle$, with time ordering operator \mathcal{T} , can be written as

$$\langle \mathcal{T}B(\tau')A(\tau) \rangle = \frac{\langle -\infty | \mathcal{T}B(\tau')A(\tau) | -\infty \rangle}{\langle -\infty | -\infty \rangle} = \frac{\langle \infty | \mathcal{T}B(\tau')A(\tau)S(\infty, -\infty) | -\infty \rangle}{\langle \infty | S(\infty, -\infty) | -\infty \rangle}, \quad (3.5)$$

with the time evolution operator $S(\tau', \tau)$. When going from the central expression to the right-most, we have used that in equilibrium the system is in the same state at $\tau = -\infty$ and $\tau = \infty$, $|\infty\rangle = |-\infty\rangle$, apart from a phase. Since the phases introduced in nominator and denominator by the time evolution of the ground state cancel, one can easily calculate $\langle \mathcal{T}B(\tau')A(\tau) \rangle$.

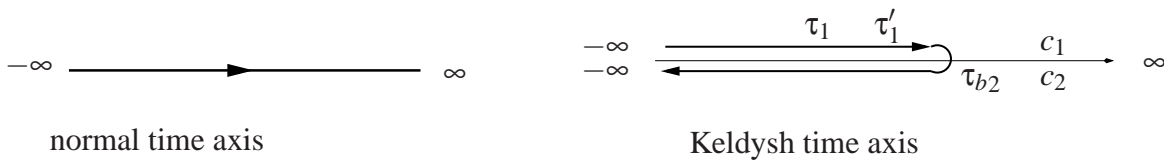


Figure 3.2: Normal to Keldysh contour. The time line is folded back to $-\infty$, with each time now additionally labeled by the side of the contour c_1, c_2 it belongs to.

Out of equilibrium, the system does not necessarily relax into the state at $-\infty$, so the states $|\infty\rangle$ and $|-\infty\rangle$ are not just different by a phase factor.

To be able to calculate expectation values, we employ the Keldysh formalism, which is derived e.g. in [1, 102] and [104]. Essentially, the time line is folded to form a new axis in time, called the Keldysh contour, which is displayed in Fig. 3.2. Then the time evolution can be performed from $\langle -\infty |$ to a specific time τ_b and back to $| -\infty \rangle$. Following this contour, the (contour ordered by \mathcal{T}_C) expectation value $\langle \mathcal{T}_C B(\tau'_1) A(\tau_1) \rangle$ can be expressed as

$$\langle \mathcal{T}_C B(\tau') A(\tau) \rangle = \langle -\infty | \mathcal{T}_C S(-\infty_1, \tau_1) A(\tau_1) S(\tau_1, \tau'_1) B(\tau'_1) S(\tau'_1, \tau_{b1}) S(\tau_{b1}, \tau_{b2}) S(\tau_{b2}, -\infty_2) | -\infty \rangle, \quad (3.6)$$

where $\tau_1(\tau_2)$ denotes that τ belongs to side 1(2) of the contour. We conclude that Green's functions, containing expectation values of the kind in eq. (3.6), now depend additionally on the side of the Keldysh contour of times τ, τ' . The dependence on the side on the contour can be folded into a 2×2 matrix, so that each Green's function can be written as

$$\hat{G}(\tau, \tau') = \begin{pmatrix} G(\tau_1, \tau'_1) & G(\tau_1, \tau'_2) \\ G(\tau_2, \tau'_1) & G(\tau_2, \tau'_2) \end{pmatrix} \quad (3.7)$$

These four parts are not independent, and by performing $\underline{G} = L\sigma^3\hat{G}L^\dagger$, a transformation in Keldysh space and rotation¹ described in Ref. [105], one can obtain the Keldysh Green's functions, which contain only three, linearly independent, parts:

$$\underline{G} = \begin{pmatrix} G^R & G^K \\ 0 & G^A \end{pmatrix}. \quad (3.8)$$

Keldysh Green's functions can be written in several ways, for alternative conventions see Ref. [105].

In this work, we use the Keldysh Green's functions \underline{G} in eq. (3.8), containing the retarded, the advanced and a ‘‘Keldysh’’ component, G^R, G^A, G^K respectively. The retarded component G^R is defined as

$$G_{AB}^R(\tau, \tau') \equiv \langle \langle A(\tau); B(\tau') \rangle \rangle^{ret} = -i\Theta(\tau - \tau') \langle [A(\tau), B(\tau')]_{-\varepsilon} \rangle, \quad (3.9)$$

with $\varepsilon = -1$ for fermions and $+1$ for bosons. The general expression for the ‘‘Keldysh’’ component is

$$G_{AB}^K(\tau, \tau') = -i \langle [A(\tau), B(\tau')]_{+\varepsilon} \rangle. \quad (3.10)$$

¹ $L = \frac{1}{\sqrt{2}}(\sigma^0 - i\sigma^2)$, and σ^i for $i = 1, 2, 3$ denote the Pauli matrices in Keldysh space, and σ^0 the unit matrix

In the steady state (or in equilibrium), \underline{G} should only depend on the distance in time. Fourier transform then allows to express the Keldysh component as $G^K = G^R f - f G^A$, where in equilibrium and for fermions, f involves the fermion distribution function [101]

$$f_F(\omega) = 1 - 2n_f(\omega) = \tanh\left(\frac{\omega - \mu}{2T}\right) \quad (3.11)$$

3.5 CPT plus Keldysh

Usually, CPT is used to handle connected identical clusters, as we have described in Section 2.3.1. However, it can also be used to treat connected non-identical clusters. The setup of the problem we want to address is sketched in Fig. 3.3 (a) and the corresponding Hamiltonian is found in eq. (3.1). Left and right lead are semi-infinite in z -direction, while the central region is a mono(bi)layer. Interaction between central region and leads takes place on two 2D (infinite) planes, as illustrated in Fig. 3.1. The single-particle Hamiltonian matrix for times after $\tau = \tau_0$ is sketched in Fig. 3.3 (b).

Note that at $\tau = -\infty$ the chemical potentials are different for left and right lead, and we thus have to resort to Green's functions in the Keldysh space, which we denote by an underline.

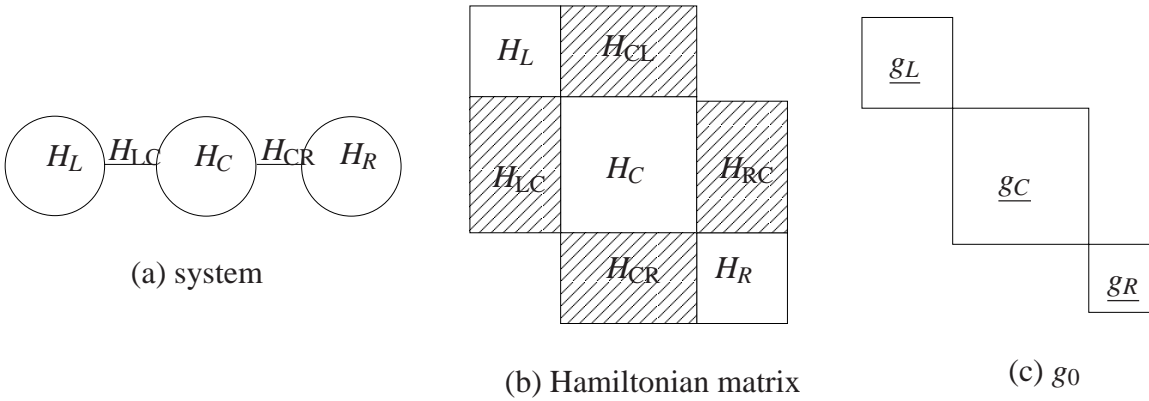


Figure 3.3: Clusters with differing Hamiltonians to be treated with CPT. In (a) we have sketched the system to be addressed. In (b) we schematically show the single-particle Hamiltonian matrix and in (c) the unperturbed Green's functions for the decoupled system at $\tau = -\infty$.

If the many-body Hamiltonian matrix is not too large, one can fully diagonalize it. Otherwise, if the inter-cluster hopping is small, the method of choice is to use CPT, i.e. treat the hybridization between the clusters perturbatively. We calculate the Green's function for each

cluster Hamiltonian H_i ($i = R, L, C$) separately, to obtain the unperturbed Green's function in Keldysh space \underline{g}_0 made up of the \underline{g}_i , see Fig. 3.3 (c). In our case, the left and right lead are in fact semi-infinitely large and so their Hamiltonian matrix is. As already pointed out in Section 3.3.1, we use the exact analytical Green's function for the edges of the leads at $\tau = -\infty$. To obtain the Green's function of the central interacting region \underline{g}_C , one has to solve a many-body problem.

We then introduce the hybridization between the regions, by a perturbation calculation:

$$\underline{G}^{-1} = \underline{g}_0^{-1} - (\hat{T}_{LC} + \hat{T}_{CR}), \quad (3.12)$$

where Green's functions and \hat{T}_{LC} and \hat{T}_{CR} are matrices in lattice sites, spin, Keldysh space and two time variables τ, τ' . The matrices containing the inter-cluster hopping $\hat{T}_{LC/CR}$, are diagonal in Keldysh space and constant in time. The usual equilibrium matrix is used for the retarded and advanced component, while the Keldysh component is empty.

In the variational calculation (described later), one needs to restrict to the central interacting region. Thus, we only calculate the full Green's function of the central region, using the following equation:

$$\underline{G}_C = \underline{g}_C + \underline{g}_C (\hat{T}_{CL} \underline{g}_L \hat{T}_{LC} + \hat{T}_{CR} \underline{g}_R \hat{T}_{RC}) \underline{G}_C, \quad (3.13)$$

where $\underline{G}_C, \underline{g}_C$ are matrices in the space of central region sites, spins, τ, τ' , Keldysh space.

Like in equilibrium, we have additionally tiled the central region with 2×2 clusters ($l_x \times l_y$), and perform a Fourier transform in the superlattice, because of its translation invariance. This procedure is well described in Ref. [24].

Then $\underline{G}_C, \underline{g}_C, \hat{T}_{CR}, \hat{T}_{CL} \dots \underline{g}_{L/R}$ are relatively small matrices in cluster sites, τ, τ' , spin and Keldysh space. On the other hand, one obtains an equation of type eq. (3.13) for each superlattice K_{\parallel} -vector, the superlattice k -vector in the (x, y) -plane. The in-plane inter-cluster hopping in the interacting region is taken into account by the hopping matrix \hat{T} , like in equilibrium (compare to eq. (2.16)).

Eq. (3.13) can also be written in form of a Dyson equation, with $\tilde{\Sigma} = \sum_{j \in L, R} \hat{T}_{Cj} \underline{g}_j \hat{T}_{jC}$:

$$\underline{G}_C^{-1} = \underline{g}_C^{-1} - \hat{T} - \tilde{\Sigma} \quad (3.14)$$

3.5.1 Steady State

In non-equilibrium, Green's functions usually depend on times τ and τ' , so generally

$$\underline{G}(\tau, \tau') = \begin{pmatrix} G^R(\tau, \tau') & G^K(\tau, \tau') \\ & G^A(\tau, \tau') \end{pmatrix} \quad (3.15)$$

We want to investigate the steady state, when Green's functions just depend on the distance in time $G(\tau, \tau') \Rightarrow G(\tau - \tau')$. Then eq. (3.14) can be Fourier transformed to obtain

$$\underline{G}^{-1}(\omega) = \underline{g}^{-1}(\omega) - \underline{\hat{T}} - \underline{\tilde{\Sigma}}(\omega) \quad (3.16)$$

which can be solved independently for each value of ω .

When considering only a single free level as central region Green's function, one can easily understand that the effect of $\underline{\tilde{\Sigma}}(\omega)$ is that of a shift of the excitations by $\text{Re} \underline{\tilde{\Sigma}}(\omega)$, and that of a broadening of the excitations of $\underline{g}^{-1}(\omega)$ provided for by $\text{Im} \underline{\tilde{\Sigma}}(\omega)$, thus changing their lifetime.

3.5.2 Current

In non-equilibrium, the evaluation of the current flowing between different sites is of great interest. For a detailed derivation of the formula for the current calculation we refer the interested reader to Ref. [102].

The current flow I_j from a site j , where particles are created (annihilated) by $d_j^\dagger (d_j)$, is described by the time evolution of the particle number operator on site j

$$I_j = -e \frac{\partial}{\partial \tau} d_j^\dagger d_j = -e i [H, \frac{\partial d_j^\dagger d_j}{\partial \tau}]. \quad (3.17)$$

H denotes the Hamiltonian of the full system and e the particle charge. Using this, one can derive an expression for the current between site j and site i [102],

$$I_{ij} = \frac{e}{2} V_{ji} \text{Re} G_{ij}^K, \quad (3.18)$$

where G_{ij}^K is the Keldysh part of the Green's function connecting sites i and j , V_{ij} denotes the corresponding hopping amplitude, and e is the charge of the particle.

We do not solve the full Hamiltonian exactly, since it is too large. Instead, we use CPT to couple the leads to the central region. To calculate the current between sites i and j , where i belongs to the left lead L and j to the central region we make use of the Dyson equation (3.12).

$$G_{ij}^K = (G_C^R V g_L^K + G_C^K V g_L^A) = (\underline{G}_C V \underline{g}_L)^K \quad (3.19)$$

Restricting to the steady state, one finds that for a small central region, which is dominated by the leads

$$I = e \int \frac{d\omega}{2\pi} \bar{T}(\omega) v_L(\omega) v_R(\omega) (f_F(\omega - \mu_L) - f_F(\omega - \mu_R)), \quad (3.20)$$

with $v_L(v_R)$ the density of states in left (right) lead and f_F the fermion distribution function. $\bar{T}(\omega)$ is the transmission coefficient of the central region, defined by $\bar{T}(\omega) = 4\pi^2 V^4 |G_C^R(\omega)|^2$. At temperature $T = 0$, the fermion distribution function becomes $\Theta(\mu - \omega)$, and we conclude that for current flow, the leads DOS need to overlap between μ_L and μ_R , as shown schematically in Fig. 3.4. In the next section, we want to find out what happens to the current and CPT equations in our specific model.

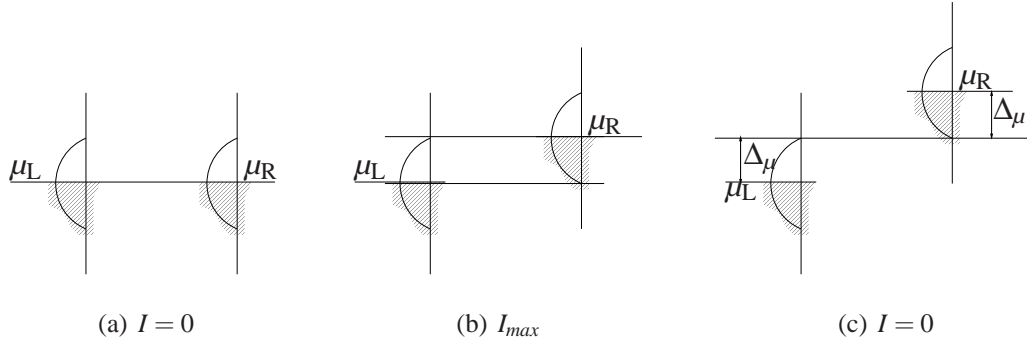


Figure 3.4: Schematic illustration of current on voltage dependence for TB leads. The grey DOS regions denote occupied states. (a) $\Delta\mu = 0$: Maximal overlap of the left and right lead DOS, i.e. $v_L(\omega)v_R(\omega) > 0$ in the whole ω range. The resulting current is however zero, because no voltage is applied ($\Delta\mu = 0$), and there is no difference in the occupation in the leads, $f_F(\omega - \mu_L) = f_F(\omega - \mu_R)$. (b) $\Delta\mu = 2t_L$: Maximal contribution to the current from the leads, since for $0 < \omega < 2t_L$ the right lead is occupied and the left lead is empty, $f_F(\omega - \mu_L) - f_F(\omega - \mu_R) \neq 0$. (c) $\Delta\mu = 4t_L$: No current can flow, because there is no overlap of the densities, $v_L(\omega)v_R(\omega) = 0$

3.5.3 Implications of Our Specific Setup

For most of our calculations we use a monolayer central region. Then, considering that the hybridization is perpendicular to (x, y) , the above formulae can be further simplified. Let us write the Dyson equation (3.13) in the space of sites of the central (x, y) -plane,

$$\underline{G}_C^{-1}(r, r', \omega) = \underline{g}_C^{-1}(r, r', \omega) - \hat{T}(r, r') - \sum_{r'', r'''} \sum_i^{\in L, R} \hat{T}(r, r'') \underline{g}_i(r'', r''', \omega) \hat{T}(r''', r'). \quad (3.21)$$

The hybridization between leads and central region in eq. (3.4) is diagonal in the space of lattice sites in the (x, y) -plane, independent of ω and identical for left and right lead, $V_L = V_R = V$. Then what remains of the sum term on the right hand side of eq. (3.21) is $\sum_{i \in L, R} V g_i(r', r, \omega) V$, and we find:

$$\underline{G_C}^{-1}(r, r', \omega) = \underline{g_C}^{-1}(r, r', \omega) - \hat{T}(r, r') - V \underline{g_L}(r, r', \omega) V - V \underline{g_R}(r, r', \omega) V. \quad (3.22)$$

Since the leads Green's function is obtained exactly and thus is translation-invariant in the (x, y) -plane,

$$\underline{G_C}^{-1}(r, r', \omega) = \underline{g_C}^{-1}(r, r', \omega) - \hat{T}(r, r') - V \underline{g_L}(r - r', \omega) V - V \underline{g_R}(r - r', \omega) V. \quad (3.23)$$

When the central region Hamiltonian can be solved exactly, too, e.g. for $U = 0$, it is also translation-invariant in (x, y) , and the last Fourier transform from cluster sites to the full k_{\parallel} -vector gives

$$\underline{G_C}^{-1}(k_{\parallel}, \omega) = \underline{g_C}^{-1}(k_{\parallel}, \omega) - \hat{T}(k_{\parallel}) - V(\underline{g_L}(k_{\parallel}, \omega) + \underline{g_R}(k_{\parallel}, \omega))V. \quad (3.24)$$

We are thus left with a set of decoupled equations, and can solve $\underline{G_C}^{-1} = \underline{g_C}^{-1} - \hat{T} - V(\underline{g_L} + \underline{g_R})V$ for each pair of (k_{\parallel}, ω) separately.

If one applies the analogous procedure to the Keldysh component in the current formula eq. (3.18), one finds that generally in the steady state, with a (x, y) translation invariant lead Green's function, the current $I(\omega)$ is proportional to

$$I(\omega) \propto \text{Re} G_{LC}^K = \sum_{r''} \text{Re} (\underline{g_L}(r - r'', \omega) V \underline{G_C}(r - r'', r', \omega))^K. \quad (3.25)$$

If the central region Green's function can be calculated exactly as well (e.g. for $U = 0$), it should be translation invariant as well, and we can Fourier transform the last equation from sites in (x, y) into k_{\parallel} to obtain

$$\text{Re} G_{LC}^K(k_{\parallel}) = \text{Re} (\underline{g_L}(k_{\parallel}, \omega) V \underline{G_C}(k_{\parallel}, \omega))^K. \quad (3.26)$$

We conclude that in this case the particles moving through the central region conserve k_{\parallel} and ω . When a current is measured, the lead Green's function has to overlap with the central Green's function for a specific frequency ω and k_{\parallel} -vector, in order for the integral over all (k_{\parallel}, ω) not to vanish.

3.6 Leads

We show here the analytic expression we use for the lead Green's function. Furthermore, we mention what has to be considered when applying a one-sided particle-hole transformation to the full Hamiltonian. Such a transformation is one possibility to allow for a superconducting variational field in the interacting layer.

3.6.1 Green's function for $\tau = -\infty$

For the simulation of the NnSN junction, we need the Green's function at the contact surface of the leads. At time $\tau = -\infty$, when the system parts are decoupled and in equilibrium, it corresponds to the Green's function at the edge of the semi-infinite cubic TB Hamiltonian.

An analytical expression for the single-particle Green's function $G(\vec{l}, \vec{m}; \gamma, \varepsilon, t_L)$ of the TB Hamiltonian on an infinite cubic lattice is derived in Ref. [92]:

$$G_\infty(l_x - m_x, l_y - m_y, l_z - m_z) = G(\vec{l}, \vec{m}; \gamma, \varepsilon, t_L) = \frac{1}{(2\pi)^3} \int_{-\pi/a}^{\pi/a} dk_x \int_{-\pi/2}^{\pi/a} dk_y \int_{-\pi/a}^{\pi/a} dk_z \times \frac{\cos[(l_x - m_x)k_x a] + \cos[(l_y - m_y)k_y a] + \cos[(l_z - m_z)k_z a]}{\gamma - \varepsilon - 2|t_L|(\cos(k_x a) + \cos(k_y a) + \cos(k_z a))}, \quad (3.27)$$

where γ is the analytic continuation of the energy ω into the complex plane, a is the lattice constant and $l_i(m_i)$ is the coordinates of lattice site $\vec{l}(\vec{m})$ in the $i = x, y, z$ direction, k_i are the corresponding wave vectors, ε is the onsite energy and t_L the hopping amplitude in the lead. We have used a notation different from Ref. [92].

Taking the Green's function of the infinite cubic lattice G_∞ and regarding the open boundary condition at $z = 0$, it can be shown [106] that the Green's function to the semi-infinite cubic lattice is

$$G_{\text{semi}-\infty}(l_x - m_x, l_y - m_y, l_z, m_z) = G_\infty(l_x - m_x, l_x - m_x, l_z - m_z) - G_\infty(l_x - m_x, l_y - m_y, l_z + m_z). \quad (3.28)$$

For the edge layer, $l_z = m_z = 1$, one finds

$$G_{\text{semi}-\infty}(l_x - m_x, l_y - m_y, 1, 1) = G_\infty(l_x - l_y, m_x - m_y, 0) - G_\infty(l_x - m_x, l_y - m_y, 2). \quad (3.29)$$

3.6.2 One-Sided Particle-Hole Transformation

We later want to use the operator of superconducting pairing field as perturbation term in the central region Hamiltonian. However, as one can see in eq. 2.30, it is an anomalous operator, i.e. it contains pair creators and annihilators and does not conserve the total particle number. It is thus convenient to transform the Hamiltonian. We apply a one-sided PH transformation to the Hamiltonian, like we have done in equilibrium.

$$c_{\uparrow} \Rightarrow b_{\uparrow}^{\dagger} \quad c_{\uparrow}^{\dagger} \Rightarrow b_{\uparrow} \quad \text{and} \quad c_{\downarrow} \Rightarrow b_{\downarrow} \quad c_{\downarrow}^{\dagger} \Rightarrow b_{\downarrow}^{\dagger} \quad (3.30)$$

By a simple calculation one can find that this causes some sign changes for parameters for one spin species. The superconducting coupling operator is transformed into a ‘‘hopping’’ with spin flip. The Green’s functions are expanded to account for these spin flip terms.

Application of the one-sided PH transformation to the Hamiltonian of the central region only, yields a two particle operator for the hybridization term:

$$V(c^{\dagger}d + d^{\dagger}c) \Rightarrow V(bd + d^{\dagger}b^{\dagger}) \quad (3.31)$$

To avoid this, the PH transformation for up spins is also done in the leads: $d_{\uparrow} \Rightarrow a_{\uparrow}^{\dagger}$, and $d_{\uparrow}^{\dagger} \Rightarrow a_{\uparrow}$. The tight-binding Hamiltonian for the left lead is now

$$\begin{aligned} H_L &= -t_L \sum_{\langle ij \rangle} (a_{i,\downarrow}^{\dagger} a_{j,\downarrow} + h.c.) + (\varepsilon_L - \mu_L) \sum_i a_{i,\downarrow}^{\dagger} a_{i,\downarrow} + t_L \sum_{\langle ij \rangle} (a_{i,\uparrow}^{\dagger} a_{j,\uparrow} + h.c.) - (\varepsilon_L - \mu_L) \sum_i a_{i,\uparrow}^{\dagger} a_{i,\uparrow} \\ &= H_{\text{TB},\downarrow}(t_L, \varepsilon_L - \mu_L) + H_{\text{TB},\uparrow}(-t_L, -\varepsilon_L + \mu_L) \end{aligned} \quad (3.32)$$

plus a constant. The right lead Hamiltonian is treated in the same way. The different spins in the lead Hamiltonian do not mix, thus the Green’s function for the down spin can be calculated as before. For calculating $\langle a_{\uparrow}^{\dagger} a_{\uparrow} \rangle$ we use the relation from [92] (page 81) to transform the Green’s function of the cubic tight-binding model in eq.(3.27):

$$G(l, m; \omega + i0^+, \varepsilon_L - \mu_L, t_L) = G(l, m; -\omega - i0^+, -\varepsilon_L + \mu_L, -t_L), \quad (3.33)$$

with ω the energy, 0^+ a positive infinitesimal (for the retarded Green’s function) ε_L, t_L the parameters of the lead Hamiltonian, and l, m the lattice sites.

This means that $\langle a_{\uparrow}^{\dagger} a_{\uparrow} \rangle$ is calculated like $\langle a_{\downarrow}^{\dagger} a_{\downarrow} \rangle$, only the energy ω has to be inverted.

3.7 Test: TB Central Region

3.7.1 Recovering the 3D TB Model

Coupling the semi-infinite leads to a 2D TB central region, in equilibrium ($\mu_L = \mu_R = \epsilon_L = \epsilon_R = \epsilon_C$) should recover the 3D TB model. The setup is in principle the same as shown in Fig. 3.1, but with a TB Hamiltonian instead of a Hubbard Hamiltonian defined on the interacting layer. We want to perform this test and use the opportunity to give information on the lead spectral function and density of states. Moreover, we calculate the current flow through a non-interacting central region, if voltage is applied. As already pointed out, the central region Hamiltonian is here of TB type

$$H_C = -t \sum_{\langle ij \rangle} \sum_{\sigma} (c_{i\sigma}^{\dagger} c_{j\sigma} + c_{j\sigma}^{\dagger} c_{i\sigma}) + (\epsilon_C - \mu_C) \sum_i n_i, \quad (3.34)$$

with c_i^{\dagger} (c_i) the creation (annihilation) operator on nearest neighbour sites $\langle ij \rangle$ in the central ($z = 0$)-plane, $n_i = c_i^{\dagger} c_i$ the particle number operator, the hopping amplitude t , the onsite energy ϵ_C and the chemical potential $\mu_C = 0$. The Hamiltonian of the 3D semi-infinite lead and the hybridization have been described in Section 3.3.1.

The DOS and spectral function for the central region decoupled from the leads ($V = 0$) is shown in Fig. 3.5, it is the solution for a TB Hamiltonian on a 2D lattice. The spectral function is obtained from the retarded Green's function according to eq. (2.32) and the density of states (per site) is calculated using

$$\nu(\omega) = \frac{1}{N} \sum_{i=1}^N \text{Im} G_{ii}^R(\omega) = \frac{1}{N} \sum_{i=1}^N \sum_{k_{\parallel}} \text{Im} G_{ii}^R(k_{\parallel}, \omega) = \sum_{k_{\parallel}} \nu(k_{\parallel}, \omega), \quad (3.35)$$

where the sum is performed over sites $i = 1, \dots, N$, and in the second step we introduced the dependence of the Green's function on k_{\parallel} .

If the central region is a bilayer, i.e. the extension in z-direction = 2 (while it is infinite in x and y), the density of states and spectral function change, see Fig. 3.6.

In this case, the spectral function consists of two parts, the antibonding band is shifted up by t , the bonding band down. The density of states is as well a sum of two (monolayer) densities, one centered around $-t$, the other around $+t$. The results are exact, since $U = 0$.

Now we change the hybridization with the leads from $V = 0$ to $V = 1$. Since the magnitude of V is equal to the hopping within the probe and the leads, $V = t = t_L$, at voltage $2\Delta\mu = 0$ and $\epsilon_C = \epsilon_{L/R} = 0$ and for times $\tau > \tau_0$ we obtain a 3D TB Hamiltonian.

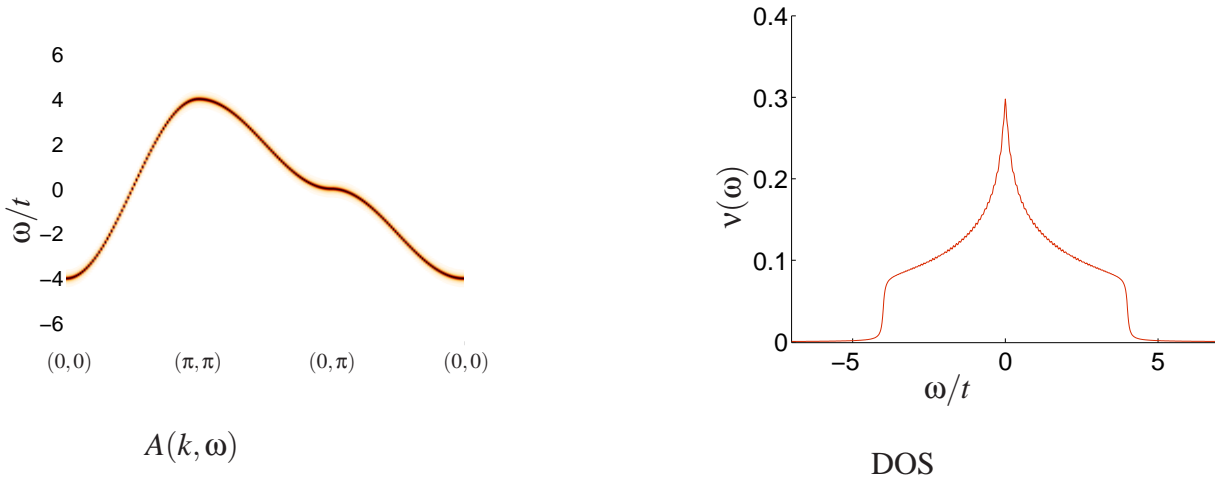


Figure 3.5: Spectral function $A(k, \omega)$ as color plot (l.h.s.) and density of states $v(\omega)$ summed over the k -vector in the (x, y) -plane, denoted k_{\parallel} (r.h.s.) for the 2D tight-binding Hamiltonian, with $t = 1$ and $\varepsilon_C = 0$.

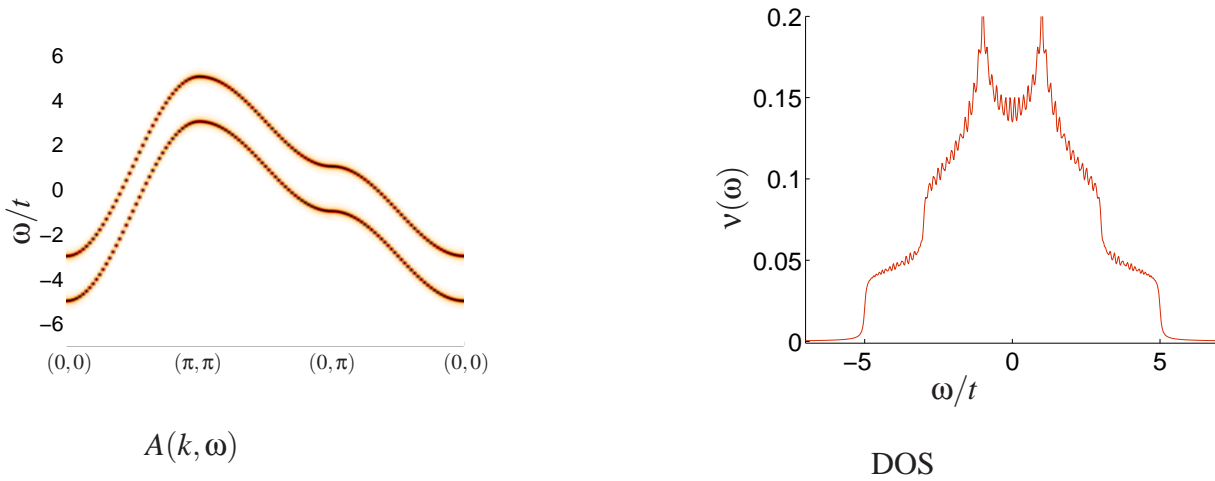


Figure 3.6: Spectral function $A(k, \omega)$ as color plot (l.h.s.) and density of states $v(\omega)$ (r.h.s) for the bilayer 2D tight-binding Hamiltonian. The oscillations in the DOS vanish if more k -points are calculated, i.e. more clusters are used in the (x, y) plane as pointed out in the Discussion 2.5.

The TB Hamiltonian contains no correlation energy ($U = 0$), thus at $2\Delta\mu = 0$ CPT solves the model exactly. Accordingly, we obtain the spectral function and DOS of the 3D tight-binding Hamiltonian, as shown in Fig. 3.7.

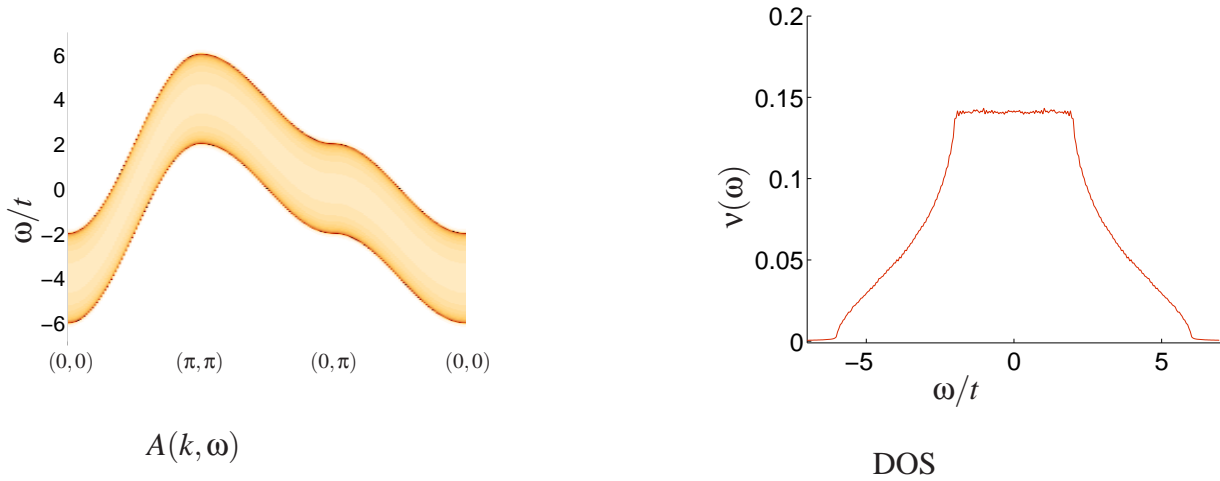


Figure 3.7: Spectral function $A(k, \omega)$ as color plot (l.h.s) and density of states $v(\omega)$ (r.h.s) of the 3D TB model, recovered by $V = t = t_L = 1$ and $\mu_{L/R} = \epsilon_C = \epsilon_{L/R} = 0$

3.7.2 Lead DOS and Dispersion Relation

Coupling to one lead only, $V_R = 0$ and $V_L = 1$, we obtain the spectral function and DOS for the edge of the semi-infinite TB model, which we use as lead. The DOS is shown in Fig. 3.8. The total bandwidth of the DOS, $\sum_{k_{\parallel}} v(k_{\parallel}, \omega)$, amounts to $12t_L$, but in fact we need to consider the k_{\parallel} -dependence in our calculations, as pointed out in Section 3.5.2.

The dispersion has the same form as the spectral function for the 2D tight-binding Hamiltonian (Fig. 3.6), namely $(-2t(\cos(k_x) + \cos(k_y)))$, see eq. (3.27). t here denotes the respective hopping amplitude. In fact, the bandwidth is $4t_L$ for each k_{\parallel} -vector.

In our simulation of the NnSN junction, we use $G_{\text{semi-}\infty}$ from eq. (3.29) to obtain the Green's function for the lead contact region $g_{L/R} = G_{\text{semi-}\infty}(l_x - m_x, l_y - m_y; 1, 1) = G_{\text{semi-}\infty}(\Delta x, \Delta y)$, where in the last step we have introduced the distance in lattice sites $(\Delta x, \Delta y)$ like in Section 2.2.1. To change the bandwidth of the leads, we will use different amplitudes for the hopping t_L .

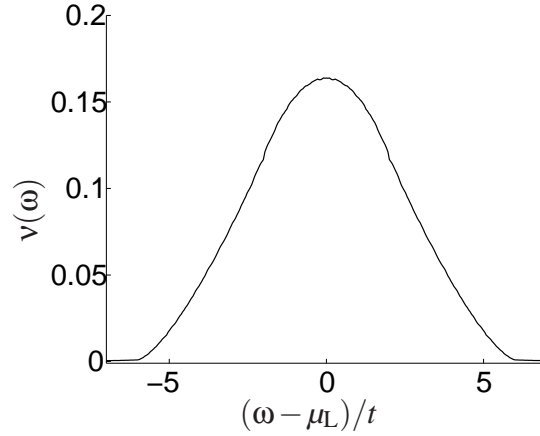


Figure 3.8: Density of states $v(\omega)$ according to eq. (3.35) in the end layer of the semi-infinite cubic nearest neighbour tight-binding model.

3.7.3 Applying Voltage

Now we apply different chemical potentials to the leads and measure the current flowing through. Like in all our later calculations we use $\epsilon_L = \mu_L = -\mu_R = -\epsilon_R$, i.e. the onsite energy and the chemical potential in the leads are changed coherently, and asymmetrically for the left and right lead. The applied voltage amounts to $\mu_L - \mu_R = 2\Delta\mu$. The current between left lead and central region per unit contact-area is measured according to eq. (3.18) and shown in Fig. 3.9 in units of the electron charge e , intra-layer hopping $t = 1$ and $\hbar = 1$ and lattice spacing $a = 1$.

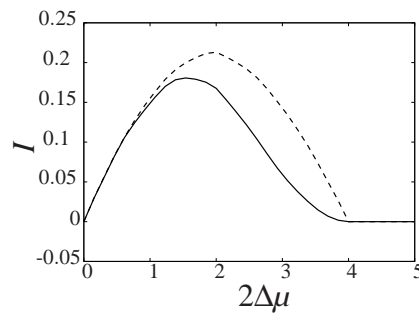


Figure 3.9: Current per unit contact-area I over potential $2\Delta\mu$ through a TB monolayer (dashed line) and bilayer (solid line) central region, for $\mu_L = \epsilon_L$ and $\mu_R = \epsilon_R$, by CPT. For the bilayer, the current is much smaller for voltages $1 < 2\Delta\mu < 4t_L$, because the bands are split and are shifted away from the center, where the leads overlap is highest. The current is in units of electron charge $e = 1$, lattice spacing $a = 1$, $t = 1$, $\hbar = 1$. All energies are in units of $t = 1$.

Let us refer to eqs. (3.20,3.26) and Fig. 3.4 to understand what happens. The overlap of left and right lead DOS is maximal at zero voltage, but here, the voltage difference is also zero, thus there can be no current. Even though the k_{\parallel} -independent bandwidth is $12t_L$, we find that current flows only in the range $0 < |2\Delta\mu| < 4t_L$. The reason is that for $U = 0$ there is no scattering and each particle conserves momentum.

3.7.4 Particle Density

When the leads are attached to the central region, and a voltage is applied, the doping or density in the central region changes. We investigate this for a TB central region. If the central region onsite energy $\varepsilon_C = 0$, the central region is half-filled and stays so, even if two half-filled leads are attached, and a voltage applied according to $\mu_L = \varepsilon_L = -\mu_R = -\varepsilon_R$. However, when the sample is not half-filled before coupling to the leads (e.g. $\varepsilon_C = -0.2$), then the resulting particle density in the central region depends on the applied voltage. We show the central region doping vs. voltage characteristics in Fig. 3.10.

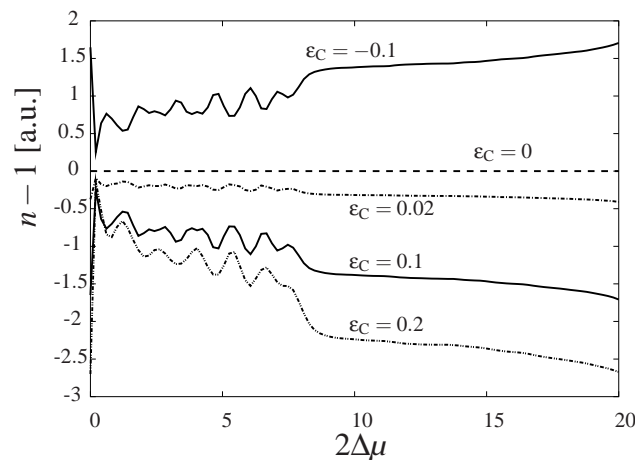


Figure 3.10: Doping ($n - 1$) in arbitrary units vs. voltage $2\Delta\mu$ for a TB central region ($U = 0$), and different small values of onsite energy ε_C for $t_L = 5$ and $V = 0.2236$, by CPT. Contrary to our other results, here we have not extrapolated the density to a broadening factor $\delta = 0$, as described in Section 3.11. The central region onsite energy ε_C is shown as label for each graph. Further conventions are as in Fig. 3.9.

Considering the effect of the leads on the central region described in eq. (3.21) one can naively expect that:

- An overlap of lead DOS and central region DOS causes a change in the central region particle density, if the filling is different.
- For density changes induced by the contact with the leads, contact with both leads is not necessary. So, the density might be changed, even when no steady state current flows.

Our results show that:

- Close to $\Delta\mu = 0$, the overlap of lead and central region bands is maximal, thus the central region density is drawn towards the leads filling (half-filling), see Fig. 3.10.
- For zero overlap, the central region filling is only related to the central region Hamiltonian, here characterized by the onsite energy ϵ_C .

3.8 Coupling Strength Γ

It is convenient to introduce a measure of the coupling between leads and central region. The coupling strength Γ is defined as

$$\Gamma_{L/R} = \pi v_{L/R} V^2 \quad (3.36)$$

where $v_{L/R} = i \text{Im } g_{L/R}^R$ denotes the density of states of the leads and V is the hybridization.

The total impact of the hybridization between the leads and the central region Green's function has been expressed in equation 3.13. If we split the leads Green's function $g_{L/R}$ into real and imaginary part we can see there are two main effects that arise because of the hybridization with the leads:

$$\pi V^2 g_{L/R}^R = -i\Gamma_{L/R} + \pi V^2 \text{Re } g_{L/R}^R \quad (3.37)$$

The real part of the lead's Green's function shifts the the excitation energy from the unperturbed central region Green's functions, while the imaginary part broadens the quasiparticle excitation, thus changing its lifetime.

The definition of the coupling strength Γ makes most sense in the wide band limit, where $v_{L/R}$ does not depend on ω and k_{\parallel} . In our simulation, we use $G_{\text{semi-}\infty}(\Delta x, \Delta y)$, the Green's function at the edge of the semi-infinite 3D TB lattice, where the resulting density v does depend on k_{\parallel} vector and energy ω . In order to facilitate a comparison of our results to those of other groups e.g. [88], we still speak about a coupling strength, and use for $v_{L/R}$ the summed DOS at $\omega = 0$, $v = \sum_{k_{\parallel}} v_{L/R}(k_{\parallel}, 0)$.

For hopping $t_L = 1$ in the TB leads, the density of states $v_{L/R}$ around $\omega = 0$ is about 0.16. When changing the lead bandwidth, we find that v is inversely proportional to t_L .

3.9 Effect of Lead Bandwidth and Interaction U

Here we investigate how the current vs. voltage characteristic is influenced by (a) the form of the lead density of states and (b) interaction U in the central interacting layer. Therefore, we add an interaction term $U \sum_i n_{i\uparrow} n_{i\downarrow}$ to the TB Hamiltonian on the central layer and calculate the current vs. voltage characteristic for different values of hopping amplitude in the leads t_L . The Hamiltonian of the central region is

$$H_C = -t \sum_{\langle ij \rangle} \sum_{\sigma} (c_{i\sigma}^{\dagger} c_{j\sigma} + c_{j\sigma}^{\dagger} c_{i\sigma}) + (\epsilon_C - \mu_C) \sum_i n_i + U \sum_i n_{i\uparrow} n_{i\downarrow}. \quad (3.38)$$

3.9.1 Non-Interacting Central Region

First, we set $U = 0$ and focus on the effect of the hopping amplitude in the leads t_L . t_L fixes the bandwidth of the leads, the total bandwidth being equal to $12t_L$, as shown in Section 3.7.1. The results are shown in Fig. 3.11(a). Note that current again only flows in the $0 < 2\Delta\mu < 4t_L$ range, as pointed out in Section 3.7.3, and that the current peaks around $2\Delta\mu \approx 5$ and then starts to decrease quickly.

Fig. 3.11(b) shows how the central region influences the current vs. voltage characteristic: We change the hopping amplitude t in the central region and note, that the maximum of the current flow for wide lead bands (here $t_L = 9$) is achieved at $2\Delta\mu = 4t$. At this voltage, all central region states contribute to the current flow.

3.9.2 Interacting Central Region

For the description of superconductivity we need to introduce a term of onsite interaction in the Hamiltonian, the so called Hubbard U , motivated in Section 1.3. Without interaction U we can not have superconductivity. Here, however, the central region is interacting but not superconducting. The method we apply is CPT.

Figure 3.12(a) shows the current vs. voltage for different values of interaction U . We find that the current in the $0 < 2\Delta\mu < 4t_L$ voltage range decreases with growing correlation energy U .

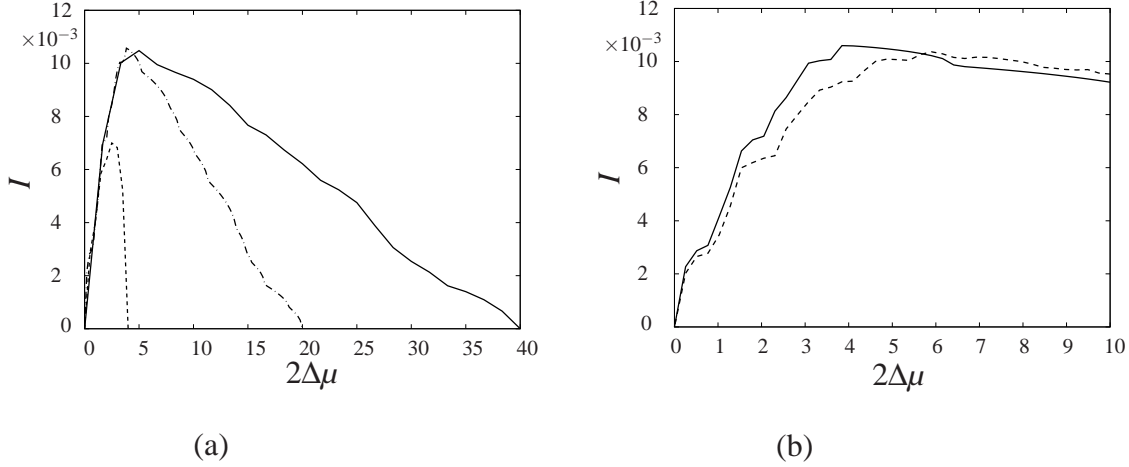


Figure 3.11: Current per unit contact-area I vs. voltage $2\Delta\mu$ through a TB monolayer central region ($U = 0$), by CPT.

(a) Results for constant coupling strength $\Gamma = 0.005$ but different lead bandwidth, $t_L = 10$ (solid line), $t_L = 5$ (dashed with dots) and $t_L = 1$ (dashed). Note the range where current flows is $4t_L$ wide. (b) Results for constant coupling strength $\Gamma = 0.005$, $t_L = 9$, and two different values of central region hopping $t = 1$ (solid line) and $t = 1.5$ (dashed line). Further conventions are as in Fig. 3.9.

However, for $U > 0$ a second feature appears for $2\Delta\mu > t_L$, which grows with interaction U . The cluster size we use here and later is $2 \times 2 \times 1$ ($l_x \times l_y \times l_z$). For the current calculation we make an extrapolation in the broadening factor δ , as described in Section 3.11.

In Fig. 3.12(b) the dependence of the current vs. voltage characteristic on the onsite energy of the center region ϵ_C is illustrated. Whereas for $\epsilon_C = 0$ the second peak is only small, for $\epsilon_C = -U/2$ (half-filled central region at $V = 0$) the first peak loses much of its intensity and the second (broad) peak is emphasized. This can be explained by considering the spectral function of the central region: For $\epsilon_C = 0$ a lot of spectral weight can contribute for small voltages, while at half-filling, the Hubbard bands have been shifted away from $\omega = 0$, which reduces the current in the first peak regime. One could also say, that for $\epsilon_C = 0$ the double occupation should be small and so the effects of U are small.

The use of wide lead bands should put forward the effect of the interaction U on the interacting region. We set $t_L = 9$ and plot the corresponding current vs. voltage characteristics in Fig. 3.13. We find that for the originally half-filled central layer the current peaks at $\Delta\mu \approx 2 \times 4$ and

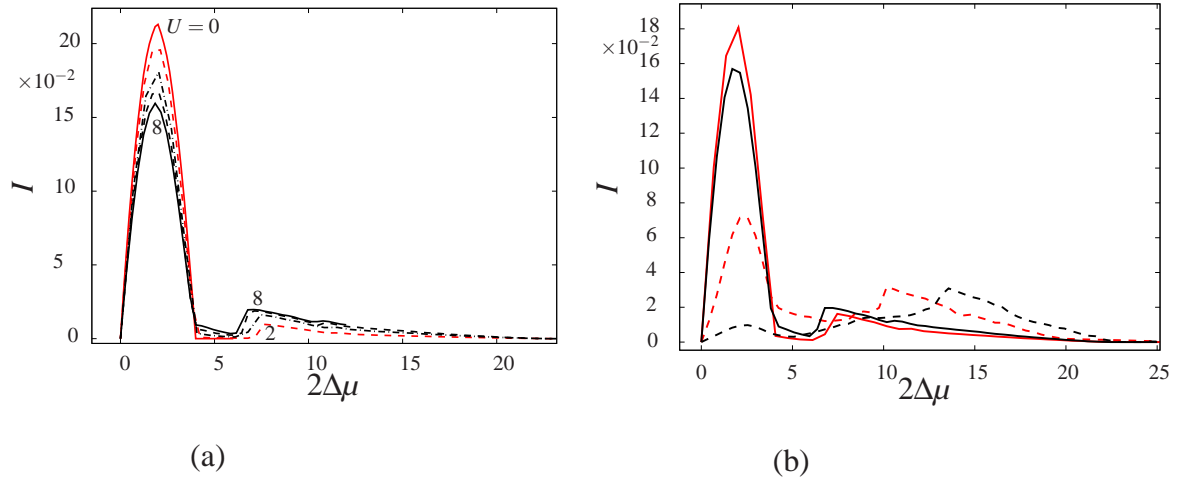


Figure 3.12: Current I per unit contact-area vs. voltage $2\Delta\mu$ through a non-superconducting interacting monolayer with nearest neighbor hopping $t = 1$, by CPT. The hybridization is $V = 1$, so for correlation energy $U = 0$ we retrieve the TB solution shown in Fig. 3.9. (a) Results for different values of $U = 0, 2, 4, 6, 8$, and onsite energy $\epsilon_C = 0$. (b) Results for a originally half-filled central layer $\epsilon_C = -U/2$ (dashed lines) and $\epsilon_C = 0$ (solid lines) and different interaction values $U = 8$ (black) and $U = 4$ (red). Further conventions are as in Fig. 3.9.

$\Delta\mu \approx 2 \times 7$. For the central layer shifted away from half-filling by the onsite energy $\epsilon_C = -2$, the peaks are found at $\Delta\mu \approx 2 \times 2$ and $\Delta\mu \approx 2 \times 6$. The corresponding spectra at half-filling and hole doping (in equilibrium) are shown in Figures 2.4 and 2.13, however with $t' = 0.3t$ while we use $t' = 0$ here. The amount of current obviously depends on whether the Hubbard bands can contribute or not.

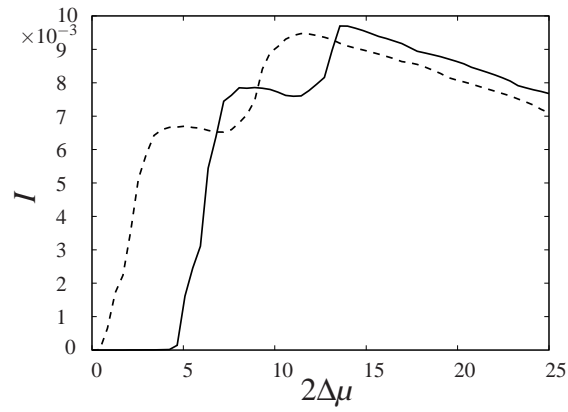


Figure 3.13: Current I vs. voltage $2\Delta\mu$ through an interacting non-superconducting central layer with nearest neighbor hopping $t = 1$ and onsite interaction $U = 8$, half-filling $\epsilon_C = -4$ (solid line) and $\epsilon_C = -2$ (dashed line), by CPT. The leads have wide bands, $t_L = 9$, and the hybridization amounts to $V = 0.3$. Further conventions are as in Fig. 3.9.

3.10 Variational Cluster Approach for Non-Equilibrium

Now that we have introduced all ingredients for the description of a non-equilibrium system, like the Keldysh formalism, the leads TB Green's function, and how to calculate the current, we turn towards the variational calculation.

CPT [24, 25] allows to treat large systems with strong local correlations. It is exact in three limits, for correlation energy $U = 0$, for dimension $N = \infty$ and for hopping $t = 0$. For the description of symmetry-broken phases like antiferromagnetism or superconductivity, CPT has been extended to the VCA. VCA has been successfully applied to a wide range of problems [48, 50, 51, 22] and proven to be exact in certain limits in the framework of SFT [52, 53]. A description of CPT and VCA in equilibrium has been given in Chapter 2, Sections 2.3.1 and 2.3.2.

Non-equilibrium setups present a new playground, with all kinds of problems, including e.g. short time dynamics [107], or the steady state [100]. They can be treated using the Keldysh formalism, introduced in Section 3.4, where the time dependence of each function is folded into a matrix. For short times, the CPT + Keldysh [107] works well, since a voltage turned on for a short time $\Delta\tau$ represents a small perturbation $V\Delta\tau$, which we already know that CPT is up to. VCA + Keldysh has already been used to describe the steady state, which evolves when the voltage has been turned on for some time [100]. In that case, variational parameters have been included that serve to minimize the difference between the “initial” reference cluster solution and the final steady state. The corresponding self-consistency condition was to minimize the cluster to CPT difference for expectation values of the operators corresponding to the variational parameters.

But what if one wants to include symmetry-broken phases in the start configuration? We present here the application of a variational condition which allows to treat a symmetry broken phase, e.g. superconductivity, in the central region. We describe this new condition in Section 3.10.2. The theory and parts of the results will be published in Ref. [108].

3.10.1 Variational Cluster Approach + Keldysh

We will again step through the VCA procedure, treated in Section 2.3.2, and hope the vigilant reader apologizes the repetitions. The starting point is a central region Hamiltonian H , defined

on a lattice geometry. In order to be able to treat the strong correlations exactly, a cluster is chosen which can be solved exactly or by Lanczos diagonalization, and the Hamiltonian is split into a cluster and intercluster part, $H = H_{\text{CL}} + H_{\text{inter-CL}}$. H_{CL} is complemented by fields of arbitrary one-particle operators summarized in $H_{\vec{\lambda}}$,

$$H'_{\text{CL}} = H_{\text{CL}} + H_{\vec{\lambda}} \quad (3.39)$$

$$H'_{\text{inter-CL}} = H_{\text{inter-CL}} - \delta_{a,b} H_{\vec{\lambda}} \quad (3.40)$$

where $\delta_{a,b}$ denotes that $H_{\vec{\lambda}}$ is diagonal in cluster indices a, b . The variational fields $H_{\vec{\lambda}}$ help to make the dynamics of the cluster problem coincide with the exact dynamics of the system. The advantages that arise when using variational fields $H_{\vec{\lambda}}$ are listed in 2.3.2. Using the SFT one can show that finding a saddle point in the grand potential as a function of the variational parameters $\vec{\lambda}$ gives an approximation to the true ground state of the system, see Section 2.3.3 or [52, 53].

In order to account for the interaction with the leads, we have to consider the hybridisation with the leads Green's function in the perturbation calculation: The Green's function of the central region \underline{g}_{C} is coupled to the Green's functions of the leads $\underline{g}_{\text{L/R}}$,

$$\underline{G}_{\text{C}}^{-1} = \underline{g}_{\text{C}}^{-1}(\vec{\lambda}) - \hat{T}(\vec{\lambda}) - \hat{T}_{\text{CL}} \underline{g}_{\text{L}} \hat{T}_{\text{LC}} - \hat{T}_{\text{CR}} \underline{g}_{\text{R}} \hat{T}_{\text{RC}}. \quad (3.41)$$

The chemical potential in the leads $\mu_{\text{L/R}}$ is not uniform at time $\tau = -\infty$, which hinders the treatment of this problem with the usual (equilibrium) Green's functions. Thus we use Green's functions in the Keldysh space, marked by the underline.

3.10.2 Variational Condition

The problem that now arises is the question as to how to choose the right values of the variational parameters $\vec{\lambda}$. In equilibrium we look for a saddle point in the grand canonical potential in the space of variational parameters $\vec{\lambda}$. In non-equilibrium, however, the grand canonical potential is not defined.

A simple self-consistency criterion is to ask for values of variational parameters, that make the difference between the corresponding expectation values in the reference system (defined by H'_{CL}) and the original system (defined by H , and calculated using CPT) vanish. We will denote the Green's functions and their observables by cluster/CL/reference system and lattice/CPT, respectively, and express this condition as $\langle A_i \rangle_{\text{CL}} = \langle A_i \rangle_{\text{CPT}}$, where A_i is the single-particle

operator to which the variational parameter λ_i is the coefficient. When using a variational onsite energy ϵ_{var} , this condition asks for a value of ϵ_{var} that results in equal densities in the reference system and the lattice (CPT) Green's functions. This self-consistency criterion has already been used and proved helpful [109, 100]. It corresponds to some kind of minimizing the “difference” between the initial state at $\tau = -\infty$ and the final (steady) state. [100].

A variation of all possible parameters (including dynamic ones) would lead to perfectly equal Green's function in reference system and lattice, $\underline{g}_{\text{C}}(\vec{\lambda}) = \underline{G}_{\text{C}}$

Does the condition $\langle A_i \rangle_{\text{CL}} = \langle A_i \rangle_{\text{CPT}}$ work for our problem?

We found, that the condition $\langle A_i \rangle_{\text{CL}} = \langle A_i \rangle_{\text{CPT}}$ does not work with superconductivity as variational field, introduced as h_{SC} in eq. (2.30). The problem is, that the superconducting field causes (new) anomalous terms in the Green's function to emerge. These contain information

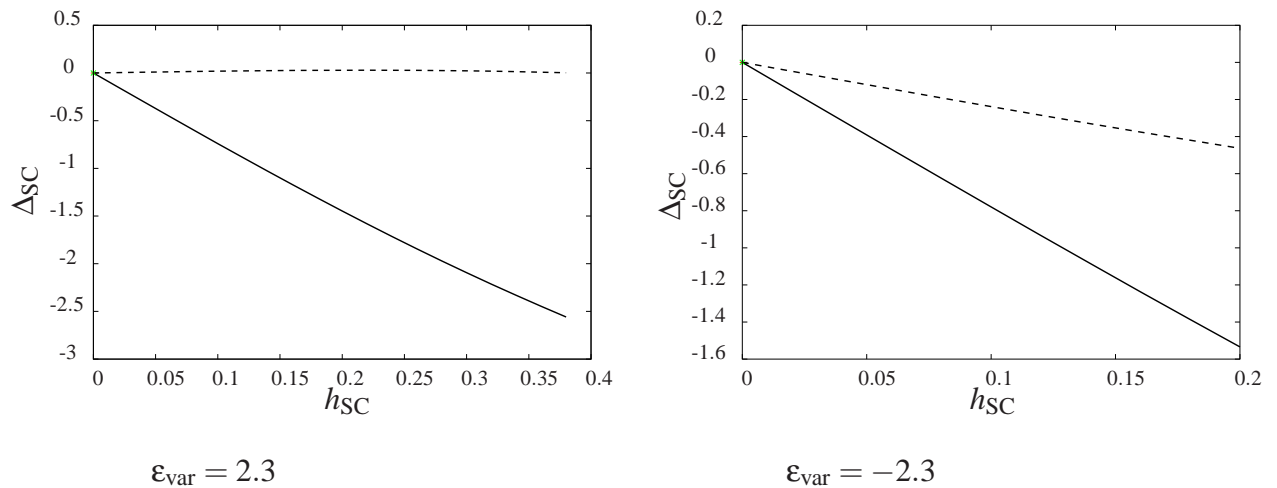


Figure 3.14: Expectation value of the superconducting order parameter Δ_{SC} , in reference cluster (solid line) and lattice (dashed line) vs. variational pairing field h_{SC} at two different values of variational onsite energy ϵ_{var} . The central region is the monolayer Hubbard model with $U = 8$. The onsite energy of $\epsilon_{\text{C}} = -1.7$ moves the system away from half-filling, so that it can be superconducting. On the l.h.s. the variational onsite energy of $\epsilon_{\text{var}} = -2.3$ shifts the reference system back to half-filling, where superconductivity is not favoured. When subtracting the field again, the system is doped and the superconductivity order parameter could be larger than in the (half filled) reference system. It is, however, not like that.

on the dynamics of the pair creation $c_i^\dagger c_j^\dagger$ and pair annihilation $c_i c_j$. If the pairing field term is

set to zero, the expectation values in reference system and lattice are both zero. Thus, there is always a solution at zero pairing field. We did not succeed in finding any other but this trivial solution. The perturbation calculation reduces the magnitude of the anomalous Green's function terms, and we claim there cannot be another but the zero solution for superconductivity, for the discussed type of self-consistency.

Fig. 3.14 features the results of our search for a non-trivial solution to $\langle H_{\text{SC}} \rangle_{\text{CL}} = \langle H_{\text{SC}} \rangle_{\text{CPT}}$, where H_{SC} is the superconducting pairing operator.

A New Variational Condition

Since we cannot equalize the expectation value of the pairing field in cluster and lattice, we need a new criterion for the search of the stationary point. We introduce an expression, which is analogous to the equilibrium Euler equation in eq. (2.26).

$$\int \frac{d\omega}{2\pi} \text{Tr} \hat{\sigma}_1 \frac{\partial \underline{\Sigma}}{\partial \lambda_i} (\underline{g}(\vec{\lambda}) - \underline{G}) = 0 \quad (3.42)$$

where $\hat{\sigma}_1$ is the Pauli matrix in Keldysh space, and $\frac{\partial \underline{\Sigma}}{\partial \lambda_i}$ is the derivative of the cluster self-energy with respect to the variational parameters λ_i , which is a subset of the set of one-particle parameters t' of the reference system H'_{CL} . $g(\vec{\lambda})$ and G are the reference cluster and lattice Green's functions of the central region, respectively. Eq. (3.42) describes a vector of the same size as $\vec{\lambda}$. The expression can be written as

$$\int \frac{d\omega}{2\pi} \text{Tr} \left[\frac{\partial \Sigma^{\text{R}}}{\partial \lambda_i} (g^{\text{K}}(\vec{\lambda}) - G^{\text{K}}) + \frac{\partial \Sigma^{\text{K}}}{\partial \lambda_i} (g^{\text{A}}(\vec{\lambda}) - G^{\text{A}}) \right] = 0. \quad (3.43)$$

and the part in square brackets is the Keldysh part of

$$\frac{\partial \underline{\Sigma}}{\partial \lambda_i} (\underline{g}(\vec{\lambda}) - \underline{G}). \quad (3.44)$$

The analogous Euler equation for equilibrium has been derived in Refs. [54, 53]. We feature the derivation in Appendix A.

For non-equilibrium we have replaced the self-energy and Green's functions by their counterparts in Keldysh space. This would give us a 2×2 matrix with the three entries (Keldysh, advanced and retarded). The main standing question is how to conduct the trace in the Keldysh space. In this work, as variational condition, we use the Keldysh component of the matrix in Keldysh space. A check showed exact accordance with equilibrium results for an uncoupled

system, see Fig. 3.15.

As variational parameters we take the superconducting pairing field h_{SC} and a variational onsite energy ε_{var} in the central region. These have been introduced in Section 2.3.4. Every additional parameter makes the search in the parameter space much more complicated, therefore we restrict to these two variational parameter, and renounce the use of an antiferromagnetic field.

We calculate the derivative of the reference cluster self-energy $\underline{\Sigma}$ according to

$$\begin{aligned} \frac{\partial \underline{\Sigma}(\vec{\lambda})}{\partial \lambda_i} &= \frac{\underline{\Sigma}(\vec{\lambda}|\lambda_i + \Delta\lambda) - \underline{\Sigma}(\vec{\lambda}|\lambda_i - \Delta\lambda)}{2\Delta\lambda} = \\ &= \frac{g_U^{-1}(\vec{\lambda}|\lambda_i + \Delta\lambda) - g_U^{-1}(\vec{\lambda}|\lambda_i - \Delta\lambda) - g_0^{-1}(\vec{\lambda}|\lambda_i + \Delta\lambda) + g_0^{-1}(\vec{\lambda}|\lambda_i - \Delta\lambda)}{2\Delta\lambda}, \end{aligned} \quad (3.45)$$

with $\Delta\lambda = 0.005$ and $\underline{g}_{U/0}$ the cluster Green's functions with correlation energy U and 0 respectively.

For a check, we simulated the equilibrium setup with a series of input parameters (like U and ε_C). Both the non-equilibrium program that uses equation (3.43) and the equilibrium program using equation (2.18) yield the same results for variational parameters and expectation values of operators. However, the frequency integral in eq. (3.43) has to be done in an appropriate way. We find that a poor integration, with not enough $k_{||}$ -vectors or energy steps, leads to oscillations of the expression in the variational condition in equation (3.43) as a function of ε_{var} .

3.11 Frequency Integration over Objects in Keldysh Space

Frequency integration of Green's functions as required for the evaluation of the variational condition eq. (3.42) faces us with a problem: the Green's functions have poles at the excitation energies.

3.11.1 Equilibrium

In equilibrium, there are several possibilities to carry out such a frequency integration, described in Refs. [103, 50, 51, 22, 110, 111], among them the Q-matrix technique [50] and the direct sum over Matsubara frequencies [110]. When investigating the equilibrium problem in Chapter 2,

we have distorted the integration path to an appropriate contour in the complex frequency plane, as discussed in [111].

In non-equilibrium, the Keldysh Green's functions have poles not just on one side of the real axis, but on both. This makes the integration more difficult, and the usual methods can not be applied.

What can be done, is to replace the infinitesimal 0^+ by a finite δ to shift the poles away from the real axis, up (down) for retarded (advanced) poles, and integrate directly over the real axis. Of course, a finite δ does not give the exact result any more. But the expression in equation (3.43) does show a linear dependence on δ for values of δ larger than a threshold, which depends on the accuracy of the integration. For very small values of δ we resolve the features of the single cluster.

In fact, we have to keep in mind that there are two limits to be taken:

- (a) thermodynamic limit: lattice (and cluster) to infinity
- (b) reduction of the error introduced by non-zero δ

The limits have to be taken in the listed order. To (a): The use of a finite cluster size results in delta peaks, e.g. in the self-energy and the Green's functions. A finite δ causes a broadening of the peaks and thus simulates an infinite (or larger) lattice. On the other hand, the finite δ makes the frequency integration less accurate. We settled for the following procedure for calculating the expression in eq. (3.43). Integrations over Keldysh objects to obtain observables like current and density are done in the same way.

- The integration is performed for two different values of δ (namely 0.03 and 0.045).
- The “virtual” result at $\delta = 0$ is extrapolated linearly.

The appropriate values of δ can be found by plotting the “gradient” in eq. (3.42) as a function of ϵ_{var} . A wavy curve signals that the chosen δ -values are too small to compensate for the finite size effect, or the integration in ω needs more supporting points. The wavy dependence on ϵ_{var} comes from the integration over the derivative of delta peaks in the self-energy. We need the function smooth enough to be able to find a root using the Newton Raphson algorithm.

For the integration in ω we use a Gauss-Legendre integrator, instead of an adaptive integrator, since there are two expressions in eq. (3.42) for the two corresponding variational parameters, to be integrated at the same time.

The pairing field and the hybridisation to the leads should help to make the integration in ω space simpler, since both terms are expected to broaden the features.

Comparison To Equilibrium VCA Results: We have used an equilibrium Hubbard model to test the above method of frequency integration over functions in Keldysh space. Extrapolating the variational condition in eq. (3.42) for finite values of δ to $\delta = 0$ gave good accordance with equilibrium VCA results. Moreover, we found that the extrapolation of observables to $\delta = 0$ helps to reproduce the values obtained by the equilibrium frequency integration.

This is shown in Fig. 3.15 for the density, the observable which belongs to the particle number operator.

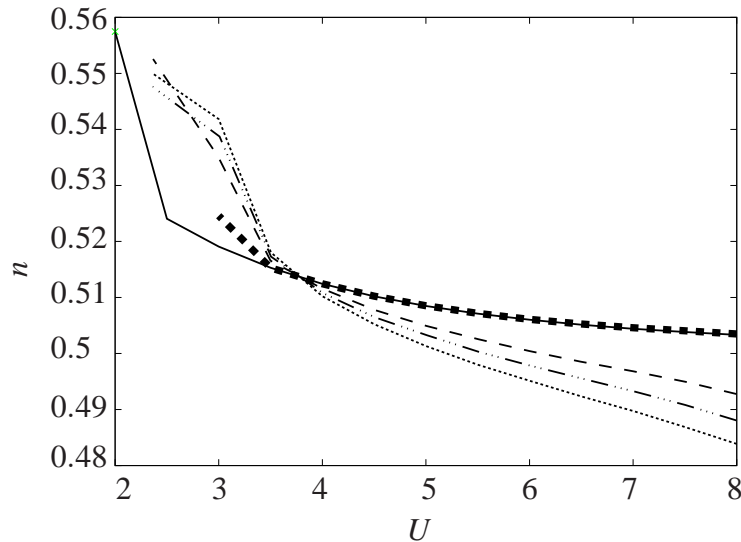


Figure 3.15: Density n vs. correlation energy U for a monolayer Hubbard model in equilibrium, with $\mu = U/2$ and $t'/t = 0.3$, by CPT. We compare results from the equilibrium frequency integration (black squares) [111] and direct real axis integration used for non-equilibrium. The density obtained by the non-equilibrium ω integration is shown for $\delta = 0.12$ (dotted line), $\delta = 0.09$ (dashed-dotted) and $\delta = 0.06$ (dashed line). Note the $\delta = 0$ extrapolated density (solid black line) corresponds well with former results for correlation energies $U > 3.5$. For smaller U it would have been necessary to adapt δ and the integration accuracy.

3.12 NnSN in Non-Equilibrium: Results

We present here the results we obtained when simulating a NnSN junction, using the non-equilibrium variational method introduced in Section 3.10. The setup is illustrated in Fig. 3.1, and the full Hamiltonian has been described in Section 3.3.1. Some of the results will be published in [108]. The contribution of coauthor M. Knap to this work was to furnish the author with a basis for the code needed to do this work. The coauthor developed the code to investigate 2D non-equilibrium setups, like the one described in Ref. [100].

The most important parameter, in addition to the parameters of the central region Hubbard model, is the coupling strength Γ , defined in Section 3.8. For our simulations we have chosen two different values of Γ , namely $\Gamma = 0.005$ and $\Gamma = 0.01$.

Another group used the fluctuation exchange approximation (FLEX) in Keldysh space to describe a similar setup [88]. They choose $\Gamma = 1 \times 10^{-3}$, and report that for $\Gamma > 0.1$ no superconducting ordering takes place.

We represent the central superconducting region by a Hubbard monolayer or bilayer in the ($z = 0$)-plane. We will first describe the results obtained for the monolayer, and in the next section show how we investigated the bilayer superconducting interacting region. In Section 3.12.3 we present what we obtain for the a nearest-neighbour Hubbard monolayer, which is the same interacting layer as used by the authors of Ref. [88]. At the end, we summarize our results on the NnSN junction in non-equilibrium.

3.12.1 Monolayer as Central Region

We have carried out calculations for $\Gamma = 0.01$ with two different lead bandwidths: The results for a narrow lead bandwidth, $t_L = 1$, and those for a wide bands, $t_L = 9$, are both given in Section 3.12.1.1. The large lead bandwidth allows to focus on the influence of the central region features, and to compare with [88]. In Section 3.12.1.2 we show results for a weaker coupling strength $\Gamma = 0.005$, and wide lead bands.

While the parameters determining the interaction with the leads are different for each data set, the central region is always the same as the one in the equilibrium problem, i.e. eq. (3.3) with parameters $U/t = 8$ and $t'/t = 0.3$. The central region onsite energy ϵ_C is used to fix the initial density, which is the density of the central region before the hybridisation with the

leads happens. The chemical potential μ_C is zero. We use four different values for ϵ_C , namely $\epsilon_C = -1.4, -1.5, -1.6, -1.7$. When the central region is decoupled from the leads, for each value of ϵ_C one obtains a specific initial density n_0 in the superconducting state. The uncoupled interacting layers are always hole-doped, with densities $n_0(\epsilon_C)$ in the superconducting state ranging from optimal doping to underdoping: $n_0(-1.4) = 0.887$, $n_0(-1.5) = 0.914$, $n_0(-1.6) = 0.934$ and $n_0(-1.7) = 0.954$.

For each value of ϵ_C , we do variational calculations for a series of applied voltages up to the voltage where the superconducting order parameter Δ_{SC} has vanished. The results obtained are shown in various figures to make clear the dependencies of the most important quantities on each other, namely the current I flowing perpendicular to the central region, voltage $2\Delta\mu$, superconducting order parameter Δ_{SC} and density n . The current through an infinitely large surface is of course infinitely large. Thus, when speaking about current I we in fact mean the current per unit contact-area, in units of electron charge $e = 1$, hopping $t = 1$ and $\hbar = 1$ and lattice spacing $a = 1$. The observables are obtained by δ extrapolation, as explained in Section 3.11.

The nature of the variational condition is such, that there can exist more solutions (saddlepoints). In equilibrium, we ruled out additional saddlepoints by comparing their corresponding energies. Here we show both solutions that we find, one with normal-state and the other with superconducting central region. For the coupling strengths Γ that we have chosen, and our central region parameters, the superconducting solution vanishes at some voltage treshold, while we always find a normal state solution.

3.12.1.1 $\Gamma = 0.01$, Narrow and Wide Lead Bands

Narrow Lead Bands We start with narrow lead bands, $t_L = 1$. In order to reach a coupling strength of $\Gamma = v(0)\pi V^2 = \sum_{k_{\parallel}} v_{L/R}(k_{\parallel}, \omega)|_{\omega=0}\pi V^2 \approx 0.01$, we set the hybridisation to $V = 0.145\dot{6}$. On the next pages, we show various figures featuring the dependencies of current I , central region density n , superconducting order parameter Δ_{SC} and applied voltage $2\Delta\mu$ on each other. We describe them and summarize the main points at the end.

Fig. 3.16 shows the current vs. voltage characteristics. If one oversees the smaller features, the dependence of current on voltage (in the voltage range shown) is almost linear. What surprises us, is, that different initial densities may lead to different amounts of current is some

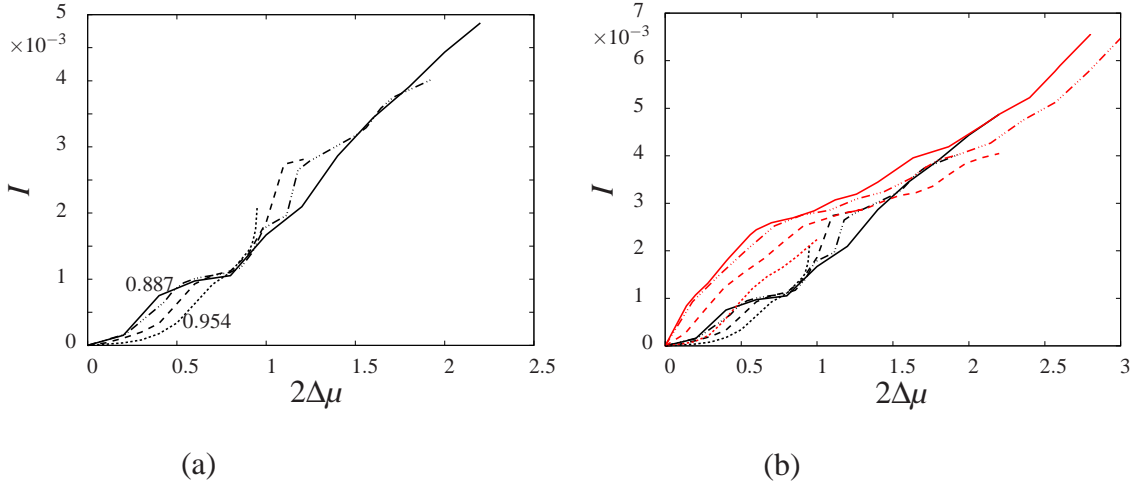


Figure 3.16: Current I per unit contact-area vs. voltage $2\Delta\mu$ through a Hubbard monolayer, for $\Gamma = 0.01$ and narrow lead bands $t_L = 1$, by VCA. Four values of ε_C are used to fix the initial density, and the other parameters of the Hubbard model are $U/t = 8$, $t'/t = 0.3$ and $\mu_C = 0$. In (a) and (b), the black lines represent the current through the superconducting central region for different initial densities. The upper and lower bound of the initial densities n_0 are noted next to the graphs. In (b) the current through the normal state central region is additionally shown (red lines).

The different dashed denotes different central region onsite energies ε_C , $\varepsilon_C = -1.4$ (solid line), $\varepsilon_C = -1.5$ (dash-dotted line), $\varepsilon_C = -1.6$ (dashed line), $\varepsilon_C = -1.7$ (dotted line). All energies are in units of the intra-layer hopping $t = 1$, and the current is in units of $a = 1, e = 1, t = 1, \hbar = 1$.

regions (e.g. at voltage $2\Delta\mu \approx 0.5t$), or to only one value, e.g. at $2\Delta\mu \approx 0.8t$.

In Fig. 3.16(b) we compare the current through the superconducting and normal-state central region. We find, that in the superconducting state the current is reduced. We attribute the reduction to the superconducting gap, which impedes states at the Fermi energy in the $(\pi, 0)$ region to emerge. These states would contribute a lot to the current.

In Fig. 3.17(a) we present the dependence of superconducting order parameter on voltage. The superconducting order parameter decreases when voltage is applied, the main fall-off happening around $2\Delta\mu \approx 1$. This is in the order of the gap size obtained in VCA. Superconductivity has totally vanished for $2\Delta\mu = 2$.

The changes in the central region density are illustrated in Fig. 3.17(b). In the superconducting state, the density change is much smaller than in the normal state, where doping happens

almost linearly with voltage, in the featured voltage range. Here one can also see, that the central region initial density is in fact not the same for the superconducting and the normal state: In the normal state, the identical onsite energy ϵ_C leads to a density much closer to half filling.

In Fig. 3.24(b) we will plot the density vs. voltage characteristics for a much larger range of voltages. The linear behaviour does not continue until $n = 0$, but instead there are two peaks of minimal density at $2\Delta\mu \approx 4$ and $2\Delta\mu \approx 9$, more or less where there are maxima in the current flowing. As pointed out already in Section 3.9.2, these are the regions, where the Hubbard bands are overlap with a large density of states in the leads.

The relation of current and density is displayed in Fig. 3.18. In the normal state, we can observe an almost linear dependence of doping $n - 1$ on current, especially for voltages $2\Delta\mu > 0.6$, but not so in the superconducting state.

In Fig 3.19(a) we see the superconducting order parameter vs. density. For equivoltage line $2\Delta\mu = 0$ we have used equilibrium data, where the central region is not coupled to the leads. Unlike field effect experiments, we observe that changes in the central region density towards optimal doping do not lead to a larger superconducting order parameter.

Fig. 3.19(b) illustrates the superconducting order parameter vs. current behaviour. One could say, that the effect of the transverse current on the superconducting order parameter is qualitatively similar to the effect of temperature or magnetism.

Let us summarize:

- The current through the superconducting central region is smaller than through the normal state central region. We can attribute this reduction to the gap, that hinders the emergence of states at the Fermi energy.
- In the superconducting state, at some values of voltage, the current does not depend on the initial density of the central region. Taking a closer look, we found that at these points, for all different central-region onsite energies ϵ_C , the variational onsite energy ϵ_{var} corrects ϵ_C to only one value of effective cluster onsite energy.
- When the applied voltage reaches the size of the superconducting gap, the superconducting order parameter is reduced or destroyed, depending on the coupling strength Γ .
- The effect of the transverse current on the superconducting order parameter qualitatively resembles that of temperature.

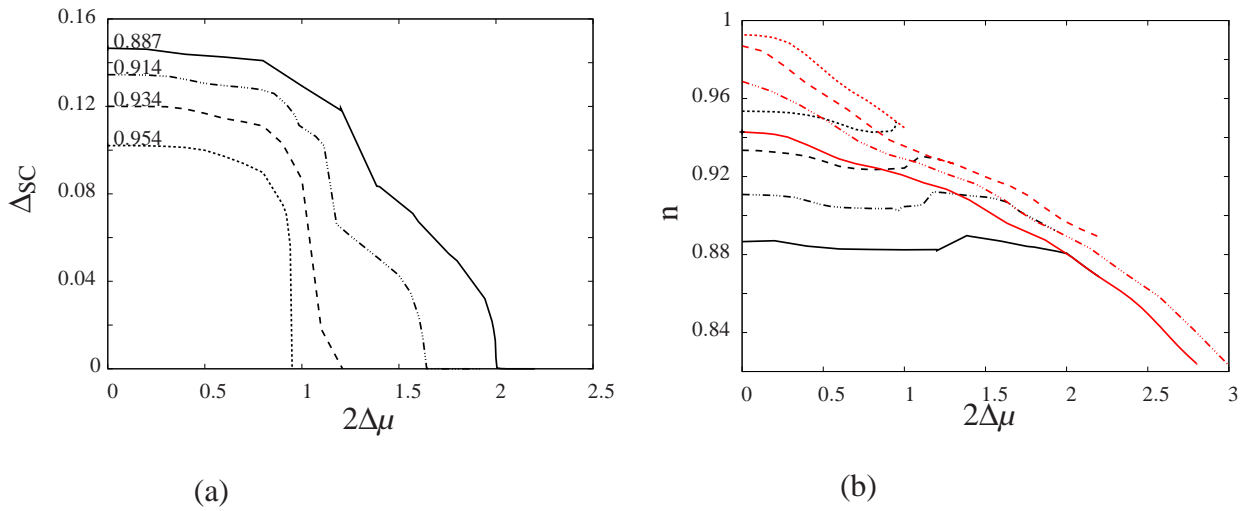


Figure 3.17: (a) Superconducting order parameter Δ_{SC} and (b) density vs. applied voltage, for a Hubbard monolayer as central region, for $\Gamma = 0.01$ and narrow lead bands $t_L = 1$. (a) Numbers represent the initial density. (b) The normal state density is shown as well (red lines). Further conventions are as in Fig. 3.16.

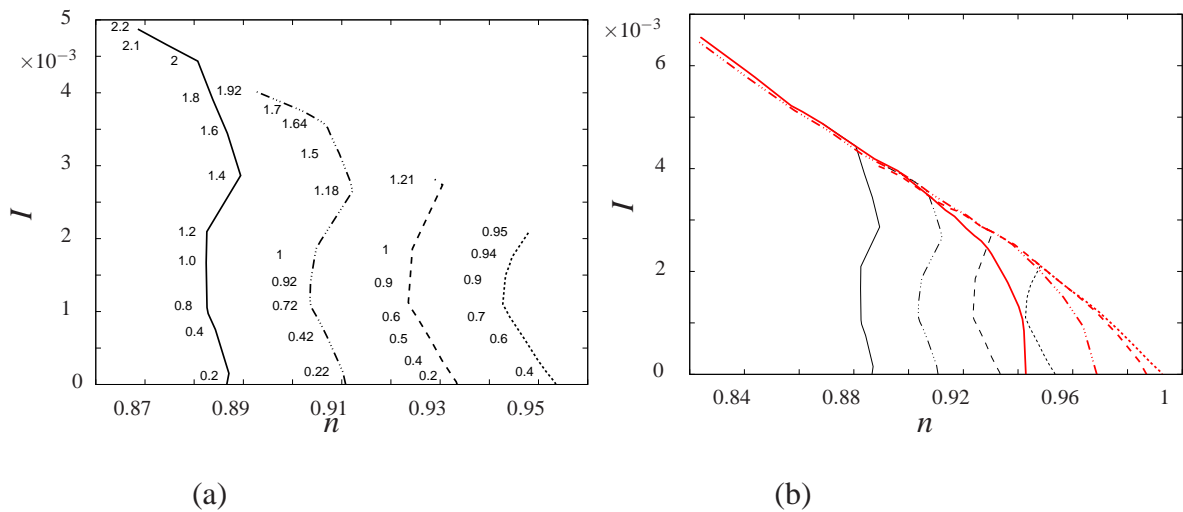


Figure 3.18: Current per unit contact-area I vs. density n through a Hubbard monolayer for $\Gamma = 0.01$ and $t_L = 1$. In (a) we show the current in the superconducting state, labels denote the applied voltage. In (b) the current in the normal state is shown additionally (red lines). Further conventions are as in Fig. 3.16.

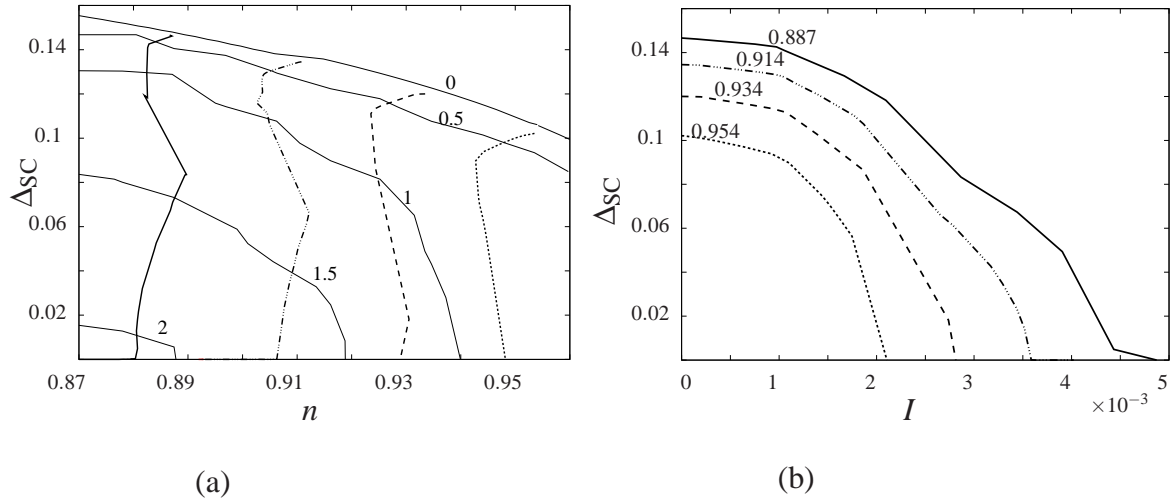


Figure 3.19: Superconducting order parameter Δ_{SC} , (a) vs. density n and (b) vs. current for a Hubbard monolayer as central region and $\Gamma = 0.01$ and $t_L = 1$. In (a) equipotential lines (gray full lines) are labeled with size of $2\Delta\mu$. In (b) numbers indicate the initial density. Further conventions are as in Fig. 3.16.

Wide Lead Bands Wider lead bands should emphasize the effect of the central regions spectral function, or better: reduce the effect of the lead DOS. We use $t_L = 9$ and $V = 0.437$ for the same four values of ϵ_C as above. The coupling strength again amounts to $\Gamma = n(\omega)\pi V^2 \approx 0.01$ at $\omega = 0$. Fig. 3.20 shows the results in the same format as was used for the figures containing the results obtained using narrow band leads.

Summarizing, we find two main differences from the results for narrow lead bands, regarding the superconducting state: There is a second region in voltage where all initial densities n_0 collapse to the same current, namely $2\Delta\mu = 1.5$. At this voltage, for the narrow bands, the sample was only superconducting for optimal doping. Moreover, we find that for wide lead bands, superconductivity survives up to higher values of voltage. This is remarkable, since the pure size of coupling strength Γ is larger in a wide range of energies. An explanation could be, that for narrow lead bands, the changes in coupling strength (or lead DOS) in energy ω are larger. We suggest that any band in the central regions avoids overlapping with sharp edges of lead bands. In the variational calculation, doing the derivative of the self-energy with respect to ϵ_{var} (which shifts the central region up/down in energy) will result in a large gradient in these regions. This effect should be softer using wide lead bands.

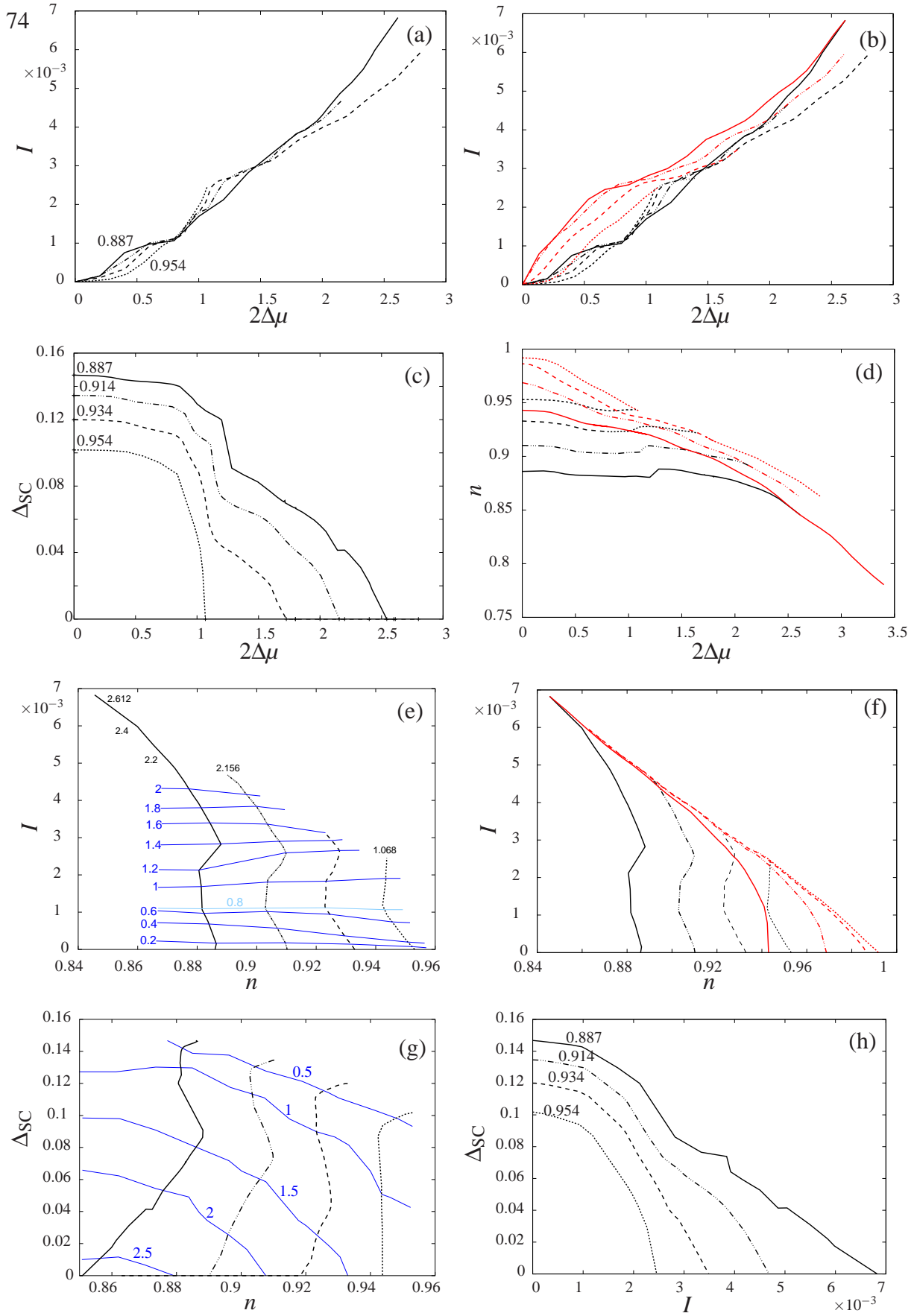


Figure 3.20: Illustration of the dependencies between current I , voltage $2\Delta\mu$, density n and superconducting order parameter Δ_{SC} for a Hubbard monolayer as central region and $\Gamma = 0.01$ and wide lead bands $t_L = 9$. In (e) and (g), equivoltage lines are drawn in blue. Conventions are as in Figs. 3.16,3.17,3.18,3.19.

3.12.1.2 $\Gamma = 0.005$, Wide Lead Bands

We now show results for wide lead bands $t_L = 9$, but with a reduced coupling strength of $\Gamma = 0.005$. The hybridisation amounts to $V = 0.3$. As we hoped for, the superconducting solution survives up to much larger voltages, especially for the optimally doped central region.

The dependence of the observables current I , density n and superconducting order parameter Δ_{SC} on voltage and on each other are illustrated in Fig. 3.21.

The current vs. voltage characteristics are shown in Fig. 3.21 (a) and (b). At low voltages, the dependence is similar to results for $\Gamma = 0.01$ (shown in the previous section), see inset of Fig. 3.21(b). Then, above $2\Delta\mu \approx 4$, there exists a wide region in voltage, where the differential conductance $\partial I/\partial(2\Delta\mu) \lesssim 0$, the current is almost constant, but rather decreasing with increasing voltage. Regarding the central region only, the current should not decrease. It is the diminishing overlap between the leads here, that results in the lightly dropping current. At $2\Delta\mu \approx 9$, there is again a fast upturn in current. This corresponds to the second peak in current, that we have obtained previously for an interacting ($U = 8$) central region (compare to Fig. 3.13). Note that for strong doping, there exists a superconducting solution up to this position $2\Delta\mu \approx 9$. The main features in the current vs. voltage characteristics are very similar for the superconducting and the normal state central region.

In Figures 3.21(c),(d) one can observe the constancy of superconducting order parameter Δ_{SC} and density over a wide voltage range. We also see, in Fig. 3.21(f), that while below $2\Delta\mu \lesssim 8$ the current behaves almost linear with doping, for larger values of voltage, the dependence is still linear, but in the other direction: Now for decreasing doping the current increases again. This is always the case for an interacting central region, and just not shown in previous figures, since the superconductivity did not survive up to these voltage values. The character of the dependence is the same in the normal state.

We summarize:

- For low values of voltages, $2\Delta\mu \lesssim 3.5$, the density, superconducting order and current have a strong dependence on $2\Delta\mu$.
- In the range of $3.5 \lesssim 2\Delta\mu \lesssim 8.5$, both current and density are almost constant, probably because in this voltage range there are no heavy changes in the amount of central region DOS contained between the lead bands and the chemical potentials μ_L, μ_R .

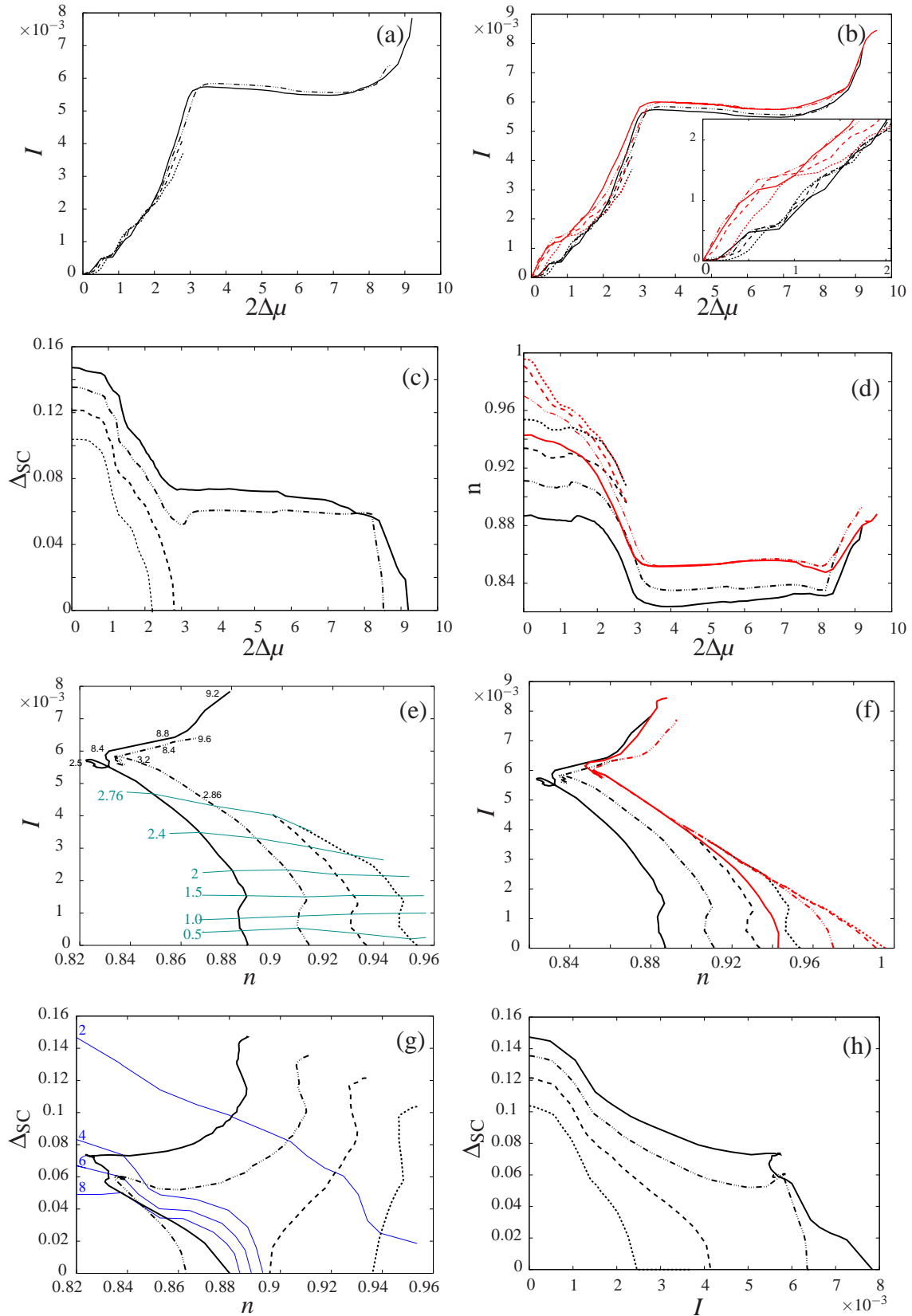


Figure 3.21: Dependencies of the observables I , n , Δ_{SC} and voltage $2\Delta\mu$ and on each other for a Hubbard monolayer as central region, for $\Gamma = 0.005$ and $t_L = 9$. In (e) and (g) we have added equivoltage lines (cyan and blue lines, respectively). Conventions are as in Figs. 3.16, 3.17, 3.18, 3.19.

- At $2\Delta\mu \approx 9$, however, the current starts to grow again, the doping moves closer to half filling and, most importantly, superconductivity vanishes even for optimal doping. We suppose, this is because at $2\Delta\mu \approx 9$ the upper Hubbard band gets enclosed into the current conducting energy range.

Fig. 3.21(h) shows, that the superconducting order parameter is not reduced monotonically with current. There are some small regions, where a growing current coexists with an upturn of the superconducting order, and vice versa. This means, that not only the pure amount of current can be the reason for the cancellation of superconductivity.

3.12.2 Bilayer as Central Region

We now want to find out what happens if the monolayer central region is substituted by a bilayer central region, as illustrated in Fig. 3.22. Will the second layer help to stabilize superconductivity in the central region? Is the current reduced, with respect to the monolayer, and how is the density of the two layers going to evolve? The results should hint towards what to expect for a thicker superconducting central region, which is already accessible to experiments. We can sim-

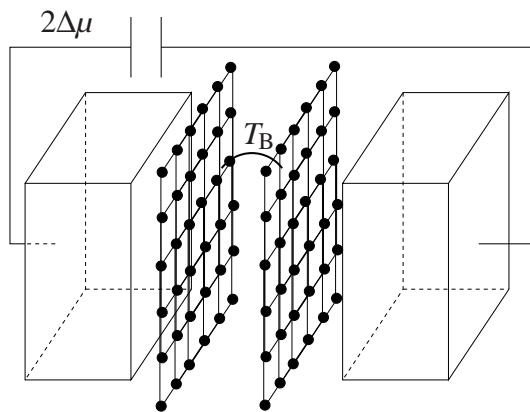


Figure 3.22: Non-equilibrium bilayer setup, T_B denotes the k_{\parallel} -dependent inter-layer hopping

ulate this problem using the previous methods, the VCA in Keldysh space. However, we have to adapt the equations for calculating the central region Green's function and the variational condition. We will outline the necessary changes in the next section. Then, in Section 3.12.2.2, we present the results for a Hubbard bilayer as central region, and compare to the monolayer results.

3.12.2.1 Adaptions in Model and Method

The central region is now a bilayer, with the usual hopping amplitude $t = -1$ in the layers and a small k_{\parallel} -dependent hopping parameterized by $\tilde{t} = 0.4t$ between the layers (interlayer hopping), as described in Section 2.2. This problem can be treated in several ways, we will sketch two of them and use only one for the simulation.

(1) Take a $2 \times 2 \times 2$ cluster as reference cluster. Most inter-layer hopping terms are then treated exactly in the cluster. However, this is very time consuming in the numerical calculation, because of the large Hilbert space.

(2) Another possibility is to choose two 2×2 reference clusters, one in each layer, couple the two clusters by CPT, and couple the bilayer to the leads:

The intra-layer inter-cluster hopping matrix $\underline{T}(K_{\parallel})$ recovers the Green's function of the layers, with K_{\parallel} the superlattice wave vector in the (x, y) -plane. The hopping matrix $\underline{T}_{\text{B}}(K_{\parallel})$ between the two layers recovers the bilayer Green's function. Then the central region Green's function becomes

$$\underline{g}_{\text{B}}^{-1} = \begin{pmatrix} \underline{g}_2^{-1} - \underline{T}(k_{\parallel}) & -\underline{T}_{\text{B}}(K_{\parallel}) \\ -\underline{T}_{\text{B}}(K_{\parallel}) & \underline{g}_1^{-1} - \underline{T}(k_{\parallel}) \end{pmatrix}, \quad (3.46)$$

where g_1 and g_2 are the Green's functions to the reference cluster Hamiltonians of layers 1,2. Moreover, each single layer is coupled to its neighbouring lead, described by the Green's function $\underline{g}_{L/R}$. Then the full bilayer Green's function in Keldysh space

$$\underline{G}_{\text{B}}^{-1} = \begin{pmatrix} \underline{g}_2^{-1} - \underline{T}(K_{\parallel}) - V_{\text{L}} \underline{g}_{\text{L}} V_{\text{L}} & -\underline{T}_{\text{B}}(K_{\parallel}) \\ -\underline{T}_{\text{B}}(K_{\parallel}) & \underline{g}_1^{-1} - \underline{T}(K_{\parallel}) - V_{\text{R}} \underline{g}_{\text{R}} V_{\text{R}} \end{pmatrix}, \quad (3.47)$$

depends on z , so that we can measure the current directly.

We settle for option (2), the CPT-coupling of two identical layers in order to obtain a larger unit cell. To simplify the problem, we use the same reference cluster for both layers, and allow only one set of variational parameters. Thus $\underline{g}_2 = \underline{g}_1 = \underline{g}_0$ and

$$\underline{G}_{\text{B}}^{-1} = \begin{pmatrix} \underline{g}_0^{-1} - \underline{T}(K_{\parallel}) - V_{\text{L}} \underline{g}_{\text{L}} V_{\text{L}} & -\underline{T}_{\text{B}}(K_{\parallel}) \\ -\underline{T}_{\text{B}}(K_{\parallel}) & \underline{g}_0^{-1} - \underline{T}(K_{\parallel}) - V_{\text{R}} \underline{g}_{\text{R}} V_{\text{R}} \end{pmatrix}, \quad (3.48)$$

When doing VCA, $\underline{T}(K_{\parallel})$ also contains information on the variational fields to be subtracted, $\underline{T}(K_{\parallel}) = \underline{T}_{\text{inter-CL}}(K_{\parallel}) - \underline{T}_{\text{intra}}$. The variational fields are contained in matrix $\underline{T}_{\text{intra}}(\vec{\lambda})$. Moreover, also the reference cluster Green's function \underline{g}_0 depends on the variational parameters $\vec{\lambda}$.

Variational Condition for Bilayer Now we come to the search for the solution of the model with the bilayer central region. Remember we need to stay at the root of eq. (3.43), which can be written as

$$\int \frac{d\omega}{2\pi} \text{Tr} \left[\frac{\partial \underline{\Sigma}}{\partial \lambda_i} (\underline{g}(\vec{\lambda}) - \underline{G}) \right]^{\text{K}} = 0, \quad (3.49)$$

where K denotes the Keldysh component. As reference system in the variational calculation we use a bilayer, consisting of two disconnected 2×2 clusters. Thus $\underline{g}(\vec{\lambda})$ and \underline{G} are the Green's functions of the bilayer system. It would also be possible to use just one of the two layers as reference system, such that $\underline{g}(\vec{\lambda})$ and \underline{G} are the Green's functions of one layer.

Since the clusters are disconnected, the self-energy is diagonal in the layers,

$$\underline{\Sigma} = \begin{pmatrix} \underline{\Sigma}_0 & \\ & \underline{\Sigma}_0 \end{pmatrix}. \quad (3.50)$$

Using this, we write eq. (3.43) as

$$\int \frac{d\omega}{2\pi} \text{Tr} \left(\frac{\partial \underline{\Sigma}_0}{\partial \lambda_i} \left[\begin{pmatrix} \underline{g}_0 & \\ & \underline{g}_0 \end{pmatrix} - \underline{G}_B \right] \right)^{\text{K}} = 0, \quad (3.51)$$

with \underline{G}_B from eq. (3.48). Here we have used as reference system the two distinct layers, not coupled to each other. In that way, we obtain for $\underline{g}(\vec{\lambda})$ a diagonal matrix, containing only the single layer Green's function \underline{g}_0 . The other possibility is to use a reference system consisting of a $2 \times 2 \times 2$ cluster connecting the layers. Since the steady state should not depend on the initial state, this should not make a difference. On the other hand, the reference system is modified by variational parameters on purpose, in order to move the initial state close to the steady state, where certainly inter-layer hopping occurs. Thus it would be important to include the inter-layer hopping in the reference cluster Green's functions in future work.

One can easily find that only the intra-layer parts of the bilayer Green's function contribute, because of the trace that is performed over cluster sites. Since $\underline{T}_B(K_{\parallel})$ is not present in our reference cluster we are then left with

$$\int \frac{d\omega}{2\pi} \text{Tr} \left[\frac{\partial \underline{\Sigma}_0}{\partial \lambda_i} (2\underline{g}_0 - \underline{G}_1 - \underline{G}_2) \right]^{\text{K}} = 0, \quad (3.52)$$

where \underline{G}_1 and \underline{G}_2 are the intra-layer parts of \underline{G}_B . The trace in the layer indices 1,2 has already been performed, and that in cluster sites and spin is left.

Current Calculation The current flowing through the setup can be measured at the interface between lead and central region, or between the two layers of the central region. In the second case, the k_{\parallel} -dependent hopping amplitude between the layers is the multiplicative factor V_{ij} in eq. (3.18) and

$$I \propto \sum_{k_{\parallel}} T_B(k_{\parallel}) \operatorname{Re} G_{12}^K(\vec{k}_{\parallel}), \quad (3.53)$$

where G_{12}^K is the Keldysh component of the inter-layer part of the bilayer Green's function \underline{G}_B .

The two currents should in fact coincide as described by Kirchhoff's current law. However, in the interacting case deviation might occur, since the method is not conserving.

We therefore only calculate the current between left lead and central region, where we do not have to consider the k_{\parallel} -dependence of the interlayer hopping.

3.12.2.2 Bilayer, $\Gamma = 0.01$, Wide Lead Bands

We now come to the results obtained for the bilayer central region. The two layers are described by the usual monolayer parameters, $U/t = 8$, $t'/t = 0.3$, and the additional k_{\parallel} -dependent inter-layer hopping, $\tilde{t}/t = 0.4$. We restrict ourselves to a single value of central region onsite energy, $\varepsilon_C = -1.4$, with the corresponding initial density $n_0 = 0.887$ in the superconducting sample. The coupling strength arises to $\Gamma \approx 0.01$, $t_L = 9$ and $V = 0.437$. We will compare the results for the bilayer to those of the monolayer setups with the same value of ε_C .

In Figure 3.23(a) we present the current vs. voltage characteristic of the bilayer setup, with the central region in the superconducting state and in the normal state. Again, we find that the current is slightly larger if the central region is in the normal state.

Fig. 3.23(b) displays the current-voltage characteristics of the bilayer together with that of the monolayer system. One can observe, that the current is of the same order of magnitude as that through the $\Gamma = 0.01$ monolayer system. It seems, that for small voltages the coupling strength Γ determines the amount of current. Dividing Γ by 2 also divides the current by 2.

We also want to point out, that in the normal state, the narrow band in the leads produces two separate peaks in the current, while the wide band has at the same positions ascending slopes.

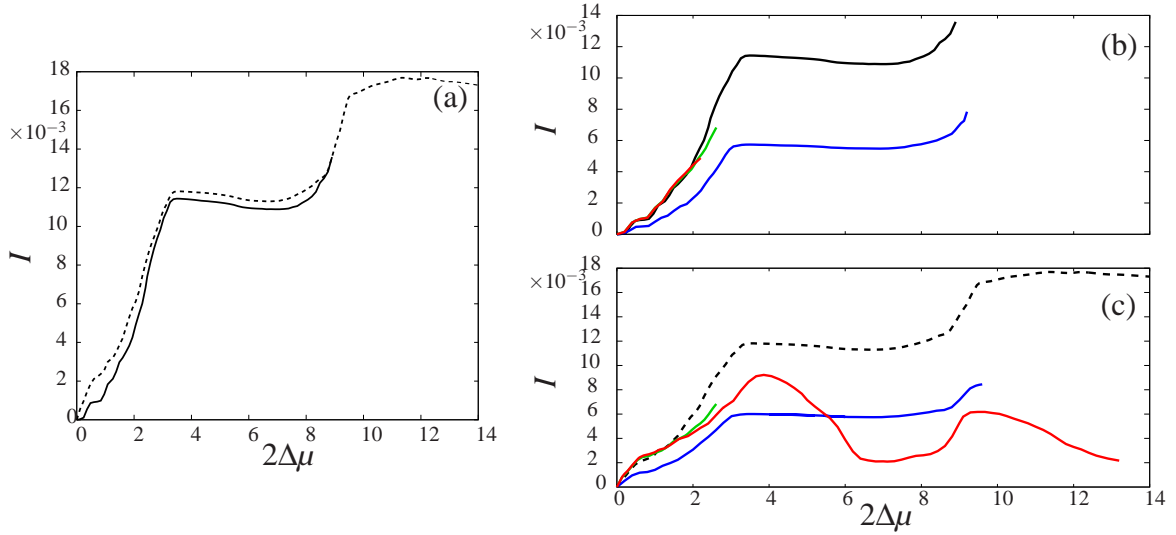


Figure 3.23: Current I (per unit contact-area) vs. voltage $2\Delta\mu$ through a Hubbard bilayer with $U/t = 8$, $t'/t = 0.3$, $\varepsilon_C = -1.4$ and k_{\parallel} dependent inter-layer hopping, for $\Gamma = 0.01$ and $t_L = 9$, by VCA. In (a) we show the current through the superconducting central region (solid line) and the normal state central region (dashed line). In (b) and (c) we compare the bilayer results (black, as in (a)) to the results obtained for the monolayer: wide band $\Gamma = 0.005$ (blue), wide band $\Gamma = 0.01$ (green) and narrow band $\Gamma = 0.01$ (red). In (b) we plot the current through the superconducting sample, and in (c) we plot the current through the normal state sample. The current is in units of lattice spacing $a = 1$, $\hbar = 1$, intra-layer hopping $t = 1$ and electron charge $e = 1$. All energies are in units of $t = 1$.

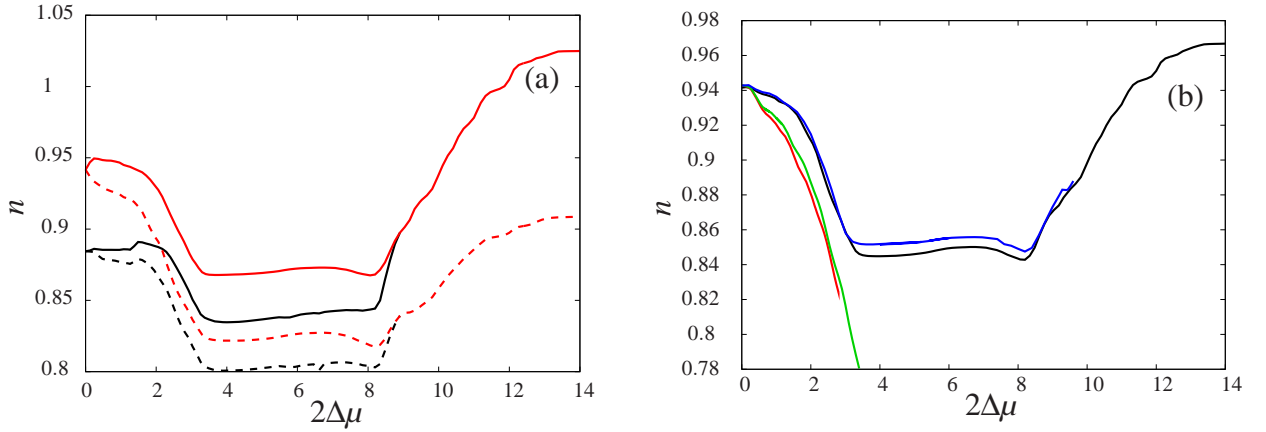


Figure 3.24: Dependence of the density n on voltage $2\Delta\mu$ for a Hubbard bilayer as central region, for $\Gamma = 0.01$ and $t_L = 9$. In (a) we show the bilayer results, we distinguish between the densities in the two layers (dashed and solid line) and superconducting (black) and normal (red) state. In (b) we compare the mean bilayer density (black) to the density obtained for a monolayer central region. The color-code and further conventions are as in Fig. 3.23.

We observe this contrast between wide and narrow bands in the superconducting state as well, for small enough coupling strength.

In Figure 3.24(a) we display the density as a function of voltage. The density of the two layers is drawn separately, and we find that the difference between the density in the two layers strongly depends on the applied voltage. For voltage $2\Delta\mu = 0$, the difference is about 0.05, but for very large voltage $2\Delta\mu \approx 12$ it is as large as 0.15, and while one layer is still hole doped, the other is electron doped. Actually, we found that for $U = 0$ this effect of asymmetric doping of the layers shows already at small voltages, and it is the interaction energy U that delays it.

Comparing to the results of the monolayer central region in Fig. 3.24(b) we see, that regarding the density, the bilayer with $\Gamma = 0.01$ behaves more like the monolayer with half coupling strength, $\Gamma = 0.005$.

Fig. 3.25(a) shows the dependence of Δ_{SC} on density, compared to the monolayer results. We cannot identify a simple pattern, and conclude that the density is not the driving force in the superconductor - normal state transition. Also the current shows not simple dependence on the central region density, see Fig. 3.25(b).

The dependence of the superconducting order parameter Δ_{SC} on the applied voltage is illustrated in Fig. 3.26(a), again together with monolayer results. One can clearly see, that Δ_{SC} shows rather the behaviour of the monolayer $\Gamma = 0.005$ system, than the monolayer $\Gamma = 0.01$ one, which is surprising. We can also see, that for narrow bands the decrease in Δ_{SC} happens most quickly. This could be, because the lead DOS has steep outer ranges. This steepness itself seems to lead to the fast decrease in superconductivity.

How the superconducting order parameter decreases with growing current can be seen in Fig. 3.26(b). Comparison to the monolayer data gives us the proof, that in the bilayer the superconducting solution is more stable against voltage and current than in the monolayer.

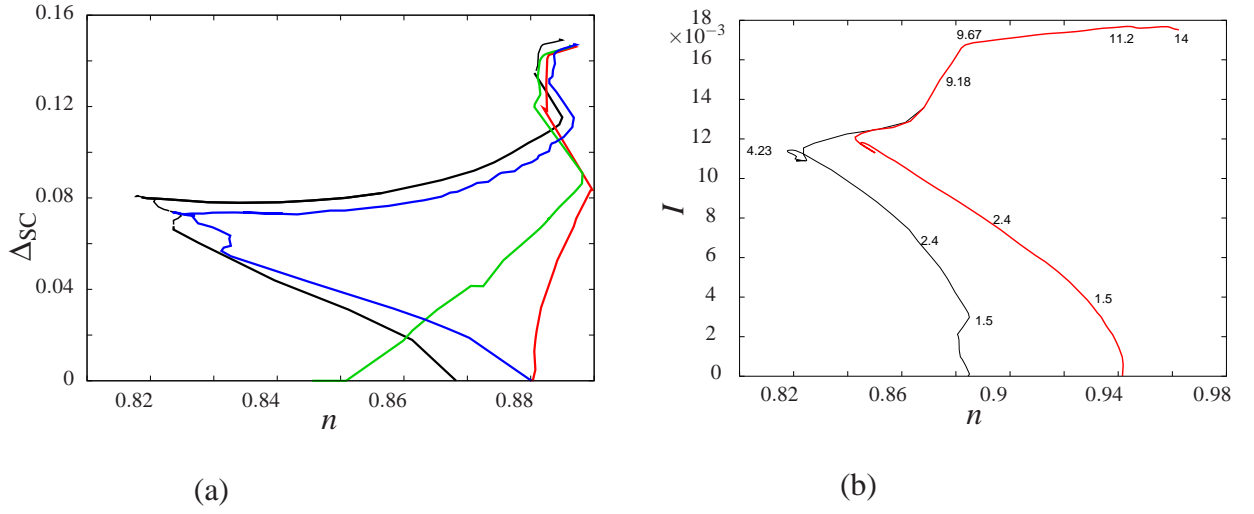


Figure 3.25: (a) Superconducting order parameter Δ_{SC} and (b) current vs. average density for the Hubbard bilayer as central region, for $\Gamma = 0.01$ and $t_L = 9$. In (a) we compare to monolayer data. In (b) we show the current through the central region in the superconducting state (black line) and in the normal state (red line). The numbers represent the corresponding voltage $2\Delta\mu$. The color-code and further conventions are as in Fig. 3.23.

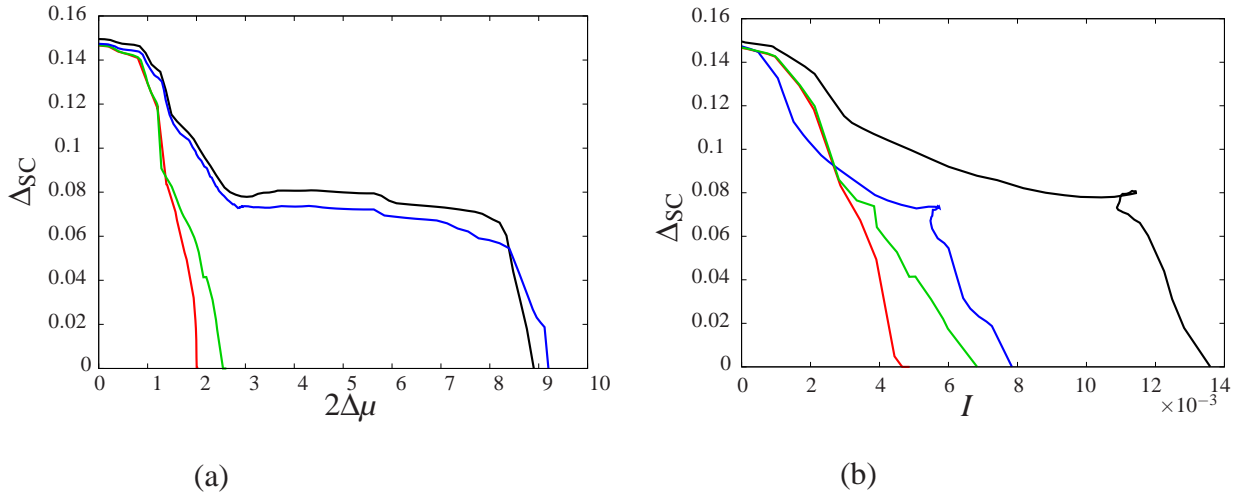


Figure 3.26: Superconducting order parameter Δ_{SC} vs. (a) voltage and (b) current for the bilayer Hubbard model as central region, for $\Gamma = 0.01$ and $t_L = 9$. We show additionally the corresponding data for the monolayer. The color-code and further conventions are as in Fig. 3.23.

3.12.3 Nearest-Neighbour Hubbard Monolayer as Central Region

A numerical investigation with a setup similar to ours is reported in Ref. [88]. The authors apply FLEX [87] with the Keldysh formalism to describe the phase transitions in a Hubbard model with $U/t = 4.5$ and only nearest neighbour hopping, under the influence of a bias voltage. They find that a bias-voltage of $2\Delta\mu = 0.1$ with $\Gamma = 1 \times 10^{-3}$ is sufficient to break down the superconducting phase. They however work in the wide band limit, where Γ is constant in frequency ω and wave vector in the (x, y) -plane.

We want to examine the NnSN model with the central region parameters they use, to see what we obtain with VCA in Keldysh space. We set $\epsilon_C = -1.56$. As starting variational parameters, we use $\epsilon_{\text{var}} = -0.154$ and $h_{\text{SC}} = 0.54$, which fulfill the self-consistency condition of equilibrium VCA, when the central region is decoupled from the leads.

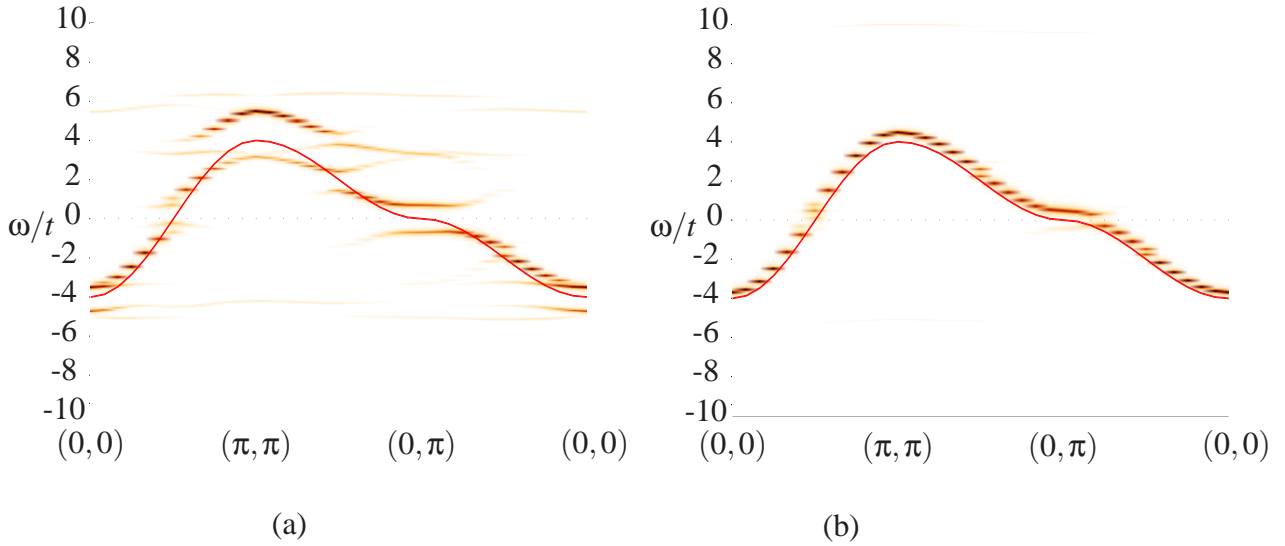


Figure 3.27: Spectral function as a color plot for a Hubbard monolayer, with $U/t = 4.5$ and $t'/t = 0$, by VCA. The line of maximum density in the lead is added in red. (a) In equilibrium, superconducting state, for hybridisation $V = 0$. (b) For a coupling strength $\Gamma = 0.01$, and a voltage of $2\Delta\mu = 0.08$. In the frequency integration, here we had to use adapted values for δ and integration accuracy.

When coupling this central region to TB leads and applying voltage, we found two solutions, depending on the coupling strength Γ :

(1) For a very small coupling strength, $\Gamma = 5 \times 10^{-5}$, and wide lead bands $t_L = 9$ and $V = 0.1$,

the system appears to remain in the equilibrium state. We could observe only minimal changes in the variational parameters as a function of applied voltage ($O(10^{-2})$). To obtain this solution, it was however necessary to accept much larger gradients than usually, as large as 10^{-3} . The corresponding spectral function of the central region is shown in Fig. 3.27 (a).

(2) For a larger coupling strength $\Gamma = 0.01$, and again $t_L = 9$, we observed the pinning of the central region spectral function to the leads spectral function, as shown in Fig. 3.27 (b). The variational parameters at this solution amount to $\epsilon_{\text{var}} = 0.44625827$ and $h_{\text{SC}} = 1.9738683$. This solution should be taken with care, because of the unphysical values of the variational parameters.

The problem seems to be, that the spectrum of the leads is very similar to the spectrum of the central region. For $U/t = 4.5$ the gap is quite small, and for $\Gamma = 0.01$ both the Hubbard and the superconducting gap are apparently eliminated by the hybridisation to the leads, however at variational parameters which are quite different from the usual values.

In order to compare our methods to FLEX + Keldysh, it would be necessary for us to work in the true wide band limit. A k_{\parallel} -independent dispersion relation for the electrodes can be obtained by setting the x and y directed hoppings in the leads to zero.

3.12.4 Summary of the Results

We here summarize the results obtained when simulating a superconducting mono(bi)layer between metal contacts using VCA and Keldysh Formalism, and formulate predictions for experiments.

We found that current I , central region density n and superconducting order parameter Δ_{SC} strongly depend on the applied voltage. Current grows with voltage, as long as the leads provide enough overlap in the density of states. Current peaks can appear where the Hubbard bands are struck by a high density of states in the leads. On the other hand, the superconducting order parameter decreases with voltage, even though the doping at the same time moves closer to optimal doping.

We distinguish four different regimes of coupling strength Γ :

- strong coupling: $\Gamma > 0.01$ leads to increasing difficulties to find solutions for the varia-

tional parameters, for the central region both in the normal state as well as in the superconducting state. The bands in the impurity might tune in with the lead bands, where possible.

- For $\Gamma \sim 0.01$ we find a phase transition when the voltage equals the superconducting gap size. The critical voltage depends on the initial density, the central region density when still uncoupled to the leads, which influences the gap size.
- For smaller coupling strength, in our case $\Gamma \sim 0.005$, the superconductor - normal state transition can also occur at much larger voltages, presumably when the upper Hubbard bands get involved in current transport.
- For small enough Γ nothing happens, with the system staying superconducting even at high voltages.

Possible Realization of the NnSN Junction in Experiment Our NnSN setup could be realized by epitaxially growing metallic contacts on a mono(bi)layer of superconducting material, e.g. by molecular beam epitaxy. The coupling strength depends on the atomic assembly between CuO_2 layers and the leads. It can be reduced by additional insulating material between the superconducting and metallic regions, or by atoms with a different band dispersion from the leads or central region.

3.13 Discussion and Conclusion

Like for the copper oxide layer in equilibrium, we are now going to discuss the approximations introduced by choosing model and solver. Moreover, we try to interpret the action of the variational condition.

3.13.1 Physics to Model

The approximations we make regarding a CuO_2 (bi)layer have already been described in Section 2.5, here we focus on the description of leads and hybridisation.

(1) Lead Hamiltonian We use a 3D tight binding model to describe the metallic leads. The TB model is appropriate for materials with limited overlap between atomic orbitals on neighbouring atoms, like Si, GaAs, SiO_2 and diamond, which are semiconductors. In transition metals, the narrow d-bands are TB bands, but these metals also contain broad conduction bands, which are not TB-like.

We found that the form of the lead bands, and their overlap with the central region bands, is deciding for reaction of the central region to voltage. When one wants to know what to expect from a specific realization of the NnSN junction, the dispersion of the lead bands should be considered. On the other hand, only the characteristics of the contact region is important for the properties obtained. Therefore, fine details of the band structure should not be important.

(2) Neglecting Disorder We describe a perfect crystal at temperature $T = 0$ and thus neglect scattering of electrons at impurities and phonons. In fact, what we simulate is the scattering of conductance electrons from electrons and superconducting pairs in the interacting region.

3.13.2 Solver

We now come to the systematic errors introduced by our method to solve the model. VCA generally, and the perturbative treatment of intra-layer and inter-layer hopping have been treated in Section 2.5. We will discuss here what has additionally to be considered when coupling to the leads and applying voltage.

(1) Reference Cluster Size To describe superconductivity in the central region, it was necessary to use a cluster of at least 2×2 in the (x, y) plane. On the other hand, because of the large numerical effort, we could not include more than 4 sites. Thus our reference system contains only sites of the central region, as illustrated in Fig. 3.1. Consequently, the hybridisation between central region and leads is only considered perturbatively, which should hold for small values of the coupling strength Γ . Moreover, we can not describe the direct interaction between particles on the leads and the central region. Because of the restricted cluster-size, we also neglect long-range Coulomb interaction in the interacting region. One assume that the important effects are sufficiently accounted for by a local self-energy, which can be well generated by a cluster of finite size [51].

(2) Variational Parameters The choice of the variational parameters affects the solutions that we can find. We have started with variational parameters, that describe the superconducting central region, when it is not in contact with the metal, namely a superconducting field h_{SC} and the central region onsite energy ϵ_C .

It is also possible that in a NnSN junction phase separation occurs, where some in some regions in the $(z = 0)$ -plane current flows through, and in other regions the superconducting order prevails. Localized current flux can not be described with our model, which is translation invariant and does not contain impurities, to which c-axis current tubes could pin.

We use no variational field to introduce an antiferromagnetic order in the interacting region. Antiferromagnetism could moreover provoke proximity magnetism in the leads. We do however simulate the NnSN junction in the hole-doped to heavily hole-doped regime, where a long-range antiferromagnetic order is not found in experiment, as shown in the phase diagram, Fig. 1.1.

(3) Finite Number of Clusters and Frequency Integration Like for the equilibrium problem, we have used a small number of clusters in the $(z = 0)$ -plane, namely 8×8 in the variational calculation. This leads to a reduced resolution in k_{\parallel} . We found that the quality of the evaluation of the variational condition is rather limited by the cluster size than the number of clusters. From our investigations we conclude, that the choice of appropriate broadening factors δ and the extrapolation to $\delta = 0$ is crucial in order to obtain meaningful results.

(4) Variational Condition We have used a Keldysh version of the equilibrium “Euler” equation eq. 2.26. In principle, that Euler equation is justified only, if the central region is in equilibrium with a certain grand potential Ω . The grand potential can be used for a system at given temperature T , volume V and chemical potential μ . However, here the chemical potential (and also T , Ω , et cetera) are not defined because the system is not in equilibrium.

(5) Choosing the Right Stationary Point In analogy to equilibrium, we find solutions to the variational condition in eq. 3.43. There is always a normal-state solution, and often a superconducting solution. Which of the two solutions is found, depends on the initial values of the variational parameters and the algorithm used for the search in variational parameter space. For the case in which multiple solutions occur, we do not have a minimum energy criterion as in equilibrium. Therefore, there is no criterion to say which one is the stable one. It is also possible, that the state in the central region depends on the previous state, in that case the junction shows a hysteresis-like behaviour as a function of the applied voltage. This however means, that the steady state depends on the initial state. If the voltage is increased very slowly, the system might always remain in a local stationary point and stay superconducting until the perturbation by the leads is too strong. On the other hand, a quick application of the voltage might destroy the information on the superconducting state, and the system could settle into a new state, where current can flow through the central region more easily, like in the normal state. In fact, we have simulated a slow increase of voltage, since the variational parameters at the start of each calculation for a voltage point was the result of the previous voltage point.

3.13.3 Summary

We have studied a three dimensional non-equilibrium setup with a two dimensional Hubbard interacting region using the Variational Cluster Approach in Keldysh space. As variational condition we use the analogon of the equilibrium “Euler” condition in Keldysh space, introduced in Ref. [53]. This allows us to investigate the steady state, which evolves in the central interacting layer when a constant bias voltage is applied. Most notably, this variational condition is suitable to study symmetry breaking phases, like superconductivity, in non-equilibrium.

The simulated setup describes a monolayer of high- T_c superconducting material, contacted by two metal leads at different chemical potentials. Using the Variational Cluster Approach in Keldysh space, we have performed calculations for this setup for four values of initial doping, coupling strengths $\Gamma = 0.005$ and $\Gamma = 0.01$, distinguishing wide and narrow lead bands. We found that the applied bias voltage and the bands of the leads strongly influence the interacting region, reducing the superconducting order parameter, changing the density in the superconducting region and causing a c-axis current to flow. Moreover, we have used a bilayer Hubbard model as central region, and compare the results of the bilayer to the monolayer system. As expected, we find that the superconducting order is more stable in the bilayer central region, as compared to the monolayer central region.

Analysing the dependence of the results on the coupling strength Γ we find that

- (a) for relatively strong coupling $\Gamma = 0.01$ the superconducting order is destroyed, when the bias voltage reaches the size of the superconducting gap and
- (b) for intermediate coupling $\Gamma = 0.005$ superconductivity exists up to a large bias voltage.

The superconducting order vanishes, when the upper Hubbard bands enter in the current conducting frequency range.

Based on our results, we formulate predictions for the physical experiment, distinguishing four regimes of coupling strength Γ . Our results indicate that the discussed model, investigated with the Variational Cluster Approach, represents a good description of a normal state - nano superconductor - normal state junction (NnSN), with tight-binding metal leads. We suggest, that the Variational Cluster Approach in Keldysh space could also be applied to simulate similar NnSN junctions with different parameters, or other non-equilibrium systems where strong correlations play a role.

Appendix A

Derivation of the Equilibrium Euler Equation

In this appendix, we revisit the derivation of Potthoff published in [54, 53], and thus make use of the same notation. One uses the self-energy functional $\hat{\Omega}[\Sigma]$

$$\hat{\Omega}_{t,U}[\Sigma] = \hat{F}_U[\Sigma] + \text{Tr} \ln(G_{t,0}^{-1} - \Sigma_{t,U})^{-1}, \quad (\text{A.1})$$

where t are the physical one-particle parameters and $F_U[\Sigma]$ is the Legendre transform of the Luttinger-Ward functional. The Luttinger-Ward functional is a universal functional of the self-energy Σ , that is, it is the same for all systems with different one-particle parameters t but the same interaction U . We have sketched it in Fig. 2.3.

The approximation made by VCA is to replace the original self-energy $\Sigma_{t,U}$ by $\Sigma_{t',U} = \Sigma(t')$, the self-energy of the reference system with one particle parameters t' , which is accessible.

$$\hat{\Omega}_{t,U}[\Sigma] = F_U[\Sigma(t')] + \text{Tr} \ln(G_{t',0}^{-1} - \Sigma(t'))^{-1} \quad (\text{A.2})$$

One wants to find the saddlepoint of $\hat{\Omega}_{t,U}[\Sigma_{t',U}]$ in t' and obtains:

$$\frac{\partial \hat{\Omega}_{t,U}[\Sigma]}{\partial t'} = \frac{\partial F_U[\Sigma(t')]}{\partial \Sigma(t')} \frac{\partial \Sigma(t')}{\partial t'} + \text{Tr}[(G_{t',0}^{-1} - \Sigma(t'))^{-1} \frac{\partial \Sigma(t')}{\partial t'}] = 0 \quad (\text{A.3})$$

Evaluating $\frac{\partial F_U[\Sigma]}{\partial \Sigma}$ for $\Sigma(t')$ gives $-T \hat{G}_U[\Sigma(t')] = -T G_{t',U}$.

$G_{t',U}$ is the Green's function of the reference system, called $g(\vec{\lambda})$ in eq. (3.42). Writing the trace as a sum over frequencies and sites, $\text{Tr} A = T \sum_{\omega} \sum_{\alpha} A_{\alpha\alpha}(\omega)$, one is left with

$$0 = T \sum_{\omega} \sum_{\alpha} \left(\frac{1}{G_{t,0}^{-1} - \Sigma(t')} - G_{t',U} \right)_{\alpha\beta} \frac{\partial \Sigma_{\beta\alpha}(t')}{\partial t'}. \quad (\text{A.4})$$

The first expression in the brackets corresponds to the CPT Green's function: $(G_{t,0}^{-1} - \Sigma(t'))^{-1} = G_{\text{CPT}}$, denoted G in eq. (3.42), so one has obtained

$$0 = -T \sum_{\omega} \sum_{\alpha} (g(\vec{\lambda}) - G)_{\alpha\beta} \frac{\partial \Sigma_{\beta\alpha}(t')}{\partial t'}. \quad (\text{A.5})$$

In VCA, the additional approximation is that not all the one-particle parameters t' of the reference system are varied, i.e. $\vec{\lambda} \neq t'$, and we thus replaced $G_{t',U}$ by $g(\vec{\lambda})$

Bibliography

- [1] L. V. Keldysh, Sov. Phys. JETP **20**, 1018 (1965).
- [2] A. Fulterer and E. Arrigoni, Journal of Superconductivity and Novel Magnetism (2012), <http://www.springerlink.com/content/212174r617034033/>.
- [3] J. Bardeen, L. N. Cooper, and J. R. Schrieffer, Phys. Rev. **108**, 1175 (1957).
- [4] A. Rothwarf, Physics Letters A **29**, 504 (1969).
- [5] M. R. Norman, Physics **1**, 21 (2008).
- [6] N. Plakida, *High-Temperature Cuprate Superconductors: Experiment, Theory, and Applications*, Springer Series in Solid-State Sciences (Springer, Heidelberg / New York / Tokyo, 2010).
- [7] D. A. Bonn, Nature Physics **2**, 159 (2006).
- [8] H. Alloul, F. Rullier-Albenque, B. Vignolle, D. Colson, and A. Forget, Europhys. Lett. **91**, (2010).
- [9] A. Lanzara, P. V. Bogdanov, X. J. Zhou, S. A. Kellar, D. L. Feng, E. D. Lu, T. Yoshida, H. Eisaki, A. Fujimori, K. Kishio, J. I. Shimoyama, T. Noda, S. Uchida, Z. Hussain, and Z. X. Shen, Nature (London) **412**, 510 (2001).
- [10] T. A. Maier and D. J. Scalapino, Phys. Rev. B **84**, 180513 (2011).
- [11] A. Kaminski, M. Randeria, J. C. Campuzano, M. R. Norman, H. Fretwell, J. Mesot, T. Sato, T. Takahashi, and K. Kadowaki, Phys. Rev. Lett. **86**, 1070 (2001).
- [12] R. Wood, M. Mostoller, and J. Cooke, Physica C: Superconductivity **165**, 97 (1990).

- [13] A. S. Davydov, *Physica Status Solidi (b)* **146**, 619 (1988).
- [14] A. Mourachkine, *Superconductor Science and Technology* **17**, 721 (2004).
- [15] P. W. Anderson, *Phys. Rev.* **79**, 350 (1950).
- [16] J. Zaanen, G. A. Sawatzky, and J. W. Allen, *Phys. Rev. Lett.* **55**, 418 (1985).
- [17] V. J. Emery, *Phys. Rev. Lett.* **58**, 2794 (1987).
- [18] A. P. Kampf, *Phys. Rep.* **249**, 219 (1994).
- [19] P. W. Anderson, *Science* **235**, 1196 (1987).
- [20] A. Tanaka, *Journal of Physics A: Mathematical and Theoretical* **40**, 10415 (2007).
- [21] W. Hanke, M. Kiesel, M. Aichhorn, S. Brehm, and E. Arrigoni, *Europ. Phys. J. - Spec. Topics* **188**, 15 (2010).
- [22] D. Sénéchal, P. L. Lavertu, M. A. Marois, and A. M. S. Tremblay, *Phys. Rev. Lett.* **94**, 156404 (2005).
- [23] M. Aichhorn, E. Arrigoni, Z. B. Huang, and W. Hanke, *Phys. Rev. Lett.* **99**, 257002 (2007).
- [24] D. Sénéchal, D. Perez, and D. Plouffe, *Phys. Rev. B* **66**, 075129 (2002).
- [25] D. Sénéchal, D. Perez, and M. Pioro-Ladrière, *Phys. Rev. Lett.* **84**, 522 (2000).
- [26] B. Scott, E. Suard, C. Tsuei, D. Mitzi, T. McGuire, B.-H. Chen, and D. Walker, *Physica C: Superconductivity* **230**, 239 (1994).
- [27] A. Kopp and S. Chakravarty, *Proc SPIE* **5932**, 593219 (2005).
- [28] Chakravarty, H.-Y. Kee, and K. Voelker, *Nature* **428**, 53 (2004).
- [29] G. Kastinakis, *Eur. Phys. J. B* **73**, 483 (2010).
- [30] A. Bansil, M. Lindroos, S. Sahrakorpi, and R. S. Markiewicz, *Phys. Rev. B* **71**, 012503 (2005).
- [31] A. Damascelli, *Physica Scripta* **T109**, 61 (2004).

- [32] A. Damascelli, Z.-X. Shen, and Z. Hussain, *Rev. Mod. Phys.* **75**, 473 (2003).
- [33] A. Damascelli, D. H. Lu, and Z. X. Shen, *J. Electron Spectr. Relat. Phenom.* **117–118**, 165 (2001).
- [34] D. L. Feng, C. Kim, H. Eisaki, D. H. Lu, A. Damascelli, K. M. Shen, F. Ronning, N. P. Armitage, N. Kaneko, M. Greven, J.-i. Shimoyama, K. Kishio, R. Yoshizaki, G. D. Gu, and Z.-X. Shen, *Phys. Rev. B* **65**, 220501 (2002).
- [35] P. Bogdanov, A. Lanzara, X. J. Zhou, S. A. Kellar, D. L. Feng, E. D. Lu, H. Eisaki, J.-I. Shimoyama, K. Kishiio, Z. Hussain, and Z. X. Shen, *Physical Review B* **64**, 180505 (2001).
- [36] D. L. Feng, N. P. Armitage, D. H. Lu, A. Damascelli, J. P. Hu, P. Bogdanov, A. Lanzara, F. Ronning, K. M. Shen, H. Eisaki, C. Kim, Z.-X. Shen, J. i. Shimoyama, and K. Kishio, *Phys. Rev. Lett.* **86**, 5550 (2001).
- [37] Y.-D. Chuang, A. D. Gromko, A. V. Fedorov, Y. Aiura, K. Oka, Y. Ando, M. Lindroos, R. S. Markiewicz, A. Bansil, and D. S. Dessau, *Phys. Rev. B* **69**, 094515 (2004).
- [38] O. K. Andersen, A. I. Liechtenstein, O. Jepsen, and F. Paulsen, *J. Phys. Chem. Solids* **56**, 1573 (1995).
- [39] S. S. Kancharla and S. Okamoto, *Phys. Rev. B* **75**, 193103 (2007).
- [40] S. Grabowski, J. Schmalian, and K. Bennemann, *Physica B: Condensed Matter* **230-232**, 948 (1997), proceedings of the International Conference on Strongly Correlated Electron Systems.
- [41] G. S. Uhrig, K. P. Schmidt, and M. Grüninger, *Journal of the Physical Society of Japan* **74S**, 86 (2005).
- [42] P. Pathak and Ajay, *Physica C: Superconductivity* **444**, 31 (2006).
- [43] A. I. Liechtenstein, O. Gunnarsson, O. K. Andersen, and R. M. Martin, *Phys. Rev. B* **54**, 12505 (1996).
- [44] R. Eder, Y. Ohta, and S. Maekawa, *Phys. Rev. Lett.* **74**, 5124 (1995).

- [45] M. Eschrig and M. R. Norman, Phys. Rev. Lett. **89**, 277005 (2002).
- [46] J.-X. Li, T. Zhou, and Z. D. Wang, Physical Review B (Condensed Matter and Materials Physics) **72**, 094515 (2005).
- [47] M. Potthoff, M. Aichhorn, and C. Dahnken, Phys. Rev. Lett. **91**, 206402 (2003).
- [48] C. Dahnken, M. Aichhorn, W. Hanke, E. Arrighoni, and M. Potthoff, Phys. Rev. B **70**, 245110 (2004).
- [49] M. Aichhorn and E. Arrighoni, Europhys. Lett. **72**, 117 (2005).
- [50] M. Aichhorn, E. Arrighoni, M. Potthoff, and W. Hanke, Phys. Rev. B **74**, 235117 (2006).
- [51] M. Aichhorn, E. Arrighoni, M. Potthoff, and W. Hanke, Phys. Rev. B **74**, 024508 (2006).
- [52] M. Potthoff and M. Balzer, Phys. Rev. B **75**, 125112 (2007).
- [53] M. Potthoff, in *Theoretical Methods for Strongly Correlated Systems, Springer Series in Solid-State Sciences*, edited by A. Avella and F. Mancini (Springer, New York Wien Heidelberg, 2011).
- [54] M. Potthoff, Eur. Phys. J. B **32**, 429 (2003).
- [55] C. Lanczos, Journal Of Research Of The National Bureau Of Standards **45**, 255 (1950).
- [56] M. Balzer, W. Hanke, and M. Potthoff, Phys. Rev. B **77**, 045133 (2008).
- [57] M. Balzer, B. Kyung, D. Sénéchal, A.-M. S. Tremblay, and M. Potthoff, Europhysics Letters **85**, 17002 (2009).
- [58] J. M. Luttinger and J. C. Ward, Phys. Rev. **118**, 1417 (1960).
- [59] C. Kim, P. J. White, Z.-X. Shen, T. Tohyama, Y. Shibata, S. Maekawa, B. O. Wells, Y. J. Kim, R. J. Birgeneau, and M. A. Kastner, Phys. Rev. Lett. **80**, 4245 (1998).
- [60] A. M. S. Tremblay, B. Kyung, and D. Sénéchal, Low Temp. Phys. **32**, 424 (2006).
- [61] We define it as the doping for which the SC order parameter is suppressed by about 10%.
- [62] Z.-X. Shen and D. S. Dessau, Phys. Rep. **253**, 1 (1995).

- [63] M. Okawa, K. Ishizaka, H. Uchiyama, H. Tadamoto, T. Masui, S. Tajima, X.-Y. Wang, C.-T. Chen, S. Watanabe, A. Chainani, T. Saitoh, and S. Shin, *Phys. Rev. B* **79**, 144528 (2009).
- [64] V. B. Zabolotnyy, S. V. Borisenko, A. A. Kordyuk, J. Geck, D. Inosov, A. Koitzsch, J. Fink, M. Knupfer, B. Buechner, S. L. Drechsler, and et al., *Physical Review B* **76**, 4 (2006).
- [65] G. S. Uhrig, K. P. Schmidt, and M. Grüninger, *Journal of the Physical Society of Japan* **74S**, 86 (2005).
- [66] M. Potthoff, *Aip Conference Proceedings* **816**, 14 (2005).
- [67] N. Kim, H.-J. Lee, J.-J. Kim, J.-O. Lee, J. Park, K.-H. Yoo, S. Lee, and K. Park, *Solid State Communications* **115**, 29 (2000).
- [68] Y. C. Ma, J. W. Liu, H. W. Lu, and H. L. Zheng, *Journal of Physics: Condensed Matter* **19**, 186203 (2007).
- [69] C. C. Homes, T. Timusk, R. Liang, D. A. Bonn, and W. N. Hardy, *Phys. Rev. Lett.* **71**, 1645 (1993).
- [70] D. N. Basov, S. I. Woods, A. S. Katz, E. J. Singley, R. C. Dynes, M. Xu, D. G. Hinks, C. C. Homes, and M. Strongin, *Science* **283**, 49 (1999).
- [71] D. G. Clarke, S. Strong, and P. W. Anderson, *Phys. Rev. Lett.* **74**, 4499 (1995).
- [72] W. Meevasana, T. P. Devereaux, N. Nagaosa, Z.-X. Shen, and J. Zaanen, *Phys. Rev. B* **74**, 174524 (2006).
- [73] M. Grüninger, D. van der Marel, A. Damascelli, A. Erb, T. Nunner, and T. Kopp, *Phys. Rev. B* **62**, 12422 (2000).
- [74] R. J. Radtke, V. N. Kostur, and K. Levin, *Phys. Rev. B* **53**, R522 (1996).
- [75] P. W. Anderson, *Science* **279**, 1196 (1998).
- [76] A. A. Dzhioev and D. S. Kosov, *Journal of Physics: Condensed Matter* **24**, 225304 (2012).

- [77] R.C. and Dynes, *Physica C: Superconductivity* **225** (1994).
- [78] R. Kleiner, P. Müller, H. Kohlstedt, N. F. Pedersen, and S. Sakai, *Phys. Rev. B* **50**, 3942 (1994).
- [79] R. Kleiner and P. Müller, *Phys. Rev. B* **49**, 1327 (1994).
- [80] C. O'Donovan, M. D. Lumsden, B. D. Gaulin, and J. P. Carbotte, *Phys. Rev. B* **55**, 9088 (1997).
- [81] K. Ueno and S. N. et al., *Nat Mater* **7**, 855 (2008).
- [82] X. Leng, J. Garcia-Barriocanal, S. Bose, Y. Lee, and A. M. Goldman, *Phys. Rev. Lett.* **107**, 027001 (2011).
- [83] P.-H. Xiang, S. Asanuma, H. Yamada, I. H. Inoue, H. Sato, H. Akoh, A. Sawa, K. Ueno, H. Yuan, H. Shimotani, M. Kawasaki, and Y. Iwasa, *Advanced Materials* **23**, 5822 (2011).
- [84] X. Leng, J. Garcia-Barriocanal, B. Yang, Y. Lee, J. Kinney, and A. M. Goldman, *Phys. Rev. Lett.* **108**, 067004 (2012).
- [85] A. S. Alexandrov, V. V. Kabanov, and N. F. Mott, *Phys. Rev. Lett.* **76**, 12 (1996).
- [86] D. Fausti, R. I. Tobey, N. Dean, S. Kaiser, A. Dienst, M. C. Hoffmann, S. Pyon, T. Takayama, H. Takagi, and A. Cavalleri, *Science* **331**, 189 (2011).
- [87] G. Esirgen and N. E. Bickers, *Phys. Rev. B* **57**, 5376 (1998).
- [88] T. Oka and H. Aoki, *Phys. Rev. B* **82**, 064516 (2010).
- [89] S. Das, S. Rao, and A. Saha, *Europhysics Letters* **81**, 67001 (2008).
- [90] A. F. Andreev, *Sov.Phys. JETP* **19**, .
- [91] H. Meissner, *Phys. Rev.* **117**, 672 (1960).
- [92] E. N. Economou, *Green's functions in quantum physics, Springer series in solid-state sciences* (Springer, Heidelberg / New York / Tokyo, 2006), p. 477.
- [93] Y. Alhassid, *Rev. Mod. Phys.* **72**, 895 (2000).

- [94] P. Mehta and N. Andrei, Phys. Rev. Lett. **96**, 216802 (2006).
- [95] S. Weiss, J. Eckel, M. Thorwart, and R. Egger, Phys. Rev. B **77**, 195316 (2008).
- [96] F. B. Anders, Phys. Rev. Lett. **101**, 066804 (2008).
- [97] E. Boulat, H. Saleur, and P. Schmitteckert, Phys. Rev. Lett. **101**, 140601 (2008).
- [98] Y. Nazarov and Y. Blanter, *Quantum Transport: Introduction to Nanoscience* (Cambridge University Press, Cambridge, 2009).
- [99] M. Esposito, U. Harbola, and S. Mukamel, Rev. Mod. Phys. **81**, 1665 (2009).
- [100] M. Knap, W. von der Linden, and E. Arrigoni, Phys. Rev. B **84**, 115145 (2011).
- [101] A. Altland and R. Egger, in *Modern theories of many-particle systems in condensed matter physics* (Springer, Heidelberg, 2012).
- [102] H. Haug and A.-P. Jauho, *Quantum Kinetics in Transport and Optics of Semiconductors* (Springer, Heidelberg, 1998).
- [103] A. L. Fetter and J. D. Walecka, *Quantum Theory of Many-Particle Systems* (McGraw-Hill, New York, 1971).
- [104] D. C. Cabra, A. Honecker, and P. Pujol, in *Modern Theories of Many-Particle Systems in Condensed Matter Physics*, Springer (Springer, Heidelberg, 2012).
- [105] J. Rammer and H. Smith, Rev. Mod. Phys. **58**, 323 (1986).
- [106] M. Knap and E. Arrigoni, private communication (unpublished).
- [107] M. Balzer and M. Potthoff, Phys. Rev. B **83**, 195132 (2011).
- [108] A. M. Fulterer, M. Knapp, and E. Arrigoni, (in preparation) .
- [109] M. Nuss, E. Arrigoni, M. Aichhorn, and W. von der Linden, arXiv (2011), arXiv:1110.4533v2.
- [110] D. Sénéchal, arXiv:0806.2690 (unpublished).
- [111] X. Lu and E. Arrigoni, Phys. Rev. B **79**, 245109 (2009).

Curriculum Vitae of the Author

Personal

- Anna Maria Fulterer
- Born on October 27, 1982, in Meran (BZ).
- Italian Citizen.
- Married, two children: Samuel *2007, Maja *2010.

Education

- Dipl. Ing equiv M.A. Technical Physics with distinction, 2007. supported by two merit scholarships by the TU Graz.
- Diploma theses in Medical Imaging at the Institute of Electronics, Forschungszentrum Jülich, Germany, 2006.
Title: Investigation on the Impact of Out Field of View Activity in High Resolution Positron Emission Tomography
supported by a scholarship by Zonta and the TU Graz.
- Matura - secondary school leaving exam with distinction with distinction, 2001.
- schoolyear at the Bournemouth and Poole College of further Education in Great Britain, with a scholarship of the region Trentino-Südtirol
Certificate in Advanced English
A-level in Sociology and Italian, AS-Level in Mathematics and Human Biology, 2000
- Visit of the secondary school in german language in Bozen, Italy, 1988-2001.

